Distribution Agreement

Signature:

________________________________ ________________

Hanlin Chen Date

Structure and dynamics of the mesodomain environment of coenzyme B_{12}-dependent ethanolamine ammonia-lyase in frozen aqueous solutions and kinetics of the radical rearrangement reaction at 173-187 K

by
Hanlin Chen
Doctor of Philosophy
Physics

Dr. Kurt Warncke
Advisor

Dr. Laura Finzi
Committee Member

Dr. Stefan Boettcher
Committee Member

Dr. Connie Roth
Committee Member

Dr. David Dunlap
Committee Member

Accepted:

Lisa A. Tedesco, Ph.D.
Dean of the Graduate School

Date

Structure and dynamics of the mesodomain environment of coenzyme B_{12}-dependent ethanolamine ammonia-lyase in frozen aqueous solutions and kinetics of the radical rearrangement reaction at 173-187 K

By

Hanlin Chen

M.Sc., Huazhong University of Science & Technology, Wuhan, China, 2007

Advisor:

Kurt Warncke, PhD.

An abstract of

A Dissertation Submitted to the Faculty of the

James T. Laney Graduate School of Emory University

in Partial Fulfillment of the Requirements for the Degree of

Doctor of Philosophy

in Physics

2014

Abstract

Structure and dynamics of the mesodomain environment of coenzyme B_{12}-dependent ethanolamine ammonia-lyase in frozen aqueous solutions and kinetics of the radical rearrangement reaction at 173-187 K

By

Hanlin Chen

The aqueous solution environment has been proposed to influence protein function by coupling with bulk solvent and hydration-shell fluctuations. To provide a deeper understanding of the relative importance of solvent mobility, intrinsic protein motions and coupling between solvent and protein motions, this dissertation embarks on characterizing the properties of the mesodomain in aqueous sucrose solutions over the range from 0 – 75% (w/v) of added sucrose, by using the paramagnetic probe, TEMPOL, and multiple electron paramagnetic resonance (EPR) techniques. The results characterize the glass transition, TEMPOL concentration, and volume of the mesodomain. The studies are extended to investigate the microscopic structure of frozen aqueous sucrose solutions which contain the coenzyme B_{12}-dependent ethanolamine ammonia-lyase (EAL) from *Salmonella typhimurium*, with and without the substrate, ethanolamine. It is concluded that the protein creates a mesodomain in frozen aqueous solutions. In a separate study, the kinetics of the Co(II)-substrate radical pair decay reaction were measured at temperatures of 173-187 K, which are below the mesodomain glass transition. The power-law decay kinetics indicate the emergence of multiple exponential phases, suggesting that protein, and possibly coupled non-bulk, hydration solvent, motions become rate determining for the radical rearrangement in the examined temperature range. Overall, the mesodomain and low temperature kinetic studies contribute to the understanding of the roles of protein and coupled solvent dynamics in EAL function.

Structure and dynamics of the mesodomain environment of coenzyme B_{12}-dependent ethanolamine ammonia-lyase in frozen aqueous solutions and kinetics of the radical rearrangement reaction at 173-187 K

By

Hanlin Chen

M.Sc., Huazhong University of Science & Technology, Wuhan, China, 2007

Advisor:

Kurt Warncke, PhD.

A Dissertation Submitted to the Faculty of the

James T. Laney Graduate School of Emory University

in Partial Fulfillment of the Requirements for the Degree of

Doctor of Philosophy

in Physics

2014

Acknowledgements

I am sincerely grateful to my advisor, Prof. Kurt Warncke, for the guidance he provided in the past years. When there are “road bumps” in my projects, there are his insightful suggestions, skillful EPR maintenance, solid knowledge, his wisdom, patience and humor. Without his support and encouragement, the research presented here would not be possible. I owe thanks to the members of my committee, Dr. Laura Finzi, Dr. Stefan Boettcher, Dr. Connie Roth, and Dr. David Dunlap for their critiques, thoughts and encouraging words. I also owe thanks to the members in the Warncke lab. I learned from Dr. Li Sun, Dr. William Gunderson and Dr. Chen Zhu how to manipulate the pulsed- and CW- EPR spectroscopies and solve the problems in my research. Dr. Li Sun and I coworked on two projects. His creativity and patience inspired me and improved my capability of solving scientific problems. Dr. Adonis Bovell, my officemate, enriched my graduate study with joy and laughter. His profession in Matlab, biochemistry, and English greatly helped me in my development. I also thank Dr. Wesley Roberson for improving the yield in my EAL purification experiments, Dr. Jessica Hernandez-Guzman for her help in the OPTESIM training, and Dr. Miao Wang for his help in ordering EPR tubes. I thank Nesli and Meghan for their helpful suggestions and trouble-shootings in my experiments. I must thank my friends, Dr. Qing Shao, Dr. Jingping Yang and Dr. Haowei Wang for their help in releasing my stresses when experiments did not work and I did not know why.

I am deeply grateful to my father, Mingchun Chen, my mother, Shengmei Zhao, my two sisters, Weilin Chen and Yulin Chen, and my lovely husband, Hanjun Fang, for their unconditional love and support, which continuously provide energy for me to pursue my dreams.

Table of Contents

List of Figures

Chapter 1: Introduction 1

Chapter 2: Heterogeneous Ordered–Disordered Structure of the Mesodomain in Frozen Sucrose–Water Solutions Revealed by Multiple Electron Paramagnetic Resonance Spectroscopies 19

List of Schemes

List of Tables

Chapter 3: Structure and Dynamic Properties of the Mesodomain Environment of the protein Ethanolamine Ammonia-Lyase (EAL), in Frozen Aqueous Sucrose Solutions 48

Chapter 4: Probing Decay Kinentics of Co(II)-[^{1}H]-substrate radical pair at temperatures below 190 K 75

Chapter 1

Introduction

1.1 Coenzyme B_{12}-dependent enzyme, ethanolamine ammonia-lyase (EAL)

Ethanolamine ammonia-lyase (EAL), a coenzyme B_{12} (adenosylcobalamin, AdoCbl)-dependent bacterial enzyme, which is coded by the *eut* operon, catalyzes the conversion of ethanolamine into acetaldehyde and ammonia.[1-3] EAL from *Salmonella typhimurium* is composed of two different subunits EutB (453-residue, 49.4 kDa) and EutC (286-residue, 32.1 kDa), which assemble into an $EutB_6EutC_6$ ($\alpha_6\beta_6$) oligomer, with a molecular mass of approximately 500 kDa.[4] The X-ray crystallographic structure from the *Escherichia coli* EAL shows that substrate ethanolamine binds at the interface of EutB and EutC.[5] EAL is biologically important for its ability to use ethanolamine rich in the intestine as an energy, carbon and nitrogen source,[6-8] which is beneficial for the bacterial colonization of the gut.[9, 10] It was found that many pathogens carrying *eut* genes cause food poisoning.[11]

EAL is an important member in coenzyme B_{12}-dependent enzyme superfamily.[12, 13] This superfamily of enzymes is categorized into three classes: (a) Class I (mutase) coenzyme B_{12}-dependent enzymes including glutamate mutase,[14, 15] isobutyryl-CoA mutase,[16] 2-methylene-glutarate mutase[17, 18] and methylmalonyl-CoA mutase (MCM),[19] catalyze carbon skeleton rearrangements reactions. (b) Class II (eliminase) coenzyme B_{12}-dependent enzymes including EAL,[20, 21] glycerol dehydratase,[22] propane-1,2-diol dehydratase,[23] and ribonucleotide triphosphate reductase,[24] catalyze the migration of hydroxyl or amino group on substrates and release water or ammonia in the final product; (c) Class III [pyridoxal phosphate (PLP)-dependent] coenzyme B_{12}-dependent enzymes including lysine 2,3-aminomutase[25] and ornithine 4,5-aminomutase,[26] catalyze amino migration reactions. These enzymes are found in bacteria, except MCM, which is present in humans. The MCM catalyzed rearrangement of (*R*)-methylmalonyl-CoA to succinyl-CoA, is indispensable in human metabolism and the cause of the disease, methylmalonic ketonuria.[27]

In this dissertation, EAL from *S. typhimurium* is used to investigate the surrounding solvent environment, the catalytic mechanism and kinetics at low temperatures. Even though the structure of *S. typhimurium* EAL remains unsolved, by X-ray crystallography, it has been homology modeled from the resolved X-ray structure of the related coenzyme B_{12}-dependent enzyme from *E. coli*.[28] Figure 1.1 presents the homology model of *S. typhimurium* EAL.

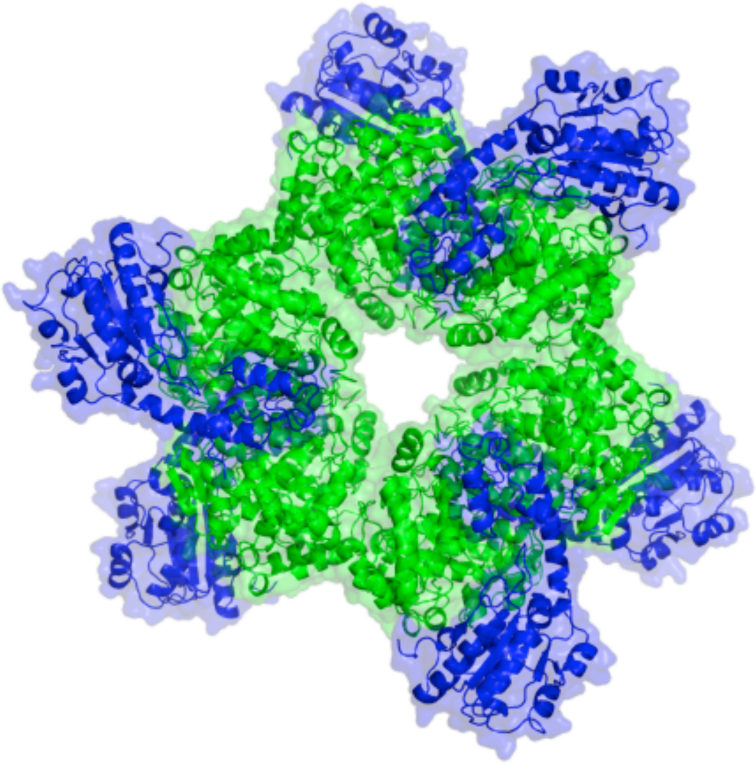

Figure 1.1 Modeled Structure of *S. typhimurium* EAL. Cartoon representation of the homology model structure of *S. typhimurium* EAL $\alpha_6\beta_6$ oligomer shows EutB subunits in green and EutC subunits in blue. The secondary structure and surface of the protein are rendered by using PyMOL.

1.2 Structure of B_{12}

EAL initiates the catalytic cycle with the homolytic splitting of the cobalt-carbon bond of coenzyme-B_{12} and harnesses the generated radicals to achieve catalysis. Coenzyme B_{12} and its derivatives are unique for the cobalt-carbon bond, which was the the first metal-carbon bond discovered.[29] Coenzyme B_{12}, a water-soluble molecule, is structurally the most complex cofactor.[27] Figure 1.2 shows the X-ray structure of coenzyme B_{12}, which is divided into three parts. The heart part of the coenzyme is a planar corrin ring with a cobalt atom bound with four nitrogens from four linked pyrrole subunits. Below the corrin ring is a covalently-bound lower axial ligand, which has the 5,6-dimethylbenzimidazole group (DMB) at its terminus. The DMB forms the "lower" axial ligand to the cobalt ion in AdoCbl. Above the corrin ring is the 5'-deoxyadenosyl group, which is axially coordinated to the cobalt ion in the "upper" position. Substitutions of the upper 5'-deoxyadenosyl axial ligand with –CN, -CH_3, and –OH create B_{12} derivatives: cyanocobalamin (vitamin-B_{12}), methylcobalamin and hydroxocobalamin.[30]

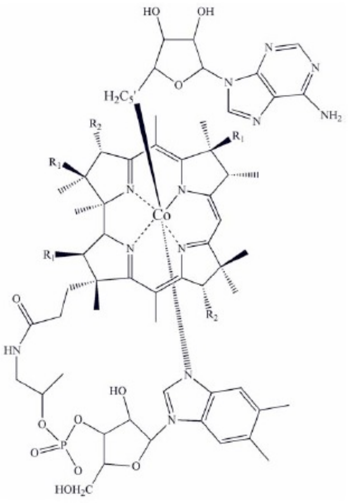

Figure 1.2: Structure of coenzyme B_{12}.

1.3. Minimal mechanism of catalysis for EAL

Figure 1.3 shows the minimal mechanism for EAL catalysis, which consists of six steps. The substrate, intermediate radical species, and organic product, are depicted in Scheme 1.1. The cycle begins with the homolytic cleavage of the cobalt-carbon bond in coenzyme B$_{12}$, triggered by binding of ethanolamine, leading to the low spin, S=1/2 Co(II) in cobalamin and the proposed S=1/2 5'-deoxyadenosyl radical. Following the initial radical generation, the C5' radical center of the 5'-deoxyadenosyl abstracts a hydrogen atom from the C1 carbon of the substrate (first hydrogen atom transfer, HT1), which forms 5'-deoxyadenosine and the substrate radical (Scheme 1.1).[13, 31] Subsequently, the substrate radical rearranges to a product radical (Scheme 1.1) in a detectably irreversible step.[32, 33] The product radical reacts by abstracting a hydrogen atom from the C5'-methyl group of 5'-deoxyadenosine (second hydrogen atom transfer HT2), which produces a diamagnetic product species and reforms the 5'-deoxyadenosyl radical. Following the HT2 step, the 5'-deoxyadenosyl radical recombines with Co(II) to regenerate the intact coenzyme,[34] and the release of products acetaldehyde (Scheme 1.1) and ammonia completes the cycle.[35]

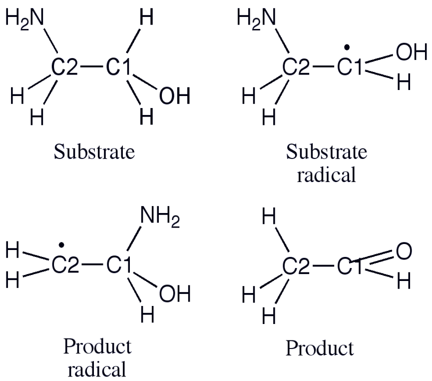

Scheme 1.1 Molecular structures of substrate, substrate radical, product radical and product.

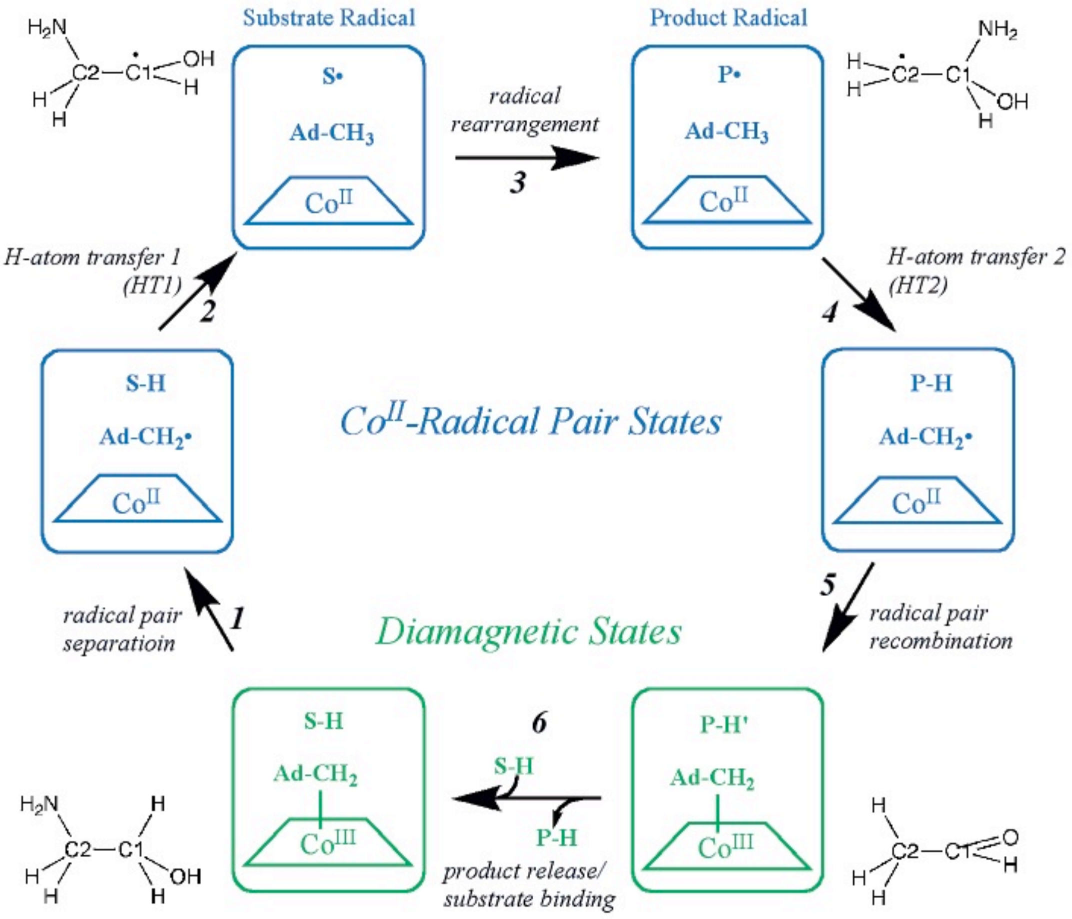

Figure 1.3. Minimal mechanism of catalysis for coenzyme B_{12}-dependent ethanolamine ammonia-lyase (EAL).[36] The forward direction of reaction is indicated by arrows. Ethanolamine binds to the holoenzyme (EAL and its cofactor, B_{12}) and initiates the reaction through six steps, which are: (1) homolytic cleavage of Co-C bond and radical pair separation, (2) first hydrogen atom transfer (HT1) to 5'-deoxyadenosyl, accompanying radical migration to substrate, (3) radical migration from C1 to C2 and amino group migration from C2 to C1, (4) second hydrogen atom transfer (HT2) from 5'-deoxyadenosyl to C2, (5) radical migration from 5'-deoxyadenosyl back to Co(II) and recombination of Co(III)-carbon bond (6) product release and substrate binding for next catalytic cycle. In this diagram, S-H represents bound substrate, $S^•$ represents substrate radical, $P^•$ designates product radical and P-H designates diamagnetic products. Coenzyme B_{12} is depicted as a Co(III) centered in a square connecting Ad-CH_2, which presents the 5'-deoxyadenosyl axial ligand. Ad-$CH_2^•$represents 5'-deoxyadenosyl radical and Ad-CH_3 represents 5'- deoxyadenosine. For clarity, the lower axial ligand is not shown. The box containing coenzyme B_{12} and substrate represents EAL.

1.4 EPR studies on the kinetics of EAL catalyzed Co(II)-substrate radicals

In the EAL catalytic reaction cycle, shown in Figure 1.3, the Co(II)-substrate radical pair intermediate accumulates during steady-state turnover on the substrate ethanolamine.[37, 38] These radical pair states can be cryotrapped, detected and characterized by using multiple electron paramagnetic resonance (EPR) techniques.

Recently by using time-resolved EPR, a "dynamical transition",[39] defined as a rapid increase in protein dynamics, was observed for the ethanolamine generated Co(II)-substrate radical pair decay at a sharp temperature range (207 -214 K).[36] A transition in the solvent was also detected around 210 K,[40] which is in the protein "dynamical transition" range. Due to the overlap of transition temperatures, a coupling between the solvent transition and a dynamical transition in the reactivity of the substrate radical in EAL is proposed. The correlation of solvent dynamics with an adiabatic reaction inside the protein is highly significant. This dissertation aims to probe the nature of the coupling and to elucidate the mechanism, from both the solvent and protein viewpoints.

The techniques are introduced and high-resolution spectroscopic studies of EAL are reviewed in **Sections 1.6** and **1.7**.

1.5 The "glass" transition of proteins and the role of solvent

Hydrated proteins undergo a dynamical transition at a temperature ranging 180-220 K, and this is known as protein "glass" transition.[41, 42] In the neighborhood of the temperature, proteins experience striking changes in the internal atomic fluctuations with reduced amplitudes and increased time scale. These abrupt transitions were observed by many different experimental techniques and theoretical simulations. Experimentally, for instance, Mössbauer spectroscopy studies showed a remarkable increase in atomic motion of the iron atom in sperm whale metmyoglobin around 200 K.[43] Inelastic neutron scattering studies also demonstrated that there is a dynamic transition in the structural fluctuations of myoglobin from the vibrational motion below 180 K anharmonic modes of motion above 180 K, on the 0.1 to 100 ps time scale.[44] X-ray crystallographic studies showed that the mean-square displacement (MSD) of back-bone of myoglobin versus temperature plot changes in slope around 200 K.[45] Theoretically, molecular dynamics simulations probed a glass-like transition in atomic fluctuations of carboxy-myoglobin protein around 210 K,[46] which is in accord with experimental results.[44] The "glass" transition is a common feature of protein dynamics, and its influence on protein functions with variety of roles is tremendous, therefore, it is significant to understand its origin. In summary of previous studies, it was speculated that protein ‘‘glass’’ transition originates in the protein itself, the bulk solvent, the hydration shell (a layer of water molecules which cover the protein surfaces) or a combination of them.[47-50]

The properties of the solvent around the protein were investigated to probe the origin of the protein dynamical transition. Infrared spectroscopy and calorimetry revealed a broad transition between 180 and 207 K in mobility and specific heat of hydration water in myoglobin crystals and solutions.[47] Hydrogen-bond network among protein and water is proposed to be the cause.[47] Simulation studies, by manipulating the temperatures of the solvent and protein respectively, showed that solvent mobility plays a major role in the atomic fluctuations of protein above 180 K.[51] Like in other simple glass-formers (sucrose, glycerol and small polymers), two relaxation processes of the solvent were also examined in hydrated proteins from the temperature dependent Arrhenius plot:[52, 53] The α-relaxation in the bulk solvent and β-relaxation in the protein hydration shell. Rich experimental data showed that above 200 K, the α-relaxation is faster, around 200 K, they are inseparable, and below 200 K, the β-relaxation is faster than the α-relaxation, leading to a molecular mechanism which suggests that the protein "glass" transition is caused by the β fluctuations in the hydration shell which engenders the α-relaxation at the transition temperature.[54, 55] Regardless of these reports, Lee and Wand presented a different viewpoint.[56] In the experimental studies on the dynamics of side chains in a calmodulin-peptide complex as a function of temperature by using NMR relaxation methods, they ascribed the low temperature "glass" transition of the protein to its internal motion. Accumulating experimental and computational observations from various sources, the role of solvent on protein "glass" transition is still elusive.

In this dissertation, EPR measurements on the kinetics of Co(II)-substrate radical pair decay extend previous temperature-dependence studies of the decay from 217 to 190 K, to ultra-low temperatures (173-187 K), to address the dynamical transition in EAL, and the role of solvent in the radical rearrangement reaction. Changes in the temperature dependence of the kinetics will be correlated with known changes in the properties of the solvent dynamics.

1.6 Continuous-wave electron paramagnetic resonance (EPR) spectroscopy

Basic principles. Continuous-wave electron paramagnetic resonance (CW-EPR) was first discovered by Zavoisky in 1945.[57, 58] EPR is a technique that detects the electromagnetic resonant absorption of chemical species possessing unpaired electrons (S>0). The sensitivity of the EPR spectral features to molecular orientations and motions, and the surrounding environment allows it to be widely applied in chemistry, physics, biology and medicine.[59, 60] The basic principle of EPR is the electron Zeeman effect. Quantum mechanically, in an external magnetic field B_0, the electron spin (down and up) aligns parallel (m_s = -½) or antiparallel (m_s = +½) to the field. Eq. 2.1.1 shows the energy of the electron:

$$E = g\,\mu_B\,B_0\,m_s \qquad \text{Eq. 2.1.1}$$

where g is the electron g-factor and μ_B is the Bohr magneton. The energy separation between the two m_s states is $\Delta E = g\ \mu_B\ B_0$. By absorbing or emitting electromagnetic radiation with a frequency ν, which satisfies:

$$h\nu = \Delta E = g\ \mu_B\,B_0 \qquad \text{Eq. 2.1.2}$$

where h is the Planck constant, a transition between the two states occurs. In thermal equilibrium, the populations at the two states follow the Boltzmann distribution, and the ratio is shown in Eq. 2.1.3:

$$\frac{n_{+1/2}}{n_{-1/2}} = e^{-\Delta E/RT} \qquad \text{Eq. 2.1.3}$$

where $n_{+1/2}$ and $n_{-1/2}$ are the number of spins in the upper and lower energy levels, ΔE is the energy difference between the two states, R is the gas constant and T is the absolute temperature. Eq. 2.1.3 shows the ratio is less than unity at thermal equilibrium. At room temperature (295 K), for instance, the ratio of the two populations is 0.998 in a fixed magnetic field with a typical value of 3400 Gauss, indicating the spins are distributed approximately equally at the two energy levels. To achieve equilibrium, excited spins at a higher energy level return from m_s = +½ states to m_s = -½ states through electron spin-lattice relaxation and an overall absorption of electromagnetic radiation is observed. Sweeping the microwave frequency is difficult to fulfill in experiments; therefore, the magnetic field is varied to bring the sample into resonance at a fixed microwave frequency. To minimize the background noise, a field modulation with a common frequency (usually 100 kHz) is applied and then phase sensitive detection in the signal channel shows the EPR signals by comparing the modulated signals with a reference signal having the same frequency and phase as the field modulation.[61] EPR spectra are recorded as the first-derivative of absorbance spectra as a function of magnetic field.

In this dissertation, EPR spectra for the common spin probe, TEMPOL and Co(II)-substrate radical pair are discussed in detail in the following sections.

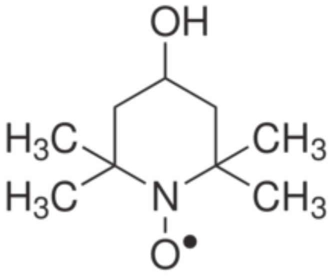

Figure 1.4. Structure of TEMPOL.

TEMPOL EPR spectroscopy. Figure 1.4 shows the structure of TEMPOL. The unpaired electron is coupled with the ^{14}N nucleus. The typical X-band EPR lineshape of mobile TEMPOL is generated by the hyperfine coupling between the unpaired electron ($S = 1/2$) and the ^{14}N nucleus ($I = 1$) in the N-O group, leading to three lines corresponding to m_{I} = -1, 0, and 1 of the ^{14}N nucleus. Eq. 2.1.4 shows a representation of the Hamiltonian that characterizes the nitroxide EPR spectrum:

$$\mathbf{H} = \mathbf{EZ} + \mathbf{NZ} + \mathbf{HF} \qquad \text{Eq. 2.1.4}$$

In Eq. 2.1.4, **EZ** is the electron Zeeman term, **NZ** is the nuclear Zeeman term, and **HF** is the electron-nuclear hyperfine coupling term. For powder EPR spectrum of

TEMPOL, besides the contributions listed in Eq. 2.1.4, a term called anisotropic hyperfine (AHF) is considered. In rigid environment, it spreads the energy separation bands, leading to a broadening effect in the EPR spectra. Figure 1.5 shows the diagram of energy levels of nitroxide radicals in a static magnetic field.

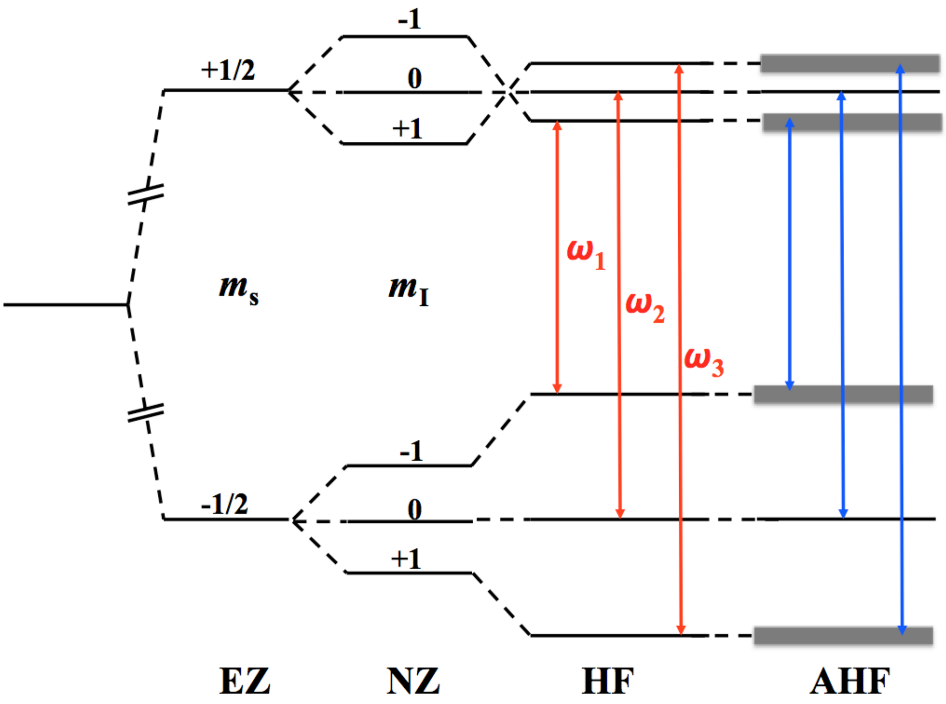

Figure 1.5. Energy levels of nitroxide radicals in a static magnetic field. According to the selection rule, transitions caused by the hyperfine coupling (HF) are marked in red, and by the anisotropic hyperfine coupling (AHF) are marked in blue.

TEMPOL mobility observed from EPR lineshapes. The EPR spectra are sensitive to the probe tumbling motions on time scales of $10^{-10} – 10^{-7}$ s, which cover time scales that are in common with protein dynamics in solutions. At low temperature, the spin probe (0.2 mM, in water) is in the slow motion regime and the spectrum presents a typical powder line width, with an outer line width, $2A_{zz}$=76 Gauss=210 MHz, where A_{zz} denotes the *z*-component of the anisotropic hyperfine tensor. When the temperature increases, the solvent environment becomes mobile, which allows faster spin rotational diffusion, thus, the anisotropic interactions are averaged to a zero value in the EPR spectrum, giving rise to three distinct sharp EPR lines, with an outer line width, $2A_{\text{iso}}=34$ Gauss, where A_{iso} is the orientation-independent isotropic hyperfine coupling constant.

Figure 1.6 shows two CW-EPR spectra of 0.2 mM TEMPOL in pure water at 180 and 250 K, that display the dependence of line shape on spin label mobility.

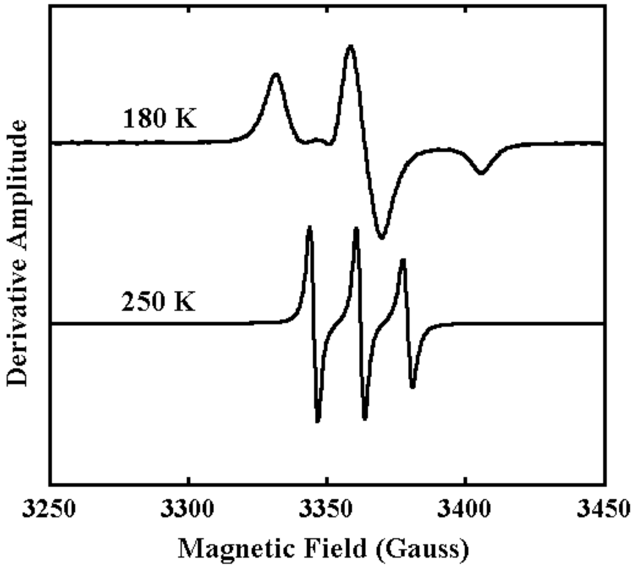

Figure 1.6. EPR spectra of 0.2 mM TEMPOL in pure water at 180 K and 250 K respectively.

Co(II)-substrate radical pair EPR spectroscopy. In the EAL catalytic reaction cycle shown in Figure 1.3, Co(II)-radical pairs are shown in blue. Figure 1.7 shows a CW-EPR spectrum of the Co(II)-substrate radical pair intermediate at 120 K. This spectrum consists of the signal from Co(II), which is prominent at magnetic field that corresponds to the perpendicular component of the g-tensor ($g_{\perp} \sim 2.3$)[62, 63] and the signal of the organic radicals around $g \sim 2.003$. With respect to the magnetic field, the $g_{\perp}$ signal of Co(II) appears at 290 mT, and the signal of the radical appears at 337 mT. The conversion is derived from Eq. 2.1.2, where the microwave frequency ν is 9.447 GHz. Co(II) and the organic radical are coupled, and therefore, perturbations in signals for each paramagnetic species are generated, leading to unresolved doublet splitting and inhomogeneous line broadening in the EPR spectrum.[64]

Previous studies show that the substrate radical ($S^{\bullet}$) is the only EPR detectable state, and that the Co(II)-C1 separation is 11 ±1 Å in the (*S*)-2-aminopropanol-generated Co(II)-substrate radical pair,[65, 66] and 9.3 ±1 Å in the ethanolamine-generated Co(II)-substrate radical pair.[65, 67] The (*S*)-2-aminopropanol radical shifts 2 Å further to Co(II) compared with ethanolamine radical. This is consistent with the separation, which is approximately 2 Å away from the cofactor, caused by the methyl substitution at C2 in (*S*)-2-aminopropanol.

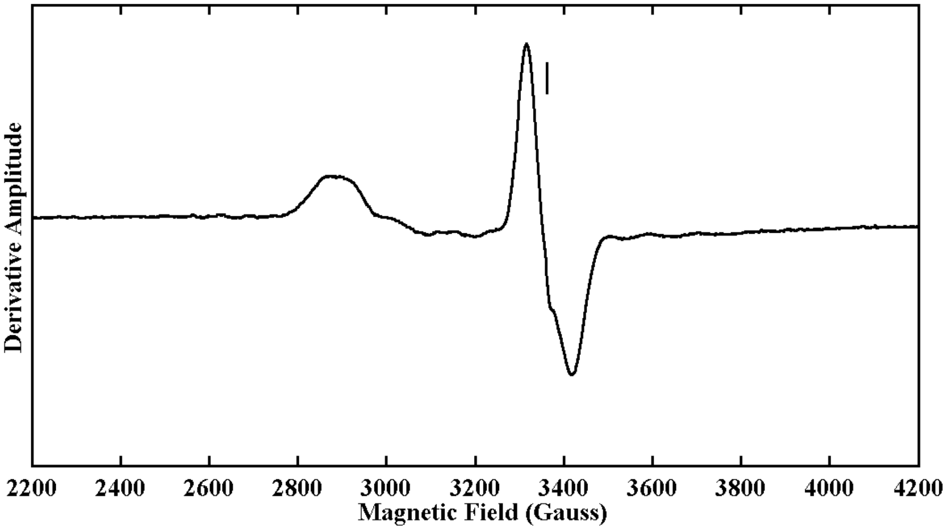

Figure 1.7. Representative EPR spectrum of the Co(II)-substrate radical pair intermediate generated with ethanolamine and cryotrapped in EAL. The free electron resonance position at $g = 2.0$ is shown by the vertical bar. *Experimental Conditions:* microwave frequency, 9.447 GHz; temperature, 120 K; microwave power, 20.43 mW; magnetic field modulation, 1.0 mT; modulation frequency, 100 kHz; time constant, 10.24 ms.

1.7 Electron spin echo envelope modulation (ESEEM) spectroscopy

Electron spin echo envelope modulation (ESEEM) is a pulse technique of EPR spectroscopy.[68, 69] ESE and ESEEM methods have been applied to characterize the solvent around EAL, by using TEMPOL.[70] Frozen samples (6 K) containing paramagnetic spins are placed in an external magnetic field (B_0), and microwave pulses with a variable magnetic field $B_1 \perp B_0$ are applied to manipulate the electron magnetization vector (M). Figure 1.8 shows the alignment of B_0, B_1. Without pulses, if M is not parallel to B_0, the electron magnetization performs Larmor procession about the direction of B_0 with a frequency given by Eq. 2.1.5:

$$w_L = \frac{2\mu_e}{\hbar} B_0 \qquad \text{Eq. 2.1.5}$$

where μ_e is the electron magnetization moment. If the microwave pulses with a frequency of ω_L are applied, the system approaches resonance, and the electron magnetization with Larmor precession and the oscillating magnetic field $B1$ are static in the lab frame (the rotating frame). In this frame, the electron magnetization vector can be treated as being rotated by specific angles (typically, π/2 or π) about the $B1$ axis.

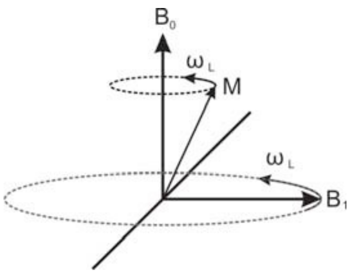

Figure 1.8. The alignment of $B0$ and $B1$ fields in lab frame. ***M*** is the electron magnetization vector and it performs Larmor precession about the direction of B_0, when B_1 is not applied.

A two-pulse sequence shown in Figure 1.9A is widely utilized to study the spin systems. Figure 1.10 shows the formation of a two-pulse echo. The net magnetization vector, shown in a red arrow in Figure 1.10A, is assumed to be initially along the B_0 axis (z-axis). Under the action of a $\pi/2$ pulse along y-axis, the magnetization vector is rotated by 90^o to the x-axis (Figure 1.10B). In the duration of τ between the first and second pulse, the off-resonance spins species induce the electron magnetization vectors to dephase on the x-y plane in the direction indicated in arrows (Figure 1.10C). The π pulse flips the individual magnetization components by 180^o in the x-y plane (Figure 1.10D) and after a time τ, the vectors "refocus" and a primary echo is formed (Figure 1.10E). The echo signal amplitude decays as a function of τ. In the time τ between two pulses, the transverse magnetization vectors are stored in this plane within the phase memory time, T_M, which describes how quickly the net magnetizations "fan" out 360 degrees to evolve into random precession. ESEEM records the waveforms evolving as a function of the time interval τ to reveal the nuclear modulation effect. By analyzing this dependence of echo amplitude on the time interval τ, values of T_M can be obtained. Taking into account couplings of hyperfine and nuclear quadrupole of adjacent nuclei with the spins, which contribute to the echo signal, two-pulse ESEEM is a sensitive method to report the local environment of the unpaired electrons. A disadvantage of the two-pulse ESEEM is that the echo decays within T_M, which is short (in the order of a few microseconds), therefore, the echo is unable to be monitored for a long time and low frequency modulations are not observed. This drawback is overcome by applying a three-pulse sequence, which provides a longer acquisition interval for monitoring the echo.

Figure 1.9B shows the scheme of the three-pulse sequence. Three identical microwave pulses ($\pi/2$) at times 0, τ, and $\tau + T$ are applied to the spin system and a three-pulse, or stimulated echo signal is formed at $2\tau + T$. The echo envelope modulation is recorded as a function of T at a fixed value of time τ between the first and second pulse. During the second and third pulse, the longitudinal magnetization components relax along the z-axis to return to equilibrium within time T_1, which is also defined as spin-lattice relaxation time. It is determined by the surrounding environment of the spin and T_1 is longer than T_2.

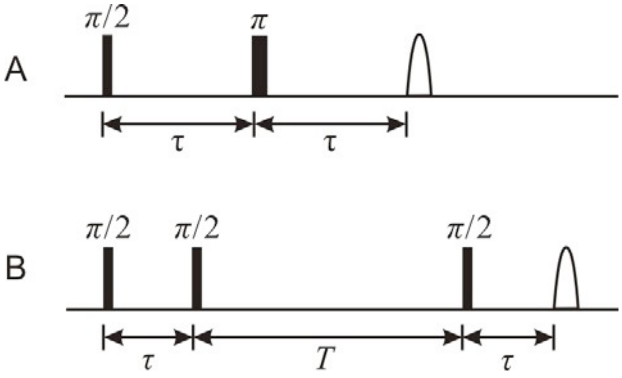

Figure 1.9. Pulse timing diagrams for the two- and three-pulse ESEEM pulse sequences. A. Two-pulse sequence: $\pi/2 - \tau - \pi - \tau -$ *detection*. B. Three- pulse sequence: $\pi/2 - \tau - \pi/2 - T - \pi/2 - \tau -$ *detection*.[71]

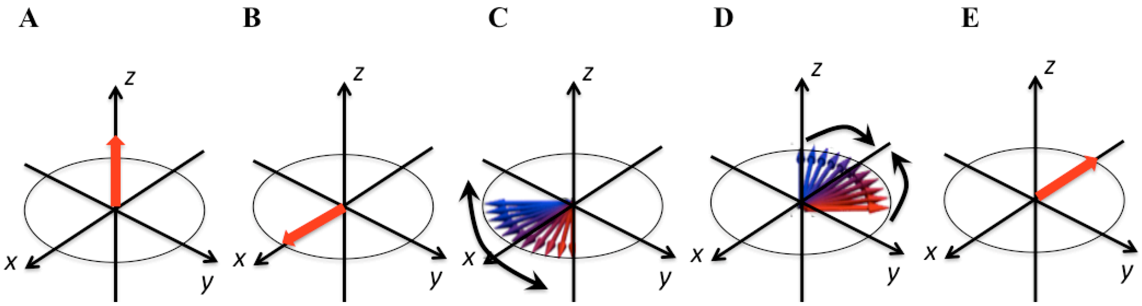

Figure 1.10. The formation of the two-pulse spin echo: (A) the initial state of the net magnetization vector, (B) after the first ($\pi/2$) pulse, (C) the dephasing of the magnetization vectors between the first and second pulse, (D) after the second (π) pulse, (E) the recombination of the magnetization vectors and the primary echo is formed on the $-x$-axis. The B_0 is along the z-axis.

1.8 Outline of dissertation

In this dissertation, the microscopic mesodomain structure of frozen sucrose-water systems with and without the presence of EAL was investigated by using CW- and pulsed-EPR techniques. The kinetics of Co(II)-substrate radical pair decay at ultra low temperatures (173-187 K) by using time-resolved EPR spectroscopy was also investigated.

Chapter 2 describes the heterogeneous ordered-disordered structure of the mesodomain in frozen sucrose-water mixtures by examining TEMPOL mobility, relaxation times and effective concentrations by using multiple EPR spectroscopies.

Chapter 3 introduces the microscopic structure of the mesodomain and hydration shell in frozen sucrose-water-EAL systems by using a combination of CW- and pulsed-EPR techniques.

Chapter 4 investigates the Co(II)-substrate radical pair decay at four ultra low temperatures (173, 177, 183 and 187 K) and constructs three kinetic models to characterize the protein dynamics at low temperatures. Further links between protein “glass” transition and the dynamics of the solvent are the goal.

Chapter 2

Heterogeneous Ordered-Disordered Structure of the Mesodomain in Frozen Sucrose-Water Solutions Revealed by Multiple Electron Paramagnetic Spectroscopies

2.1 Background and introduction

2.1.1 Mesodomain and temperature-composition (*T*-c) diagram

In the food and pharmaceutical industries, amorphisation processes are widely conducted to preserve perishable materials.[72-74] These applications attract interest in studies of glassy products. To model these amorphous behaviors, sucrose-water systems have been selected and investigated at a wide range of temperatures for over five decades.[75] It is reported that by freezing unsaturated aqueous solutions of sugars at rates of $<10^3$ Kelvin per second (K/s), water-ice crystals grows and exclude the solute sugar, resulting in a heterogeneous state featured with domains.[76] Their microstructures were shown in electron microscopy (EM) as web-like filaments after removal of the crystalline ice by sublimation, and the boundaries were clearly shown in the electron micrograph.[76-78] Thermodynamic properties and phase behaviors of sucrose-water systems during cooling were most frequently represented in the temperature-composition (*T*-*c*) state diagram, as shown in Figure 2.1. This diagram, incorporating the published calorimetric measurements,[79] shows that during freezing at infinitely slow rate or the slow cooling rate limit (approximately, $<10^2$ K/s), water in unsaturated sucrose solutions crystallizes, and the formation of ice proceeds in the direction, denoted by solid arrows in Figure 2.1 along the melting curve (the liquidus curve), resulting in increasing sucrose concentrations at the boundaries created by the water-crystalline domains. Referring to the equilibrium solubility of sucrose, the solvent begins to crystallize when the temperature drops to a theoretical eutectic point, T_e. This trajectory ends when the temperature reaches the glass temperature, T_g'≈241 K,[76] at which the sucrose is maximally freeze-concentrated, with the value of 80 ±5% (w/w) [120 ±8% (w/v)].[80] At "slow" ($<10^3$ K/s) freezing rate, a trajectory follows the liquidus curve marked with dashed line and arrows. Similarly, beginning with the formation of ice, proceeding after that, the volume of mesodomain decreases, and the sucrose approaches to higher concentrations. The curve meets with glass transition line at T_g''<T_g', at which the mesodomain eventually forms a glass. In Figure 2.1, it shows that concentrated or super-saturated sucrose solutions can transform into homogenous glasses during cooling. In our study, the cooling rate is approximately 10 K/s or lower. We found that solutions with low concentrations of sucrose (≤50% (w/v) form heterogeneous states, and those with high concentrations (>50% (w/v)) form homogeneous glass. As reference, at ultra-fast cooling rates ($>10^4$ K/s), pure water forms glass at 138 K.[81]

To gain more information of the mesodomain, TEMPOL, a paramagnetic nitroxide (S=1/2) molecule is chosen as a probe, due to its relatively small size (effective diameter, approximately 7 Å). It also resides in between the ice crystallines in frozen aqueous solutions. Therefore, in situ electron paramagnetic resonance (EPR) studies, it is widely used to provide insight into the dynamics of its environment.[82] Bhat and his coworkers have used it to characterize the formation of vitrified water[40, 82] and glycerol solutions[82] at low temperatures. They applied continuous-wave (CW) EPR spectroscopy and showed dynamical transitions of water by characterizing changes of line shapes of TEMPOL induced by tumbling of spins at varied temperatures. They reported T_g for pure water is 136 K[40], and this is comparable with 138 K, mentioned above, which was determined by calorimetric techniques.[81] They also measured T_g' values for frozen solutions with different amounts of glycerol.[82] These results indicate that high-resolution EPR spectroscopic techniques can serve as powerful tools to explore mesodomain structures of sugar-water systems.

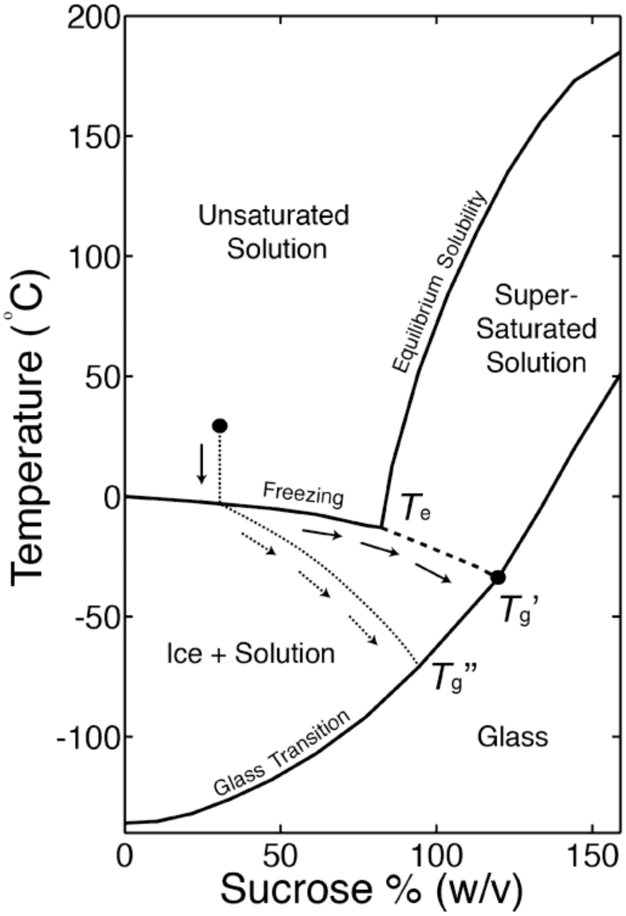

Figure 2.1. **Equilibrium temperature-composition phase diagram for water-sucrose mixtures, and overlaid cooling-rate dependences of the relations.** Representative cooling trajectories from a room temperature solution of 30% sucrose (w/v) are depicted. When the temperature drops to the freezing line, water crystallizes and the sucrose concentration increases around the water-crystalline domains. As temperature continues to drop, the trajectory follows the equilibrium liquidus curve for infinitely slow cooling (solid arrows) through the eutectic (T_e), and reaches a maximally freeze-concentrated state at the glass transition (T_g’). For finite cooling rates of <10^3 K/s, the trajectory follows an apparent liquidus curve (dashed line, arrows) and forms a glass at a lower temperature, T_g’’. At T_g’ (or T_g’’) the sucrose is maximally freeze-concentrated in the mesodomain, at the boundaries of the ice crystalline regions.

The location and distribution of solutes in sucrose-water systems are characterized in detail in this chapter. Since the presence of sucrose can affect the structural and dynamical behaviors of proteins, these studies are also of significance to further understand protein function.[83-85] Here, we applied a set of spectroscopic techniques, including continuous-wave and pulsed EPR and relaxation approaches to probe the microscopic structure of frozen aqueous sucrose solutions with TEMPOL. Sucrose concentrations vary from 0 to 75% (w/v). The measurements show detailed information about heterogeneity of the mesodomain in different aspects.

2.1.2 Sample preparations and experimental setup

Sample preparation. Sucrose (≥99.5%, Sigma-Aldrich, St. Louis, MO), deuterated sucrose ([6,6'-$^{2}H_2^{fru}$] sucrose (≥99.8%, Omicron Biochemicals, Inc., South Bend, IN) and TEMPOL (4-Hydroxy-TEMPO, Sigma-Aldrich, St. Louis, MO) were purchased from commercial resources and used as received. Water (Nanopure, Siemens) with resistivity of 18.2 MΩ was used to prepare all of the samples. Natural abundance or deuterated sucrose were mixed with water and TEMPOL. The concentrations of sucrose vary from 1-75% (w/v) and the final concentration of TEMPOL is 0.2 mM [0.0034% (w/v)]. A set of control samples with different concentrations of TEMPOL (100 mM, 33.3 mM, 11.1 mM, 3.70 mM, 1.23 mM, 0.41 mM, and 0.12 mM) in 60% (w/v) sucrose was prepared. Another control sample with 30% (w/v) [6,6'-$^{2}H_2^{fru}$] sucrose and 30% (w/v) natural abundance (^{1}H) sucrose [total, 60% (w/v) sucrose] (red square) was also made. All of these samples were degassed using freeze-pump-thaw procedures three times and were loaded into 4 mm o.d. EPR tubes (Wilmad-LabGlass, Buena, NJ) which were vacuumed and backfilled with argon (Ultra high purity gases, NexAir). Samples were first chilled in a 252 K freezer for 12 hours, and subsequently plunged into liquid nitrogen (LN_2) for storage.

CW-EPR spectroscopy. EPR spectra were collected by using a Bruker Biospin ElexSys E500 EPR spectrometer. Temperature was monitored and stabilized with an Oxford Instruments cryostat with continuous N_2 flow and a Bruker ER4131VT temperature controller. Exept for samples with 60%, 75% (w/v) sucrose content which were conducted at a lower power of 0.02 mM, spectra of different temperatures arranging from 160 K to 270 K were obtained under following conditions: 9.41 GHz of a microwave frequency, 1024 points, 3320 Gauss of central field, 280 Gauss for sweeping width, 30dB power (0.2mW), 2 Gauss modulations, 10.24 ms sample time, 2.56 ms time constant, 4-36 scans. Temperature was raised for every 5 K in the measured temperature range (160 K-270 K). Before starting to collect spectra at each temperature, when the assigned temperature was reached, 5 more minutes were waited for the temperature to stabilize and the equilibrium of samples.

Simulations of the experimental CW-EPR spectra were carried out using the software, EasySpin,[86] based on the assumptions of random rotational tumbling of the spin probe. The overall fittings of spectra at different temperatures were obtained by varying the corresponding correlation time, τ_c and other parameters (g_{xy}, g_{xy}, g_z, A_{xy} and A_z) in some specific ranges: g_{xy}=2.009-2.010, g_z=2.004-2.005; A_{xy}=6.4-7.5 Gauss, A_z=36-39 Gauss, respectively. Spectra were performed with a single component, which accounts for one rotating species of the spin probe. However, a few selected spectra, collected at T_t, defined as the temperature at the termination of the transition, required two component fittings, which correspond to fast and slow motions of the spin. Here, we chose a spectrum of the sample with 10% sucrose at 255 K as a representative. The fitting shows that the normalized ratio of the two components populations (component1: component2) is 0.6:0.4, and the correlation times are τ_{c1} =10 ns and τ_{c2} =2.6 ns.

Spin-lattice relaxation time measurement from dependence of ESE amplitude on pulse repetition rate. All electron spin echo (ESE) experiments were conducted on a home-built X-band pulsed EPR spectrometer at 6 K. The two-pulse sequence used is P_1—τ—P_2—τ—echo, where P_i is 20 ns. The echo intensity was recorded by varying pulse repetition rate.[68, 87] As the pulse sequences repeat with a high frequency, less time for the z magnetization component that was projected into the x-y plane to recover, the echo amplitude decreases. Thus, according to the dependence of the echo amplitude as a function of repetition rate, shown in Eq. 2.1,[68, 87] the longitudinal, or spin-lattice, relaxation time, T_1, can be determined:

$$V(t_{rep}) = V_0\left[1 - \exp\left(-\frac{t_{rep}}{T_1}\right)\right] \qquad \text{Eq. 2.1}$$

where V is the ESE amplitude, t_{rep} is the repetition period (inverse repetition rate) and V_0 is the maximum ESE amplitude as $t_{rep} \rightarrow \infty$. Experiments were performed under conditions: a microwave frequency of 8.752 GHz, magnetic field of 3115 G and τ value of 504 ns. The pulse sequence repetition rate varied from 1 to 1000 Hz. Between the pulse sequences; dwell times were tuned for the spin system to return to equilibrium.

Phase memory time measurement by using two-pulse ESEEM. The echo is created by a pulse sequence P_1—τ—P_2—τ— echo (P_1=P_2), with varying τ.[88] In the two-pulse ESEEM experiments on samples with different sucrose compositions, the area of the echo was integrated, monitored for stepped τ, generating a time-resolved ESEEM spectrum. These ESEEM data were collected under the following conditions: microwave frequency, 8.752 GHz; magnetic field, 3115 G; repetition rate, 5 Hz; temperature, 6 K. The phase memory time, T_M, and exponent, n, were obtained by fitting the decay of the echo with a stretched exponential equation shown as:[68]

$$V(2\tau) = V(0)\exp\left[\left(-\frac{2\tau}{T_M}\right)^n\right] \qquad \text{Eq. 2.2}$$

where $V(2t)$ is the echo amplitude at a time, $2t$, after P_1, and $V(0)$ is the echo amplitude at t=0.

Three-pulse ESEEM. A typical three-pulse sequence, P_1—τ—P_2—T—P_3 —τ— echo ($P_i=\frac{\pi}{2}$),[68] was used, with varying T. The ESEEM experiments were performed at 6 K at microwave frequency 8.752 GHz, magnetic field 3115 G, τ=226 ns, and a pulse sequence repetition rate 100 Hz. With t = 226 ns, proton modulations can be significantly suppressed, and weakly-coupled ^{2}H modulation can be effectively optimized. The ESEEM waveforms as a function of τ+T on samples with deuterated sucrose were recorded. On the basis of Mims theory,[69] a computationally efficient software, OPTESIM,[71] developed by Sun. et al., was used to simulate the collected spectra. Here, we modeled the system by assuming a single ^{2}H coupled to the electron with adjustable hyperfine coupling parameters. The simulations show that the isotropic part of the hyperfine coupling tensor, $A_{\mathrm{iso}}=0$. In the calculations, the point dipole approximation was used, and electron and nuclear dipoles were assumed to be randomly oriented by introducing an adjustable parameter, r_{en}. Here, the nuclear quadruple coupling constant, $e^2qQ/\hbar$, and electron field gradient (efg) asymmetry parameter, η, where e is the charge of an electron, q is the magnitude of the principal component of the efg tensor, Q is the nuclear quadruple moment, and $\hbar$ is the reduced Planck's constant, were fixed to 0.2 MHz and 0.1, respectively.[89] The envelope modulation depth (EMD) values, which indicate the interactions between ^{2}H in deuterated sucrose and TEMPOL, were obtained from the fittings of time domain ESEEM waveforms.

2.2 Experimental results

2.2.1 Mesodomain Mobility transition of the TEMPOL paramagnetic probe observed from EPR lineshape analysis

EPR spectra at selected temperatures in the range of 180-270 K for 0.2 mM TEMPOL in pure water and in 10 % (w/v) sucrose solution are presented in Figure 2.2. The featured peaks of the nitroxide radicals spectra originates from the interaction of the unpaired electron and nucleus, ^{14}N (nuclear spin, I=1) at its vicinity, generating ($2I+1$ = 3) of EPR lines, corresponding to the transitions between $m_{\mathrm{I}} = 0, \pm 1$ states. The motion of TEMPOL with tumbling times approximately between 10^{-10} and 10^{-7} s can be detected in

EPR, and the information is involved in the line shapes of EPR spectra.[90] In Figure 2.2, with increasing temperature, the TEMPOL mobility is much higher in the bulk solution,[91] and the spin probe tumbles more rapidly. The increasing random rotational thermal motion averages out the anisotropic effects,[90] producing narrowed EPR spectra. At 180 K, the EPR spectra shown in Figure 2.2 exhibit the typical powder pattern EPR line shapes, which are broad and rigid-limit, with an outer line width, $2A_{\mathrm{zz}}$=76 Gauss=210 MHz, where A_{zz} is the z-component of the anisotropic hyperfine tensor. At 250 K, the spin probe tumbles in the fast motional regime, and the anisotropic interactions are averaged, giving rise to isotropic EPR spectra with the outer line width, $2A_{\mathrm{iso}}$=34 Gauss, where A_{iso} is the orientation-independent isotropic hyperfine coupling constant. To quantitatively evaluate the spin mobility, simulations were performed on these EPR spectra, to obtain the correlation time, τ_{c}, which characterizes the speed of tumbling through Brownian motion.

The values of τ_{c} at different temperatures for samples with 0, 1, 3, 5, 10, 30, and 60% (w/v) sucrose contents are presented in Figure 2.3. Variations of τ_{c} as a function of temperature are divided into three common regions: (a) Within the low temperature range, which corresponds to the rigid regime at which the spin probe is immobilized, that limits the tumbling model, the τ_{c} value derived from the similar EPR line shapes is not accurately specified. The τ_{c} values in this regime are averaged and shown in Figure 2.3. (*b*) At relatively high temperatures, τ_{c} decreases sharply, demonstrating that the environment where TEMPOL resides undergoes a transition between a rigid material and one that possesses fast dynamics on the time scale of the inverse line width ($2A_{zz}^{-1}$, ~10^{-8} s). The temperature at which the transition terminates is denoted as T_t. (*c*) At temperatures above T_t, τ_c further decreases and converges to a constant value, caused by the freely rotating spin probe. The obvious discrepancy between the value of T_t and the homogeneous glass transition temperature, T_m for pure water ($T_t \ll T_m$), indicates that in our case, TEMPOL occupies an amorphous mesodomain in pure water, and in sucrose-water binary mixture as well. This is in agreement with studies of other binary solvent systems.[40, 82]

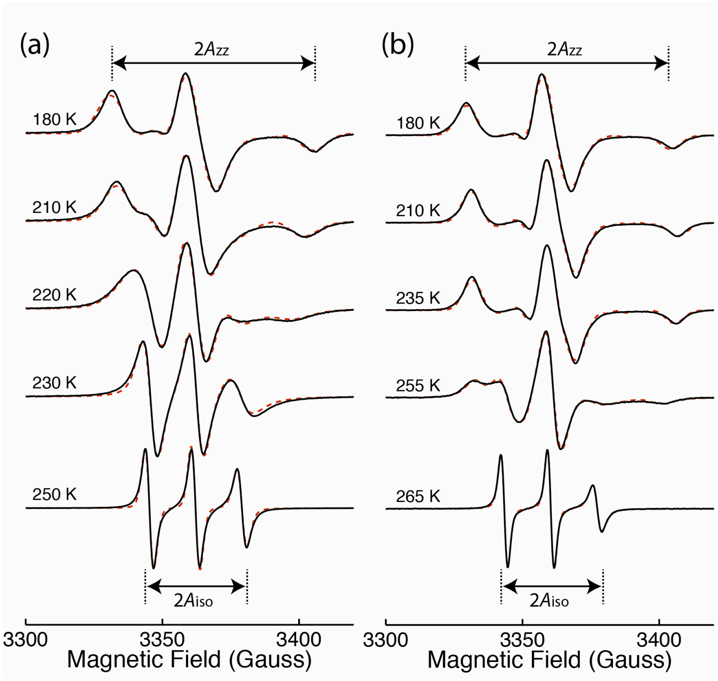

Figure 2.2. CW-EPR spectra of TEMPOL spin probe in pure water and aqueous sucrose solutions, at different temperatures, and overlaid EPR simulations (dashed line). (a) 0% sucrose (pure water). (b) 10% (w/v) sucrose. The concentration of TEMPOL is 0.2 mM (0.0034%).

In Figure 2.3, T_t for TEMPOL in pure water is 205 K, and the dependence for added 1, 3, 5, 10, 30 and 60 % (w/v) sucrose is also included. Addition of 1% (w/v) sucrose causes a large increment, 35 K, and T_t shifts to 240 K. In contrast, for ≥ 3% (w/v) sucrose, T_t increases less sharply as sucrose concentrations increase, and T_t remains a constant value of T_t=255 ±5 K. The temperature dependence of τ_c for different sucrose concentrations categorizes the mesodomain environment into two types. One is, in pure water, the mesodomain possesses a low T_t (T_t=205 K) for TEMPOL tumbling. The second type is not sensitive to sucrose concentrations, and it is common for samples with 3-50% (w/v) sucrose, characterized by a relatively high T_t (T_t=255 ±5 K).

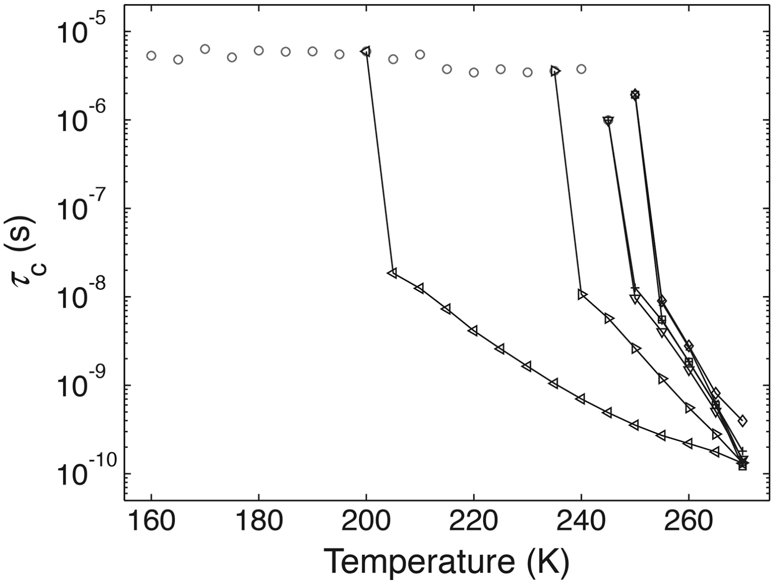

Figure 2.3. Temperature dependence of the rotational correlation time of the TEMPOL spin probe in pure water and in representative aqueous sucrose solutions. Values of τc were derived from simulations of the CW-EPR spectra. The average value of τc from the rigid limit simulations (at 5 K increments from 160 K to the mobility transition temperature) is shown (○). Symbols: (◁) 0%, (▹) 1%, (▽) 3%, (+) 5%, (△) 10%, (Å~) 30%, (◇) 60% (w/v) sucrose.

2.2.2 Relative sucrose concentration in the mesodomain from electron spin echo envelope modulation (ESEEM) spectroscopy

Here, ^{2}H ESEEM experiments were performed on samples with deuterated sucrose at 6 K to characterize the anisotropic hyperfine coupling between the unpaired electron and the nucleus, ^{2}H (I =1), in solids.[69] Larmor precession of deuterium nuclei about the external magnetic field of 3115 Gauss induced modulation of ESEEM waveforms in the time domain with a period of 480 ns, which corresponds to approximately 2.1 MHz of frequency. As the waiting time T in the three-pulse sequence increases, the amplitude of ESE decays, accompanied by a damping deuterium modulation. To demonstrate the influence of the interactions of deuterium to the electron, envelope modulation depth (EMD), also known as normalized modulation amplitude in some literature,[68] is calculated to estimate the coupling, by means of dividing the interval of the ESE amplitudes at the interpolation of the first and second peaks and the second trough by the ESE amplitude at the interpolation of the first and second peaks, where troughs and peaks are identified in simulated waveforms with magenta dots in Figure 2.4. Here, in this plot, three-pulse waveforms for three representative samples with 50, 20 and 5% (w/v) of [6,6'-$^{2}H_{2}^{fru}$]-sucrose concentrations are included. In contrast to modulated amplitude, vertical bar in the bottom panel of 5% is used to scale the unmodulated amplitude. Experimental waveforms are in black and simulated waveforms by using OPTESIM[71] are in red. Numerical calculations with OPTESIM on all of the ESEEM spectra showed slight contributions from isotropic hyperfine coupling, and therefore, indirect and non-bonded contacts between TEMPOL and the detected ^{2}H are proved. For this case of weak hyperfine coupling, the presence and spatial arrangements of deuterium nuclei surrounding the paramagnetic probe are attributed to the EMD, which is proportional to the number of the nuclei and to r_{en}^{-3}, where r_{en} is the electron-nuclear distance. Therefore, the determined EMD of the ^{2}H-involved samples can report the local concentration of sucrose around TEMPOL probe.

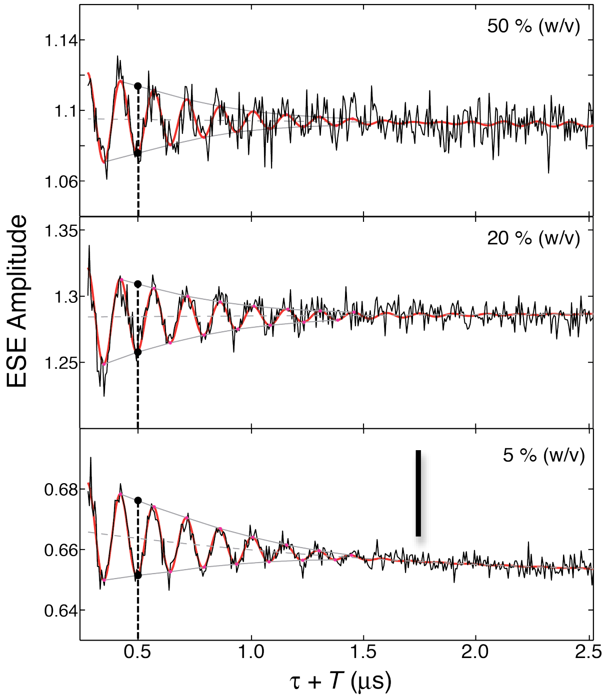

Figure 2.4. Examples EMD calculation with three-pulse ESEEM waveform of 50%, 20%, and 5% (w/v) deuterated sucrose sample. OPTESIM simulation toolbox was used to simulate the ESEEM waveforms. Experimental waveform (black) is overlaid with simulation (red line). Peaks and troughs are identified in the simulated waveform. Envelope modulation depth is then calculated based on the ESE amplitudes at the second trough and an interpolation of the first and second peaks indicated by the dashed line. Vertical scale bar in bottom panel represents 5% of the unmodulated ESE amplitude.

In Figure 2.5, the dependence of EMD on the added [6,6'-$^2H_2^{fru}$]-sucrose concentration, over a range of 1 – 75% (w/v), is presented. The EMD values are included in Table 2.1. According to the simulations, for samples with 3 – 75% (w/v) sucrose, the considerable deuterium modulation arises from the presence of a single ^{2}H nucleus coupled to the electron, situated at a distance $r_{en} \approx 6 \pm 2$ Å, on the average. Except for 1% (w/v) sucrose, within the standard deviation, these EMD values showed independence on the added concentrations of sucrose, indicating that the local concentration of sucrose surrounding TEMPOL is constant.

To assess the sensitivity of the EMD measurements to estimate local ^{2}H-sucrose concentrations, a control sample that contains 30% (w/v) [6,6'-$^2H_2^{fru}$]-sucrose and 30% (w/v) natural abundance sucrose, with a total 60% (w/v) sucrose was made. Compared to 60% (w/v) $^2H_2$-sucrose sample, this one substitutes half of ^{2}H with ^{1}H. With such high concentrations of sucrose, the sample forms homogeneous glass, and the sucrose molecules are randomly distributed. The EMD of the 1:1 ^{2}H-sucrose/^{1}H-sucrose sample is determined and marked as a red square in Figure 2.5. The EMD value is approximately half of the 60% (w/v) $^2H_2$-sucrose sample. This measurement verifies that the EMD method is responsive to significant changes in the local concentration of ^{2}H-sucrose.

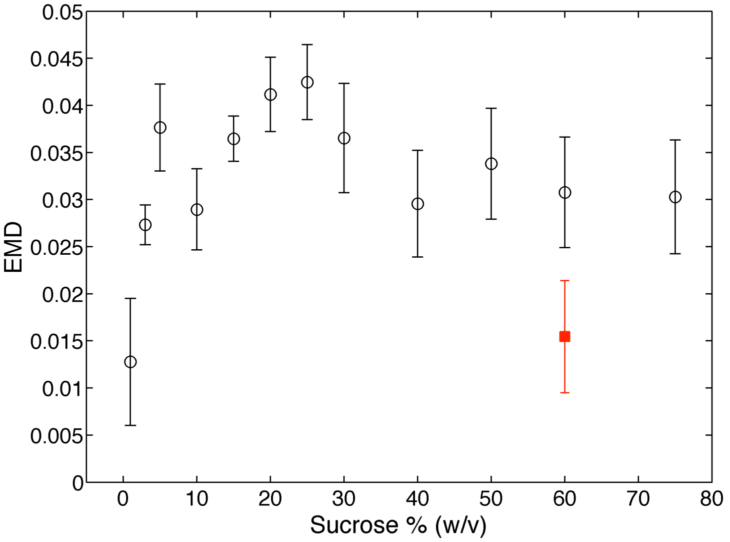

Figure 2.5. Three-pulse envelope modulation depth (EMD) of samples at different percentage (% w/v) of [6,6'-$^2H_2^{fru}$] sucrose (black). Control sample with 30 % (w/v) [6,6'-$^2H_2^{fru}$] sucrose and 30 % (w/v) regular sucrose is marked in red.

2.2.3 Relative TEMPOL mesophase concentration from spin-lattice relaxation time in sucrose solutions

Relaxation processes, which arise from interactions between the spin system and its environment, cause the decays of ESEEM signals. By examining the relaxation times, a wealth of information of the microscopic structure of the mesodomain can be provided. On the basis of the Redfield theory,[92] which specifies the interacting spins as dipolar couplings between electrons, formalisms are derived to evaluate T_1 (and spin-spin relaxation time, T_2).[93, 94] It was shown that the longitudinal, or spin-lattice, relaxation time (T_1) of spin polarization is much shorter when the volume concentration of spins increases.[68] Therefore, the values of T_1 for the samples are capable of reporting the concentrations of TEMPOL. Here, The T_1 was determined by monitoring the 2-pulse

ESE amplitude as a function of pulse sequence repetition rate at T=6 K.[87] As shown in Eq. 2.1,[87] if the pulse repetition rate is very fast, >> T_1^{-1}, the spin system is saturated, and no echo can be detected. The varying of ESE amplitudes at different repetition rates for the samples with a constant concentration of 0.2 mM TEMPOL and different amounts of added sucrose were collected, and shown in Figure 2.6. The overlaid curves are the fits of Eq. 2.1 to the data. From right to left, the concentration of sucrose increases, and the pulse repetition rate to saturate the spin system, or at which the ESE amplitude equals to zero, decreases, indicating that T_1 increases. The satisfactory fittings with a mono-exponential decay function for all of the samples demonstrate that at each sucrose concentration, the TEMPOL occupies a single type of environment in the mesodomain.

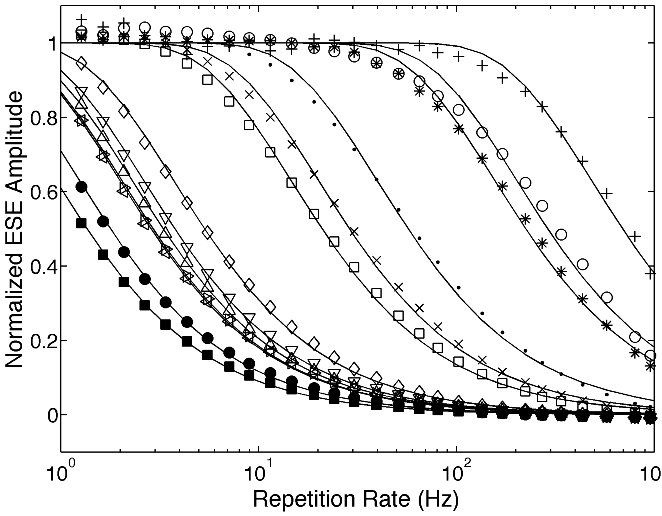

Figure 2.6. Pulse repetition rate dependence of the normalized ESE amplitude of TEMPOL in sucrose solutions with different sucrose percentages (%w/v) : (+) 0%, (○) 1%, (*) 3%, (•) 5%, (×) 10%, (□) 15%, (◊) 20%, (▽) 25%, (△) 30%, (▷) 40%, (◁) 50%, (n)60%, (●) 75%. The experimental data was fitted with exponential decay function, as described in the *Methods* section. The values of the time constant are included in Table 2.1.

The T_1 values as a function of sucrose concentration are shown in Figure 2.7. The T_1 values and fitting errors are included in Table 2.1. The values of T_1 increase, by adding more sucrose, indicating that local concentrations of TEMPOL decrease. Since the spin systems contain an identical amount of TEMPOL, 0.2 mM, this demonstrates that the volume of mesodomain expands with increasing added sucrose, resulting in a lower local concentration of TEMPOL. The trend of the increment of T_1 with respect to increasing sucrose concentrations is nonlinear, and divided into three stages, distinguished as 1-15%, 20-50%, and >50% (w/v).

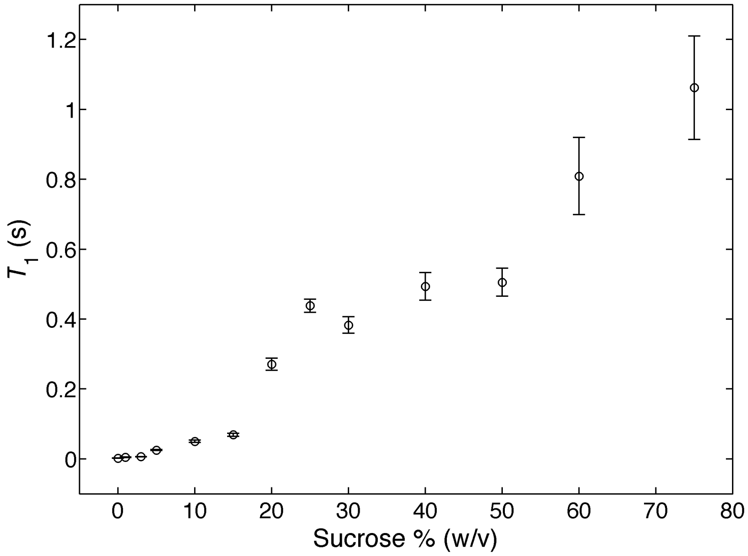

Figure 2.7. Spin-lattice relaxation time, T_1 of sucrose solutions with different sucrose percentages (w/v). It is noticeable that the sucrose samples are segregated into three regions: 0% ~ 20%, 20% ~ 50%, and greater than 50% (w/v).

2.2.4 Calibration of TEMPOL concentration with spin-lattice relaxation time in glassy 60% (w/v) sucrose solution

To further quantify the TEMPOL concentration in the mesodomain, a set of control samples were made and measured. As described above (**2.1.2**, sample preparation), these samples for calibration contain a homogeneous glass former, 60% (w/v) sucrose, and varied concentrations of TEMPOL, from 0.12 – 100 mM. The TEMPOL molecules are randomly distributed in these samples. Repetition rate dependence experiments were performed at 6 K for these samples, and T_1 values ranging from 1 – 300 s were obtained. Figure 2.8 presents the spin-lattice relaxation rate, $1/T_1$, as a function of TEMPOL spin probe concentration. Base 10 logarithmic scales are used for x and y-axes.

The results are overlaid with a curve, which presents the best fit, by the following cubic polynomial function: $T_1^{-1} = 1.327 \times 10^{-4} c^3 + 1.152 \times 10^{-2} c^2 + 0.236 c + 1.11$, where c is the TEMPOL concentration. This function provides a quantitative relationship between the concentrations of TEMPOL and T_1 values. By applying this expression to the measurements conducted on samples with varied sucrose concentrations, the effective concentration of TEMPOL in the mesodomain can be extracted. Detailed descriptions are included in **Section 2.3**.

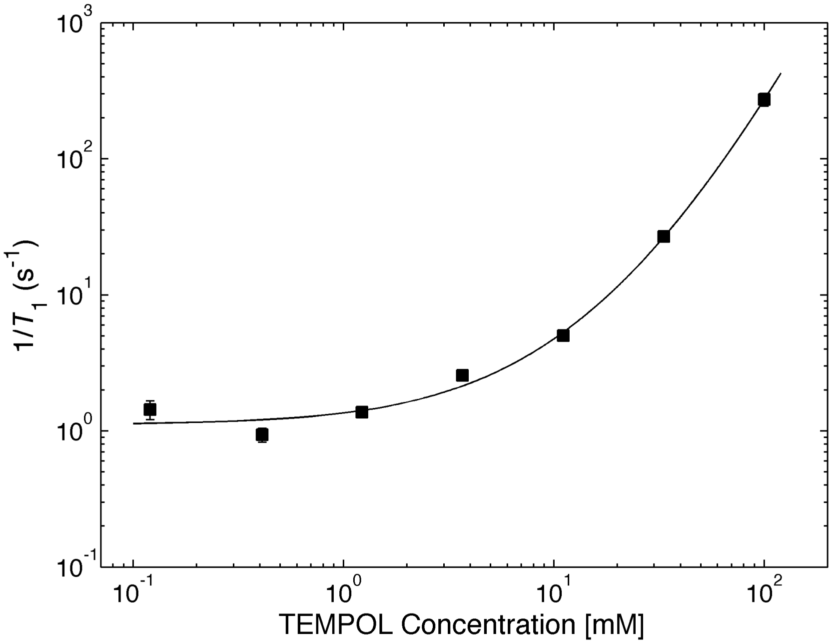

Figure 2.8. Dependence of the spin-lattice relaxation rate, 1/T₁, on TEMPOL spin probe concentration in homogeneous glass formed by using 60% (w/v) sucrose solution. The overlaid curve represents the best fit by the following cubic polynomial function: $T_1^{-1} = 1.327 \times 10^{-4} c^3 + 1.152 \times 10^{-2} c^2 + 0.236c + 1.11$, where c is the TEMPOL concentration.

2.2.5 Relative TEMPOL mesodomain concentration from phase memory relaxation time in aqueous sucrose solutions

Two-pulse ESEEM time traces were collected for the samples with different concentrations of sucrose, and fit with Eq.2, yielding the phase memory time constant, T_M. Because of the different relaxation mechanisms, for example, transverse relaxation does not require energy exchange with the environment; T_M is considerably shorter than T_1.[68] In the solid state at 6 K, the spin-spin relaxation time, T_M, for the TEMPOL and sucrose samples, is predominantly governed by the relaxation of the transverse components of the electron spin polarization, which is affected by the dipolar coupling among the electron spins.[69] Therefore, the T_M value depends on the distance between electron spins, and thus is a useful parameter to present the local concentration of TEMPOL. Selected 2-pulse ESEEM traces as a function of τ, at representative added sucrose concentrations are shown in Figure 2.9. The dashed lines represent the best fits from Eq.2. The values of T_M are listed in Table 2.1. Figure 2.10 shows the dependence of

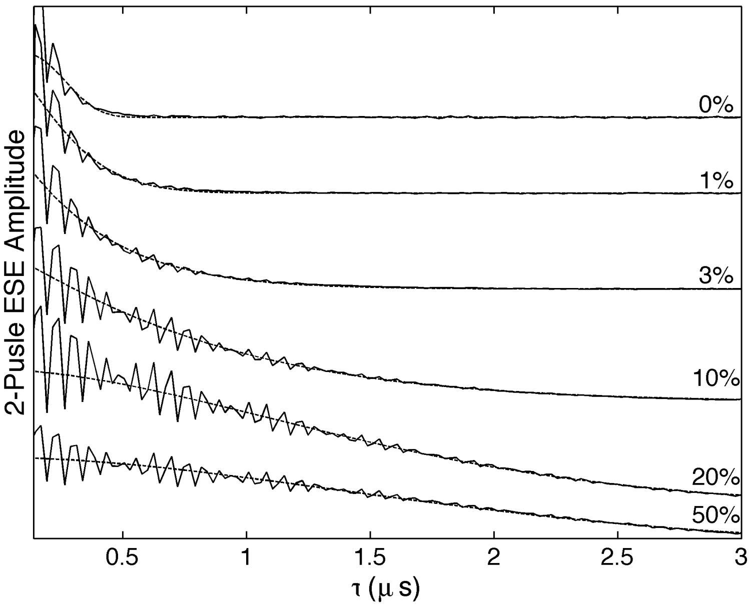

Figure 2.9. Two-pulse ESEEM waveforms at different sucrose content percentages (w/v), overlaid with baseline fitting of stretched exponential decay function.

T_M on sucrose concentration. The trend of increasing T_M resembles to that of spin-lattice relaxation time T_1: T_M increases as the sucrose concentration increases. The increments of T_M values indicate that with added sucrose, spins are further separated apart in the expanding volume of mesodomain. The variation of T_M also exhibits three dominant regimes as follows: 1-15, 20-50, and >50 % (w/v).

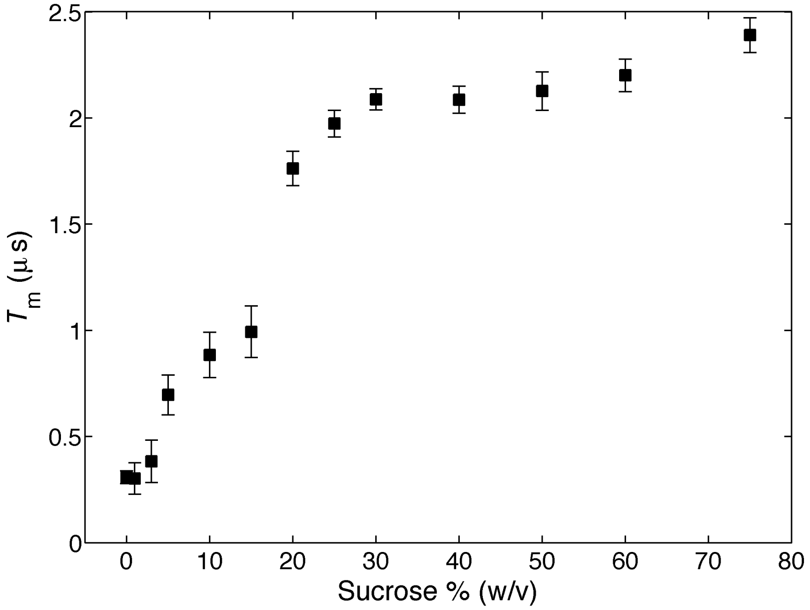

Figure 2.10. Phase-memory time, T_m, at different sucrose content percentages (w/v) obtained from fittings of stretched exponential decay function to two-pulse ESEEM waveforms.

2.3 Probing the various perspectives of the mesodomain

2.3.1 Identification of the mesodomain and properties in pure water and 1% (w/v) sucrose solution

In CW-EPR measurements, the T_t value for pure water is 205 K, which is signficantly lower than the melting temperature, T_m=273 K, but significantly higher than the T_g value of 136-138 K for homogenous water glass.[81, 82] This difference proves the formation of mesodomain in which TEMPOL is present. Figure 2.3 also shows that addition of 1% (w/v) sucrose raises the T_t up to 240 K, and for >1% (w/v) sucrose solutions, the T_t further shifts to 255 ±5 K. Similarly, in the three-pulse ESEEM measurements, as shown in Figure 2.5, the obtained EMD values classify the samples into three types: pure water (EMD = 0), 1% (w/v) sucrose solution and >1% (w/v) sucrose solutions. Compared to the constant EMD value for higher sucrose concentrations, the EMD for 1% (w/v) sucrose is approximately of its half amplitude. Both types of experiments show that the spin mobility and ^{2}H modulation in the TEMPOL with 1% (w/v) sucrose sample deviate from in other samples. This difference might be caused by a partial breakdown of the free probe assumption,[95] with addition of a small amount of sucrose.

2.3.2 Relative volume of the mesodomain in unsaturated sucrose-water solutions

It is shown in Figure 2.3 that the T_t value for >1% (w/v) sucrose solutions approximately approaches to a constant (255 ±5 K). At different temperatures, the broadening and narrowing of EPR line shapes are due to the averaging anisotropy of tumbling motions of the TEMPOL probe. Here, the rotational correlation time scale of the probe tumbling and temperature are connected by the Stoke's law, as follows:[90]

$$\tau_{c,S} = \frac{4\pi\eta a^3}{3k_B T} \qquad \text{Eq. 2.3}$$

where *h*, a and k_B represent solvent viscosity, the probe radius, and the Boltzmann constant, respectively. In Eq. 2.3, τ_c is directly proportional to η. Therefore, the nearly overlapping τ_c vs. T curves for the sucrose-water samples indicate that the viscosity of the mesodomain environment of TEMPOL is approximately equivalent at each temperature, for >1% (w/v) sucrose solutions. It has been shown that the viscosity of sucrose-water mixtures is determined by the sucrose concentration.[96, 97] The constant viscosity in the mesophase, therefore, presents a uniform local sucrose concentration, for >1% (w/v) sucrose samples. This is in agreement with the observation from EMD measurements: a constant EMD value, for >1% (w/v) [6,6'-$^{2}H_2^{fru}$]-sucrose solutions, which is also interpreted as a comparable freeze-quenched sucrose concentration in the mesodomain. The consistent results from two types of measurements at different temperatures demonstrate that the compositions and structural features of the samples at a relatively high *T* (200 -270 K, below melting temperature) are maintained at lower *T* (6 K, in this study, after quenching).

Overall, a fixed local sucrose concentration is derived from a series of experiments, and it is independent of starting sucrose concentrations above >1% (w/v). The value is reasonably assigned as a maximally freeze-concentrated concentration, which was first proposed by Franks et. al to characterize T_g', as denoted in Figure 2.1.[76] Detailed information on the concentration will be provided, below.

Table 2.1: Electron spin echo envelope modulation, spin-lattice relaxation and phase memory relaxation parameters for the TEMPOL spin probe in pure water and in aqueous sucrose solutions at different concentrations of added sucrose.

Sucrose Concentration [% (w/v)]	EMD	T_1 (s)	2-Pulse ESEEM	
			T_M (μs)	Exponent
0	N/A	(2.1±0.4)×10^{-3}	0.31±0.03	3.2±1.1
1	0.013±0.007	(5.0±0.9)×10^{-3}	0.30±0.07	1.5±0.4
3	0.027±0.002	(6.4±0.6)×10^{-3}	0.38±0.10	1.1±0.3
5	0.038±0.005	(25±2)×10^{-3}	0.70±0.09	1.2±0.2
10	0.029±0.004	(50±3)×10^{-3}	0.88±0.11	1.1±0.2
15	0.037±0.002	(69±5)×10^{-3}	0.99±0.12	1.2±0.1
20	0.041±0.004	0.27±0.02	1.76±0.08	1.7±0.2
25	0.042±0.006	0.44±0.02	1.97±0.06	1.8±0.2
30	0.037±0.006	0.38±0.02	2.09±0.05	2.0±0.1
40	0.030±0.006	0.49±0.04	2.08±0.06	1.9±0.2
50	0.034±0.006	0.51±0.04	2.13±0.09	1.9±0.2
60	0.031±0.006	0.81±0.11	2.20±0.08	2.6±0.2
75	0.030±0.006	1.06±0.15	2.39±0.08	2.6±0.2

2.3.3 Spin probe concentration in the mesodomain

Figure 2.7 or Table 2.1 exhibits the general trend in T_1 values at 6 K, which indicates a growing volume of the mesodomain with increasing added sucrose concentration, to achieve a constant maximal freeze-concentrated sucrose composition. Figure 2.8 presents a T_1 – TEMPOL calibration curve, which provides estimation of the effective concentration of TEMPOL in the mesodomain. The calculated TEMPOL mesodomain concentration is shown in Figure 2.11, as a function of added sucrose concentration. The dashed line is the predicted TEMPOL concentration,[76] based on the assumption of 80 ±5% (w/w) [120 ±8% (w/v)] sucrose in the mesodomain.[80] The 60 and 75% (w/v) super-saturated sucrose (known as homogeneous glass formers) samples fall on the line, to within the standard deviation of the measurements. However, the effective TEMPOL concentrations of the unsaturated solution samples are 5- to 10-fold higher than the prediction. In addition, the TEMPOL concentration variation is not continuous, which undergoes transitions at 15-20% and 50-60% (w/v) added sucrose. The dependence of T_M values on added sucrose concentrations in Figure 2.10 is also separated into three stages, and punctuated at two transition concentrations. Both the T_1 and T_M measurements provide direct evidence that the mesodomain is inhomogeneous.

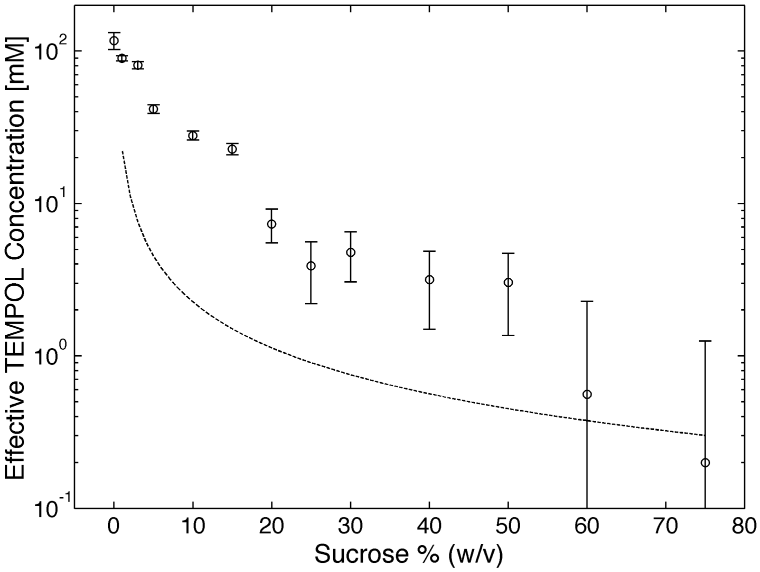

Figure 2.11. Effective TEMPOL concentrations of sucrose samples with different sucrose percentages. This effective concentration is calculated using TEMPOL concentration calibration and T_1 measurement of sucrose samples. The dashed line is the predicted TEMPOL concentration with the assumption that all sucrose forms 80% (w/w) maximally-freeze concentrated amorphous glass.

2.3.4 Heterogeneous structure of the mesodomains formed from unsaturated sucrose-water solutions

To explain the distinct deviation of the calibrated TEMPOL concentration values from which predicted for maximally freeze-concentrated 80% (w/w) sucrose, with relative to T_g' in Figure 2.1, the formation of crystalline sucrose hydrate structures in the mesodomain is proposed. The ordered sucrose hydrates exclude TEMPOL further into the amorphous sucrose-water mixture in the mesodomain. The proportion of the volume of sucrose hydrates (ordered) and amorphous sucrose-water (disordered) at each sucrose concentration is estimated and shown in Figure 2.12. The values are obtained by comparing the calibrated and predicted TEMPOL concentrations shown in Figure 2.11.

The proposed model of mesodomain heterogeneity in this work is supported by other non-mesodomain related measurements on sucrose hydrates in sucrose-water solutions in the literature, as follows: (a) Upon extended incubation of sucrose samples at a temperature among T_m and T_g of water, two crystalline sucrose hydrates: sucrose hemipentahydrate ($C_{12}H_{22}O_{11}\cdot2.5\ H_2O$) and sucrose hemiheptahydrate ($C_{12}H_{22}O_{11}\cdot3.5\ H_2O$), were discovered and investigated.[75] (b) The presence of different types of sucrose hydrates groups the DSC results into sub-regions on the temperature-composition state diagram.[98] (c) Different techniques, such as Raman[99] and fourier transform infrared (FTIR)[100] spectroscopies and X-ray[101] scattering were applied to explore the possible contributions of hydrogen bonding interactions in sucrose-solvent and sucrose-sucrose to the composition and phase segregation in the diagram for fluid aqueous sucrose solutions. The existence of an ordered sucrose portion was also detected in the mesophase.[101]

As shown in Figure 2.12, the ratio of sucrose hydrate and amorphous sucrose-water volume presents discontinuous growth of sucrose hydrates, which segregates into three regimes, as follows: (a) Below 20% (w/v) of starting sucrose concentration, the increasing sucrose concentrations is favorable to the formation of sucrose hydrates. (b) At 20≤ % (w/v) ≤50 of intermediate starting sucrose concentrations, the production of sucrose hydrates achieves to a steady state across this range, and the ratio value indicates approximately 80% of the sucrose forms hydrate structure. (c) For 50% (w/v) of initial sucrose concentration, the ratio is 0, indicating that all sucrose forms a disordered aqueous glass, and is homogeneously distributed over the sample volume. As the starting concentration of sucrose increases up to 50% (w/v), the generation of sucrose hydrate stepped decreases in the three regions, which probably results from an increasing effective viscosity of the mesodomain, that reduces hydrate nucleation and migration. Interestingly and coincidently, discontinuities also occur for 47% (w/v) sucrose solution in the following physical properties, such as viscosity,[102] sucrose C-O-C bending frequency probed by Raman spectroscopy,[99] and water mobility probed by ^{1}H and ^{17}O nuclear magnetic resonance (NMR) spectroscopy.[103, 104] In addition, about 50% (w/w) sucrose, the diffusion of water is isolated from that of sucrose.[105] Based on these discussions, the transition in Figure 2.12 at 50-60% (w/v) added sucrose therefore probably corresponds to the transition from heterogeneous frozen solution to the homogeneous glass. The origin of the transition at 15-20% (w/v) sucrose remains unclear.

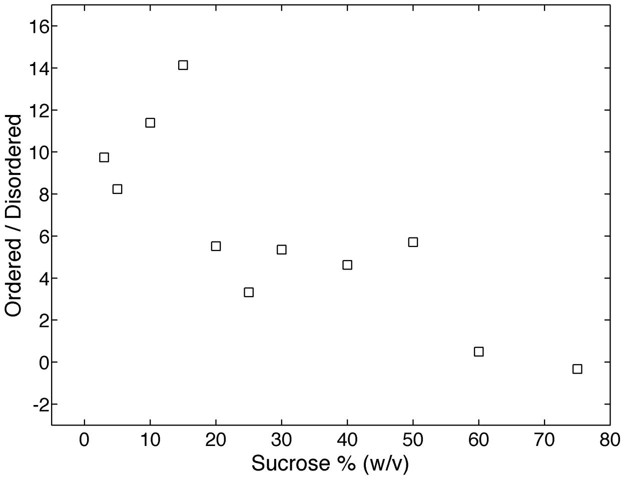

Figure 2.12. Dependence of the volume fraction of the TEMPOL-accessible region of the freeze-concentrated sucrose-water mesodomain on the concentration of added sucrose. Vertical axis is showing the volume ratio of ordered sucrose (TEMPOL inaccessible) to disordered sucrose (TEMPOL accessible).

2.4 Conclusions

In this chapter, we scrutinized the features of mesodomain in TEMPOL-sucrose-water systems with starting sucrose concentration ranging from 0-75 % (w/v), which spans pure water, unsaturated and supersaturated sucrose solution conditions. Upon freezing unsaturated sucrose solutions at a relatively slow rate, in our case, sucrose-water molecules, excluded by water-ice crystalline, reside in a heterogeneous domain (mesodomain). CW- and pulsed-EPR were applied to detect the dynamics of TEMPOL (tumbling, relaxation and etc.), the mesodomain-localized spin paramagnetic probe, to characterize the microscopic structure of mesodomain (volume, compositions, and environment and etc.), over the range of added sucrose concentrations. The experimental results are consistent. Mainly, we found that the measured mesodomain volume is less than the predicted maximally freeze-concentrated volume, derived from the higher TEMPOL concentration in the calibrated than the predicted. The volume-composition dependence exhibits transitions at two starting concentrations, 15-20% and 50% (w/v) sucrose, implying the heterogeneity of the mesodomain. Then, we proposed that a heterogeneous mesodomain consists of ordered sucrose hydrates and disordered amorphous sucrose-water glass phases. For the first time, the detailed mesodomain structure is probed with such a high resolution, and the dependence of the formation of sucrose hydrates on the pre-freezing sucrose concentration is discovered. The fundamental understanding of microscopic structure and order/disorder transitions in the mesodomain plays a critical role to characterize solvent-protein interactions, and further to protein function. This will be discussed in detail in Chapter 3.

Chapter 3

Structure and Dynamic Properties of the Mesodomain Environment of the Protein, Ethanolamine Ammonia-Lyase (EAL), in Frozen Aqueous Sucrose solutions

3.1 Background and Introduction

Solvent plays a crucial role in protein dynamics.[106] The topic of how large-scale and internal protein motions are influenced by the dynamics of bulk solvents and the hydration shell has been intensively investigated.[54, 55] To gain more insight into the relationship between protein structure/dynamics and solvent structure/dynamics, protein solutions are usually cooled down to cryogenic temperatures. In frozen aqueous solutions, the role of solvent in protein dynamics becomes more straightforward. Protein and solvent fluctuations are drastically slowed down so that probing the behavior of water in time window from ns to s becomes feasible by using a variety of experimental techniques with high resolution, such as dielectric spectroscopy and NMR.[53, 107]

It has been reported that, upon cooling, protein structures and dynamics are affected by: (a) the formation of ice or glass in the bulk solvent, (b) the interactions between protein side chains and hydration-shell solvent and (c) side chain rotations.[108] In this chapter, the first factor is emphasized. Cryoprotectants, such as sucrose and glycerol, are usually added to solutions to disturb the ice formation and reduce the solution inhomogeneity. With the aid of sucrose, proteins, cells, and biological samples in food and medicine can be commercially preserved.[109, 110] Besides these applications, the sucrose modulation on the microscopic solvent structure in sucrose-water-protein mixtures is also significant in understanding protein functions. Chiang et al. proposed that a protein peptide clustering possibly exists in frozen vitrified bulk solutions from the observed inhomogeneous EPR line shape broadening below 70 K.[111] They further found that the heterogeneity of bulk solvent structure caused the inhomogeneous peptide dispersion determined by using DEER-ESR technique. They used the spin-label ESR technique, with the paramagnetic probes attached to specific sites on proteins. The influence of solvent on the local protein structures and the side chain dynamics is characterized. In this chapter, we will focus on clarifying the role of solvent surrounding proteins on a microscopic level. The ultimate goal to develop a comprehensive understanding of the structure and dynamical behavior of the solvent environment of the protein at low temperatures, in order to quantify the contributions of solvent-protein coupling to the mechanisms of radical reactions conducted within the EAL enzyme.

Recently, Chen et al. characterized the disordered solvent structure, described as mesodomain, in frozen sucrose-water solutions containing TEMPOL by applying multiple EPR techniques.[70] It was found that TEMPOL resides in the mesodomain.[70] This study provides a promising model for probing the structure of protein environments and for obtaining a deeper insight into the correlation between the hydration shell and protein motions at low temperatures. Here, we extend the approaches to determine the detailed solvent heterogeneity in the presence of EAL.

We employ a combination of CW- and pulsed EPR techniques to explore the mesodomain in the presence of EAL over different temperature ranges, for samples containing EAL with and without the substrate ethanolamine, mixed with TEMPOL, and sucrose with a concentration ranging from 0% to 60% w/v. The concentration of TEMPOL in all samples is a constant (0.2 mM, 0.0034% w/v). Experiments were carried out to acquire the solute concentration, volume, and microscopic structure of the mesodomain: (a) CW-EPR spectra of TEMPOL mobility over 190 – 270 K were shown to determine the dynamical transition. (b) Electron spin-echo envelope modulation (ESEEM) spectroscopy at 6 K was used to exhibit the hyperfine interaction of TEMPOL and ^{2}H-sucrose and further to detect the volume of the mesodomain. (c) Electron spin echo (ESE) determined spin-lattice relaxation time (T_1), indicative of effective TEMPOL concentration in the mesodomain, was used to calculate the fraction volume of the mesodomain. (d) The phase memory time (T_M) was used to detect the relative spin-spin separation in the mesodomain. These results provide evidence for glass-like properties of proteins and lead to a conclusion that upon slow cooling, solute and solvent segregate. Proteins, TEMPOL, substrate and sucrose reside in a disordered confinement in which the concentration of sucrose reaches to maximum (80% w/v) in the forms of sucrose hydrates and amorphous sucrose-water glass phase. Ethanolamine expands the interstitial space between proteins.

3.2 Sample preparation and experimental setups

Sample preparation. Sucrose (≥99.5%, Sigma-Aldrich, St. Louis, MO), deuterated sucrose ([6,6'-$^2H_2{}^{fru}$] sucrose (≥99.8%, Omicron Biochemicals, Inc., South Bend, IN) and TEMPOL (4-Hydroxy-TEMPO, Sigma-Aldrich, St. Louis, MO) were purchased from commercial resources and used without further purification. Water (Nanopure, Siemens) with resistivity of 18.2 MΩ was used as the solvent. Solutions of TEMPOL and EAL were prepared in (a) a potassium phosphate (KPi) buffer (pH 7.5, 10 mM), (b) a mixture of 10 mM KPi (pH 7.5) buffer and natural abundance sucrose, (c) a mixture of 10 mM KPi (pH 7.5) buffer and deuterated sucrose. The concentration of EAL was maintained as 10 mg/ml, which equals to 20 μM for a holoenzyme molecular mass of 500,000 g/mol,[4] and an active site concentration of 0.12 mM, based on a stoichiometric ratio of 6:1 for active site/holoenzyme.[112, 113] The concentrations of ^1H sucrose or ^2H sucrose vary from 0% to 60% w/v. The concentration of TEMPOL is 0.2 mM [0.0034% (w/v)]. Seven samples containing substrate ethanolamine, EAL, TEMPOL, (^1H or ^2H) sucrose, were also made in 10 mM KPi (pH 7.5). The concentrations of EAL and TEMPOL are the same as above, which are 10 mg/ml and 0.2 mM, respectively. The concentration of ethanolamine is a constant, 200 mM. The concentrations of (^1H or ^2H) sucrose are 0%, 5%, 30% and 60%.

Solutions of TEMPOL with varied concentrations (100 mM, 33.3 mM, 11.1 mM, 3.70 mM, 1.23 mM, 0.41 mM, and 0.12 mM) in a sucrose/water mixture (60% (w/v) have also been prepared and investigated as reference samples. Another control sample with 30% (w/v) [6,6'-$^2H_2^{fru}$] sucrose and 30% (w/v) natural abundance (^1H) sucrose [total, 60% (w/v) sucrose] (red square) was also made.

All of these samples were degassed through freeze-pump-thaw procedures for three times and were then loaded into 4 mm o.d. EPR tubes (Wilmad-LabGlass, Buena, NJ) which were vacuumed and backfilled with argon (Ultra high purity gases, NexAir). Samples were first placed in a 252 K freezer for 12 hours, and subsequently plunged into liquid nitrogen (LN_2) for storage.

CW-EPR spectroscopy. X-band CW-EPR measurements were performed on a Bruker Biospin ElexSys E500 EPR spectrometer. Cooling of samples was achieved with an Oxford Instruments cryostat with continuous N_2 flow and the temperature was monitored and stabilized by a Bruker ER4131VT temperature control unit. EPR spectra were collected at different temperatures arranging from 160 K to 270 K. Measurement parameters were as follows: 9.41 GHz of a microwave frequency, 1024 points, 3320 Gauss of central field, 280 Gauss for sweeping width, 30dB power (0.2mW), 2 Gauss modulations, 10.24 ms sample time, 2.56 ms time constant, 4-36 scans. The temperature interval was 5 K in the measured temperature range (160 K-270 K). In the temperature dependence study, a 5- minute waiting at each temperature allowed us to ensure that the samples are in thermal equilibrium.

To obtain quantitative information on the mobility of TEMPOL, simulations were conducted on the experimental CW-EPR spectra collected at subfreezing temperatures （160-270 K) using the toolbox EasySpin "chili" function under the assumption of random rotational tumbling of the spin probe. By varying the corresponding correlation time, τ_C and other parameters (g_{XY}, g_{XY}, g_Z, A_{XY} and A_Z) in some specific ranges: g_{XY}=2.009-2.010, g_Z=2.004-2.005; A_{XY}=6.4-7.5 Gauss, A_Z=36-39 Gauss, respectively, the experimental EPR lineshapes were reproduced. Over 160-270 K, satisfactory fits were achieved with a single component, which represents one rotating species of the spin probe.

Spin-lattice relaxation time measurement from dependence of ESE amplitude on pulse repetition rate. All electron spin echo (ESE) experiments were performed at 6 K on a home-built X-band pulsed EPR spectrometer to obtain the longitudinal or spin-lattice relaxation times (T_1). The two-pulse sequence used is a Hann echo sequence, which is P1—τ—P2—τ—echo, where the width of P_i is 20 ns.[88] The spin echo intensity was recorded as a function of pulse repetition rate. The echo amplitude decreases as frequency increases because when the pulse sequences repeat with a high frequency, less z magnetization component that was projected into the x-y plane returned. As in the previous studies,[70] the dependence of the echo amplitude on pulse repetition rate can be fit with Eq. 2.1, [68, 87] which was described in detail in Chapter 2, and the longitudinal, or spin-lattice, re

laxation time, T_1, can be determined. For convenience, the expression is repeated here:

$$V(t_{rep}) = V_0\left[1-\exp\left(-\frac{t_{rep}}{T_1}\right)\right] \qquad \text{Eq. 2.1}$$

where V is the ESE amplitude, t_{rep} is the repetition period (inverse repetition rate) and V_0 is the maximum ESE amplitude as $t_{\text{rep}}\rightarrow\infty$. Experiments were performed under the following conditions: a microwave frequency of 8.765 GHz, magnetic field of 3124 G and τ value of 504 ns. The pulse sequence repetition rate varied from 1 to 1000 Hz. Between the pulse sequences; dwell times were adjusted for the spin system to return to equilibrium.

Phase memory time measurement by using two-pulse ESEEM. The ESE is created at 6 K by a Hann echo sequence, P1—τ—P2—τ— echo (P1=P2),[88] where τ is the time between two pulses. Time-domain traces of the two-pulse ESEEM experiments for samples with different sucrose compositions were generated by integrating the area of the echo at varied τ with a stepped increment of 24 ns. These ESEEM data were collected with the following instrument settings: microwave frequency, 8.765 GHz; magnetic field, 3124 G; repetition rate, 5 Hz. The ESE decay can be fit with a stretched exponential function in Eq.2.2,[68 68, 87] which was described in detail in Chapter 2. For convenience, the expression is repeated here:

$$V(2\tau) = V(0)\exp\left[\left(-\frac{2\tau}{T_M}\right)^n\right] \qquad \text{Eq. 2.2}$$

where $V(2t)$ is the echo amplitude at a time, $2t$, after P_1, and $V(0)$ is the echo amplitude at t=0, to obtain the phase memory time, T_M, and exponent, n.

Three-pulse ESEEM. The echo generated by typical three-pulse sequence, P_1—τ—P_2—T—P_3 —τ— echo ($P_i=\frac{\pi}{2}$),[68] with fixed τ and varying T was recorded. The ESEEM spectra as a function of (τ+T) on samples containing deuterated sucrose were conducted at 6 K at microwave frequency 8.765 GHz, magnetic field 3124 G, τ=226 ns, a pulse sequence repetition rate 100 Hz and a stepped increment of 20 ns for T. The reason to set τ to be 226 ns is to significantly suppress proton modulations and effectively enhance weakly coupled ^{2}H modulation. OPTESIM,[71] a program developed by Sun. et al., that was based on Mims theory,[69] was used to simulate the collected spectra, under the assumption that a single ^{2}H was coupled to the electron to form a point dipole, which is randomly oriented with an adjustable hyperfine coupling parameter, r_{en}, which denotes the electron-nuclear separation. The simulations show that the isotropic part of the hyperfine coupling tensor, A_{iso} is 0. In the calculations, the nuclear quadruple coupling constant, $e^2qQ/\hbar$, and electron field gradient (efg) asymmetry parameter, η, were fixed to 0.2 MHz and 0.1, respectively, where e is the charge of an electron, q is the magnitude of the principal component of the efg tensor, Q is the nuclear quadruple moment, and $\hbar$ is the reduced Planck's constant.[89] The values of envelope modulation depth (EMD) were obtained from the fittings of the ESEEM waveforms to determine the interactions between ^{2}H in deuterated sucrose and TEMPOL.

3.3 Local environment mobility from CW-EPR spectra

Figure 3.1 presents CW-EPR spectra for TEMPOL in pure water and in 20% (w/v) sucrose solution at selected temperatures ranging from 180 to 260 K. Experimental CW-EPR spectra in Figure 3.1 in black are overlaid with simulations in dashed red lines, which are derived from the software Easyspin.[86]

Quantitative analyses of CW-EPR spectra provide the rotational correlation times (τ_C) of TEMPOL molecules in EAL/sucrose/10 mM KPi (with and without ethanolamine substrate) mixtures. The temperature dependence of the values of τ_C in the range 200-270 K is shown in Figure 3.2. The behavior of τ_C is similar to our previous study,[70] displaying discontinuities in three regimes: (a) At low temperatures, the large values of τ_C show evidence that TEMPOL molecules are in a rigid environment and immobilized. Because in the rigid limit, the orientations of the spin probes in the sample do not change with time, the randomly tumbling model of electrons is no longer appropriate, τ_C values obtained here are not accurate. Therefore, in this temperature regime, the averaged values, obtained from all of the different conditions at the particular temperature, are calculated and shown in the plot. (b) As the temperature increases, τ_c values undergo a sharp decrease from the slow to fast motion regime. T_t, defined as the temperature at the termination of the transition. (c) At temperatures higher than T_t, τ_c decreases more slowly as a function of temperature, and approaches a constant value, characteristic of the rapid tumbling limit. T_t values for all samples are lower than the melting temperature, $T_m = 273$ K in pure water, and significantly higher than the glass transition temperature, T_g for pure water, which was shown to be 124-136 K.[81, 114] This shows that TEMPOL molecules with EAL or EAL/substrates reside in mesodomains in pure water and in the sucrose/water mixtures, which is similar to the previous observations.[70] Figure 3.2 shows that T_t of TEMPOL and EAL in pure water is 235 K, and that, for added 1, 3, and 5% (w/v) sucrose, T_t successively increases to 240, 250, and 255 K, respectively. The T_t value is also constant, at 255 K, for >5% sucrose, T_t.

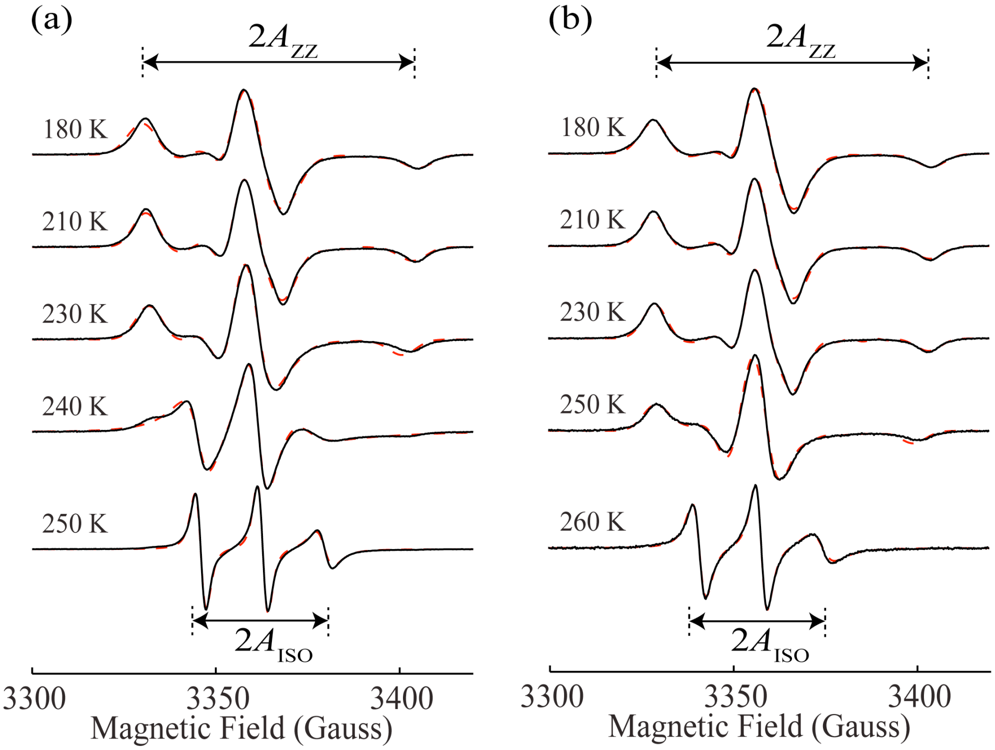

Figure 3.1. CW-EPR spectra overlaid with simulations (dashed, in red) of TEMPOL mixed with 10 mg/ml of EAL with and without sucrose. (a) 0% sucrose. (b) 20% sucrose. The concentration of TEMPOL is 0.2 mM.

The values of T_t for TEMPOL in EAL/ethanolamine/sucrose mixtures are also shown in Figure 3.2 in open symbols. T_t of TEMPOL and EAL/ethanolamine in pure water is 235 K, for added 5% (w/v) sucrose, T_t shifts to 245 K, and for added 30 and 60% (w/v) sucrose, T_t maintains a constant, 255 K.

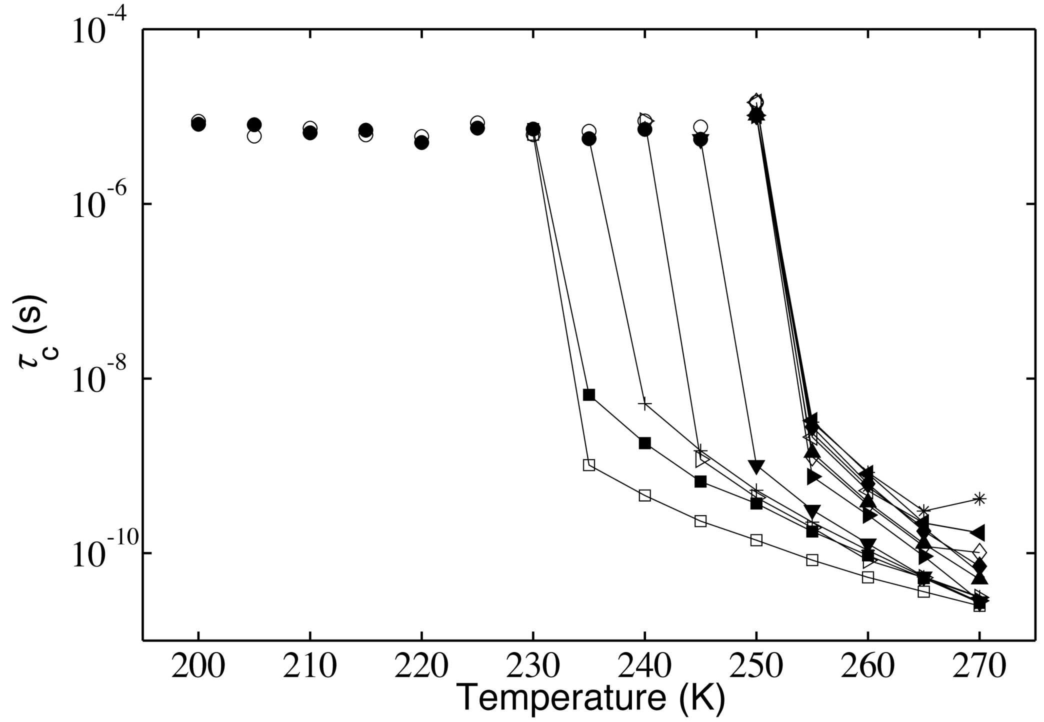

Figure 3.2. The rotational correlation time of TEMPOL, mixed with EAL, in pure water and in aqueous sucrose solutions (shown in filled symbols), and in substrate solutions with varied sucrose concentrations (%, w/v) (shown in open symbols). The temperature range is from 200 K to 270 K. The average value of τ_c from the rigid limit simulations is shown in circles. Filled symbols: (■) 0%, (+) 1%, (▼) 3%, (▶) 5%, (▲) 10%, (x) 20%, (♦) 30%, (*) 45%, (◀) 60% (w/v) sucrose. Open symbols: (□) 0%, (▷) 5%, (♢) 30%, (◁) 60% (w/v) sucrose.

3.4 Local sucrose concentration revealed by the envelope modulation depth (EMD) analysis from Electron Spin-Echo Envelope Modulation (ESEEM) spectroscopy

Three-pulsed ESEEM was applied to samples containing deuterated sucrose to detect the weak hyperfine coupling between ^{2}H (I = 1) and the unpaired electron on TEMPOL. Figure 3.3 shows representative time-domain ESEEM waveforms. The spectra are modulated

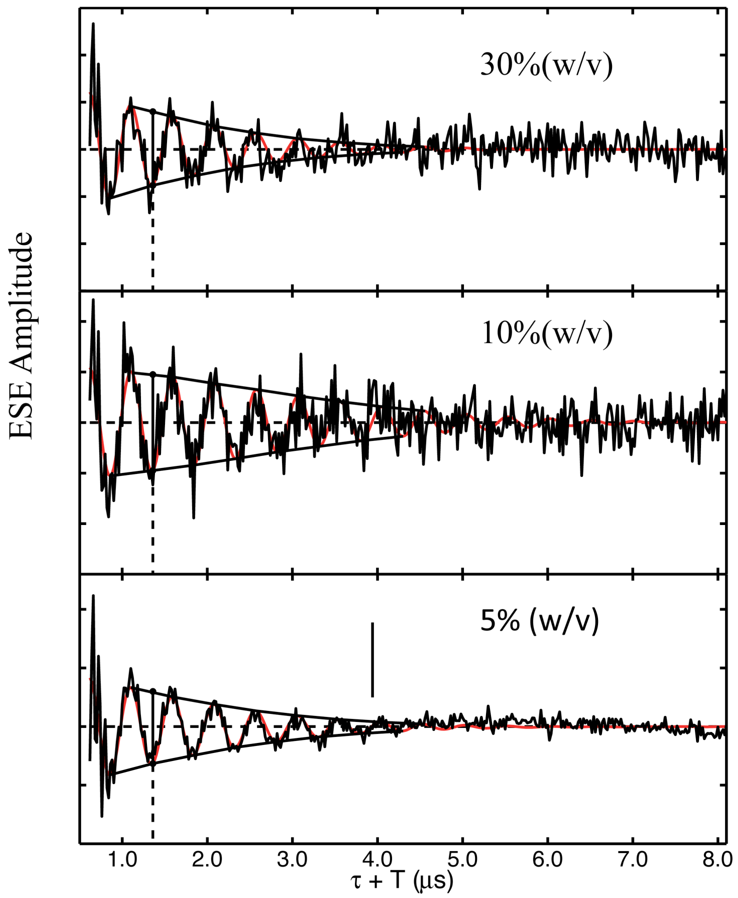

Figure 3.3. Three-pulse ESEEM waveforms (black) and overlaid ESEEM simulations (red) in EAL and ^{2}H-sucrose solutions. (top) 30% (w/v) sucrose. (middle) 10% (w/v) sucrose. (bottom) 5% (w/v) ^{2}H-sucrose.

with a period of 480 ns, corresponding to a frequency of 2.1 MHz, which is the Larmor frequency of "free" precession of ^{2}H at the experimental magnetic field of 3124 Gauss. By using the OPTESIM simulation software,[71] the spectra were simulated and the results show that the $A_{\text{iso}} = 0$ for the ^{2}H coupling, indicating that the ^{2}H are not directly bonded to TEMPOL. The weak dipolar interactions with the electron from the ^{2}H nuclei on sucrose are proportional to the number and the separation distance. The envelope modulation depth (EMD) is calculated, to estimate the intensity of the coupling and further to report the local sucrose concentration, with a formula of (*a*-*b*)/*b*, where *a* denotes the ESE amplitudes at the interpolation of the first and second peaks and *b* denotes amplitude at the second trough in the 3-pulse ^{2}H-ESEEM waveform. The positions of troughs and peaks are exhibited in simulated waveforms with black dots in Figure 3.3.

Figure 3.4 shows the EMD as a function of 6,6'-$^2H_2^{fru}$ sucrose concentration, over a range of 1-60% (w/v) added sucrose. The EMD values are listed in Table 3.1. The results for samples in the absence of substrate ethanolamine show that, with the exception of 3% (w/v) sucrose, at added sucrose concentrations ≥ 5% (w/v), the EMD values remain constant within one standard deviation. This indicaes that a constant local sucrose concentration surrounds TEMPOL, for ≥5% (w/v). The EMD for 60% (w/v) sucrose is not shown in this plot because with a repetition rate as high as 100 Hz, echo in this sample is not detectable. For samples with ethanolamine, except for added 5% (w/v) sucrose, the EMD values retain the same as samples without substrate. For comparison, data acquired in our previous work are presented here in solid spheres[70] At low sucrose concentration 5% (w/v), EMD for the sucrose solution sample is larger than EMD for the sucrose + protein sample, which is larger than EMD for sucrose + protein + substrate sample. This observation suggests that there is additive mesodomain formation by proteins and substrates, leading to a lower concentration of sucrose interacting with TEMPOL.

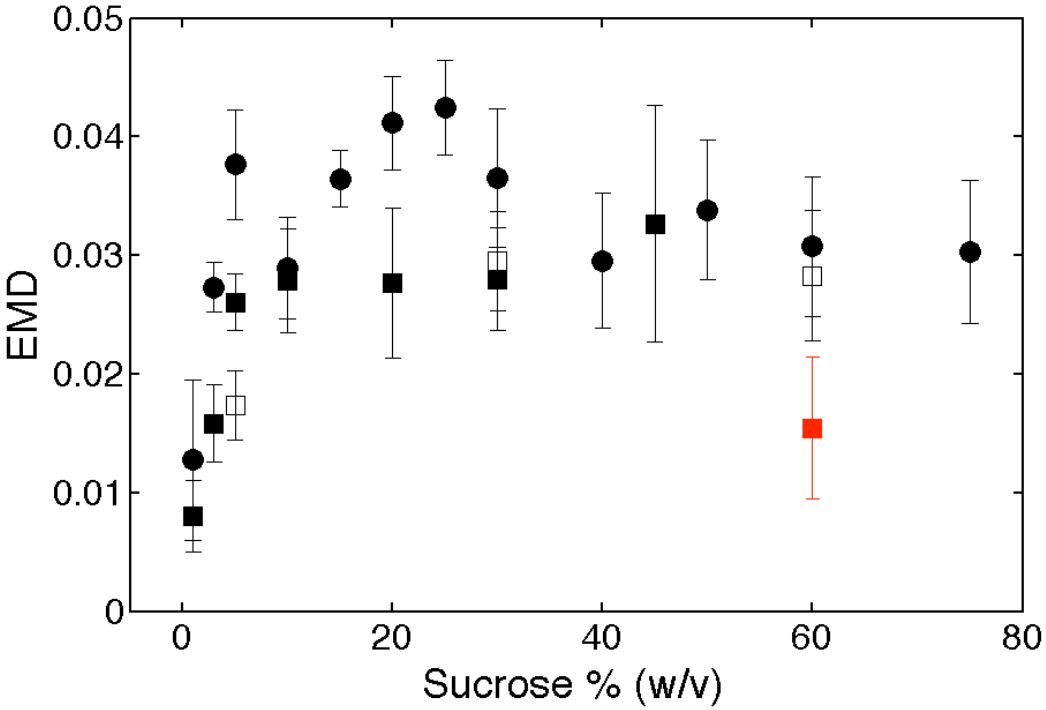

Figure 3.4. The envelope modulation depth (EMD) as a function of ^{2}H-sucrose concentrations in pure water and aqueous ^{2}H-sucrose solutions (•), in EAL and ^{2}H-sucrose solutions (■) and in EAL, substrate and ^{2}H-sucrose solutions (□). Control sample with 30 % (w/v) [6,6'-$^2H_2^{fru}$] sucrose and 30 % (w/v) regular sucrose (red).

3.5 Longitudinal relaxation times (T_1) obtained from repetition dependence of ESE measurements to reveal the relative TEMPOL concentration.

The relationship between the longitudinal, or spin-lattice, relaxation time (T_1) and the spin probe concentration is shown by the Redfield theory and the derived analytical expressions, which correlate the spin-spin interactions to the electron-electron dipolar coupling, which is distance-dependent.[92-94] With increasing spin probe concentrations, the electron polarization decreases, resulting in a shorter relaxation time, T_1. Therefore, T_1 is a reporter of the local concentration of the spin probe, TEMPOL in our samples. For samples with relatively long relaxation times, as in our case, repetition dependence of the ESE provides a way to estimate T_1.

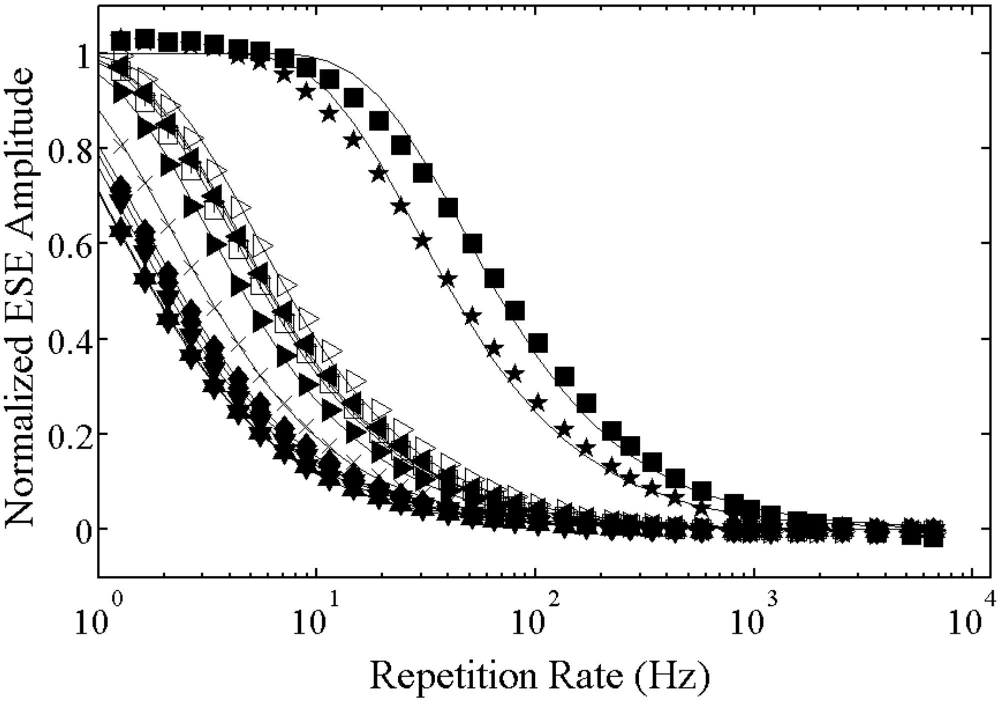

Figure 3.5. Pulse repetition rate dependence of the normalized two-pulse ESE amplitude of TEMPOL in EAL and sucrose solutions (filled symbols) and in EAL, sucrose and 200 mM of substrate solutions (open symbols) with different sucrose concentrations, [% (w/v)]: (■) 0%, (★) 1%, (+) 3%, (▶) 5%, (◀) 10%, (X) 20%, (♦) 30%, (▲) 45%, and (▼) 60% (w/v) sucrose.

Figure 3.5 presents the repetition rate dependence of ESE spectra for our samples, overlaid with fittings from Eq. 2.1. At high pulse repetition rates up to 1000 Hz, the spin system saturates, and the ESE amplitude is zero. For each sample, the fitting is good and a single value of T_1 is obtained. This means that at each sucrose concentration, the TEMPOL environment is homogeneous.

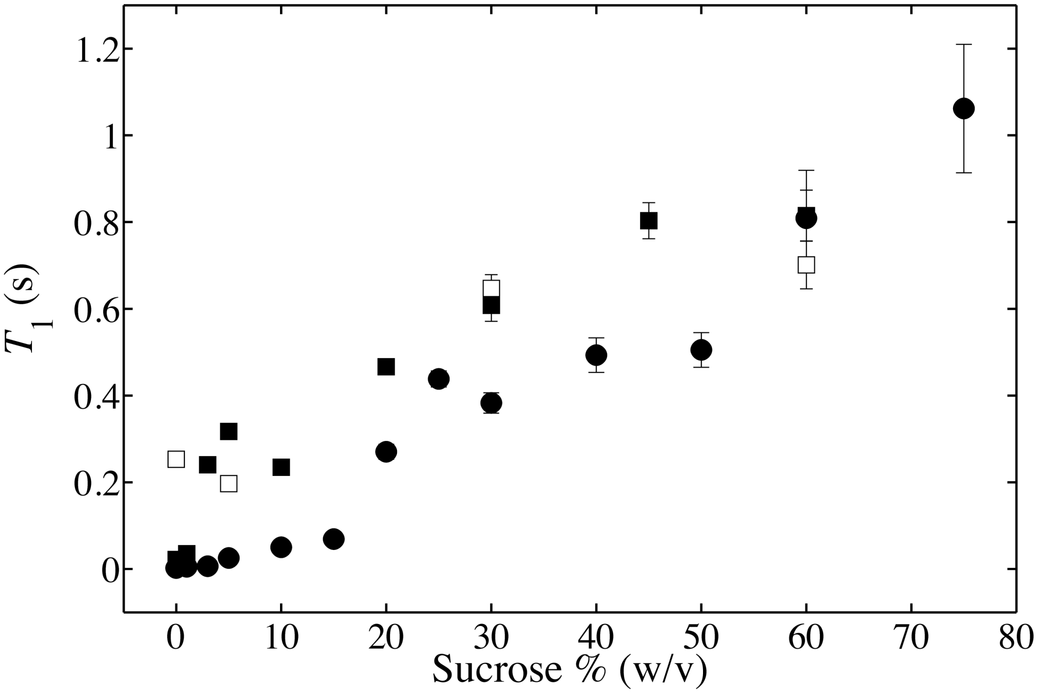

Figure 3.6. The dependence of the spin-lattice relaxation time, T_1, of TEMPOL in pure water and aqueous sucrose solutions (•), in EAL and sucrose solutions (■) and in EAL, substrate and sucrose solutions (□), as a function of sucrose concentrations.

Figure 3.6 presents the values of T_1 as a function of added sucrose concentrations over the range of 0-60% (w/v). The T_1 values with 95% confidence intervals are included in Table 3.1. Generally, as the sucrose concentration increases, T_1 increases (slower relaxation), corresponding to a decreasing concentration of TEMPOL in the mesodomain. The starting concentration of TEMPOL is constant for all samples; therefore, we can conclude that the addition of sucrose expands the volume of the mesodomain. As shown in Figure 3.6, the expansion is not linear to the added sucrose, and the trend is divided into the following regimes for the EAL and EAL/ethanolamine samples: fast increase (0-5% (w/v)), slow increase (5-45% (w/v)) and even (≥ 45% (w/v)). For comparison, T_1

values of TEMPOL in sucrose/water mixtures shown in solid symbols are also plotted.[70] For added sucrose <45% (w/v), T_1 is longer in EAL or EAL/ethanolamine solutions than in water at each sucrose concentration, indicating that proteins and substrate ethanolamine increase the volume of the mesodomain, and thus dilute the local concentration of the paramagnetic probe, TEMPOL.

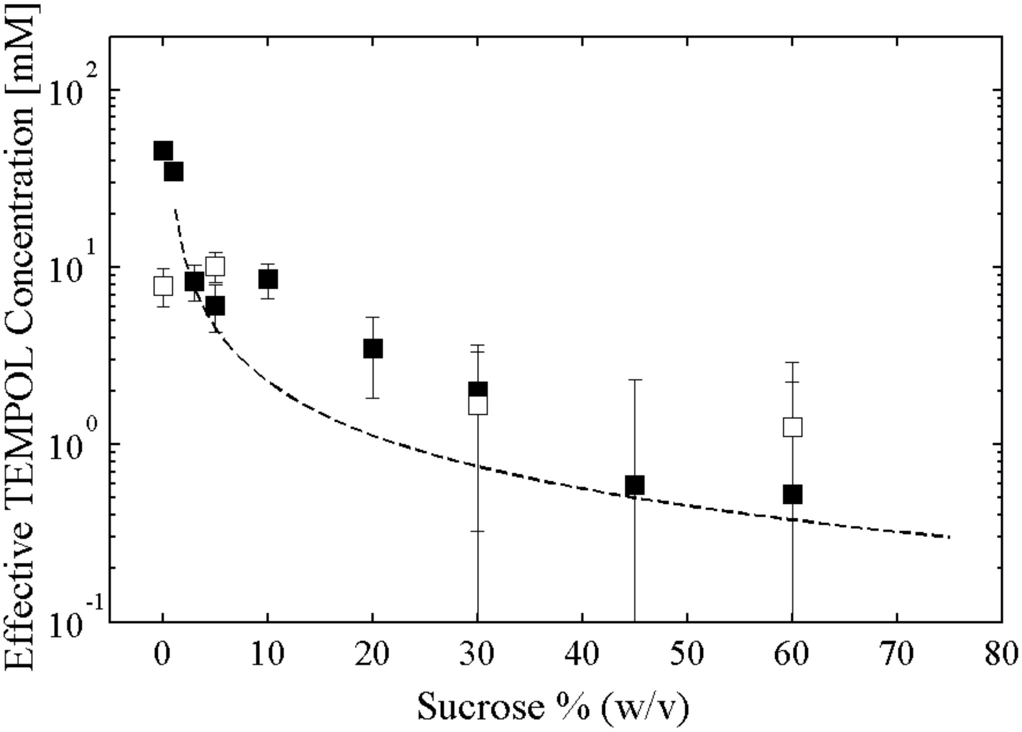

Figure 3.7. Dependence of the effective TEMPOL concentration on sucrose concentration in different aqueous EAL and sucrose solutions (filled square) and in EAL, substrate and sucrose solutions (open square). The dashed line is the predicted TEMPOL concentration under the assumption that all sucrose forms 80 ± 5% (w/w) [120 ± 8% (w/v)] sucrose maximally freeze-concentrated amorphous aqueous−sucrose glass.

To further determine TEMPOL concentrations in the mesodomain, a set of control samples with varied TEMPOL concentrations (described in Section 3.2) were prepared for calibration. The procedures were introduced in chapter 2 (see Section 2.2.4), here, we directly use the formula: $T_1^{-1} = 1.327 \times 10^{-4} c^3 + 1.152 \times 10^{-2} c^2 + 0.236 c + 1.11$, where c is the concentration of TEMPOL. By solving this equation with known T_1 values shown in Figure 3.6 and Table 3.1, the effective TEMPOL concentrations are obtained. Figure 3.7 shows the calculated TEMPOL concentrations as a function of added sucrose concentration over the range of 0-60% (w/v). All the effective TEMPOL concentration values are greater than 0.2 mM, the added concentration (concentration calculated on the basis of the total sample volume). The trend in the plot shows that with added sucrose, the effective concentration decreases, indicating the increasing volume of the mesodomain. As the sucrose reaches 45% (w/v) or higher concentration, the TEMPOL concentration shows no dependence on the addition of sucrose, suggesting a homogeneous glass formation in the samples. As discussed in Chapter 2, at extremely slow cooling rate, the maximally-freeze concentrated sucrose concentration, in the form of amorphous glass, is 80±5% (w/w) [120 ±8% (w/v)].[76] Assuming that the TEMPOL molecules reside in the mesodomain where sucrose concentration is 120% (w/v), the concentration of TEMPOL is predicted and shown in dashed line. The effective TEMPOL concentration in the middle range of sucrose contents is observed to be above the line. This is due to the formation ordered sucrose hydrates, which further shrink the volume of the mesodomain.

To explicitly reveal the deviation between the calibrated and the predicted TEMPOL concentration, the ratio is calculated and presented in Figure 3.8. The ratio also stands for the ordered sucrose hydrates/disordered sucrose phases. The fraction ranges from 0 to 3. The ratio value is higher in the intermediate sucrose concentration range (10-30% (w/v)) than in low and high sucrose contents (the ratio is approximately equal to

0). Compared to the ratio of sucrose hydrate and amorphous sucrose-water volume fractions presented in Figure 2.12, the ratio for samples containing EAL is relatively small. The general trend in the presence of EAL is similar to that in aqueous sucrose solutions at high sucrose concentrations.

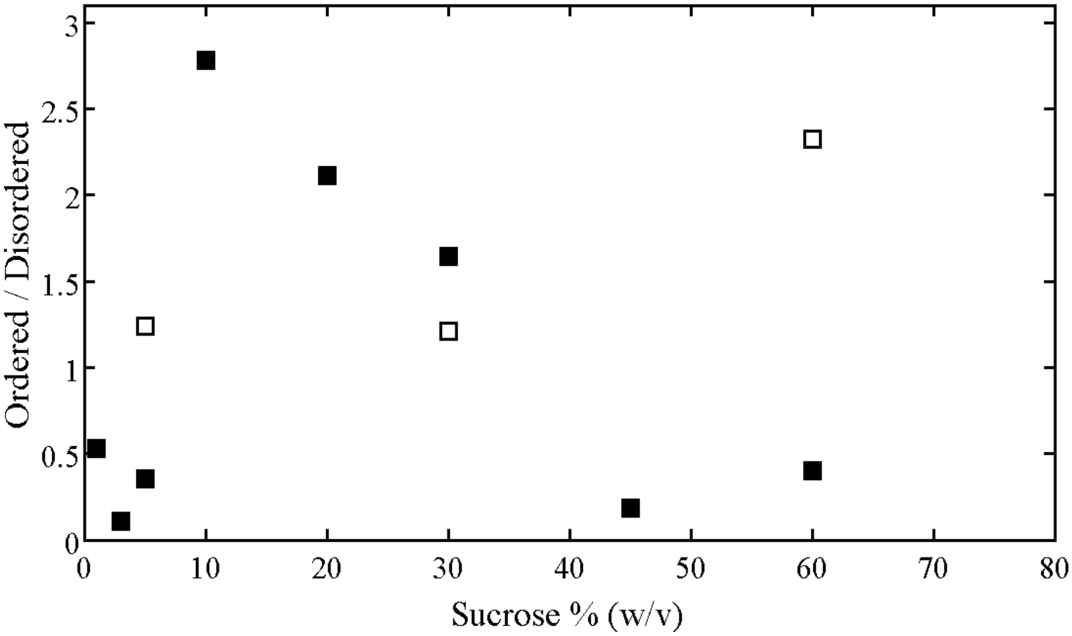

Figure 3.8. Dependence of the ratio of volume fractions of the ordered (sucrose hydrate) and disordered (amorphous aqueous−sucrose) phases of the heterogeneous mesodomain on sucrose concentration in different aqueous EAL and sucrose solutions (filled square) and in EAL, substrate and sucrose solutions (open square).

3.6 Phase memory times (T_M) obtained from 2-pulse ESEEM spectra analysis to reveal the relative TEMPOL concentration

At 6 K, two-pulse ESEEM spectra were collected for the samples. Figure 3.9 shows representative ESEEM waveforms as a function of τ for selected samples with different sucrose concentrations. The dashed lines are fittings derived from the stretched exponential function Eq. 2.2.

Figure 3.10 shows the dependence of T_M on the added sucrose concentration. The values are listed in Table 3.1. As sucrose concentration increases, T_M increases, indicating that the volume of the mesodomain increases. The general trend of the increase is separated into two regimes on added sucrose concentrations: 0-20% (w/v) and 30-60%(w/v). The same trend is observed for samples containing substrate ethanolamine.

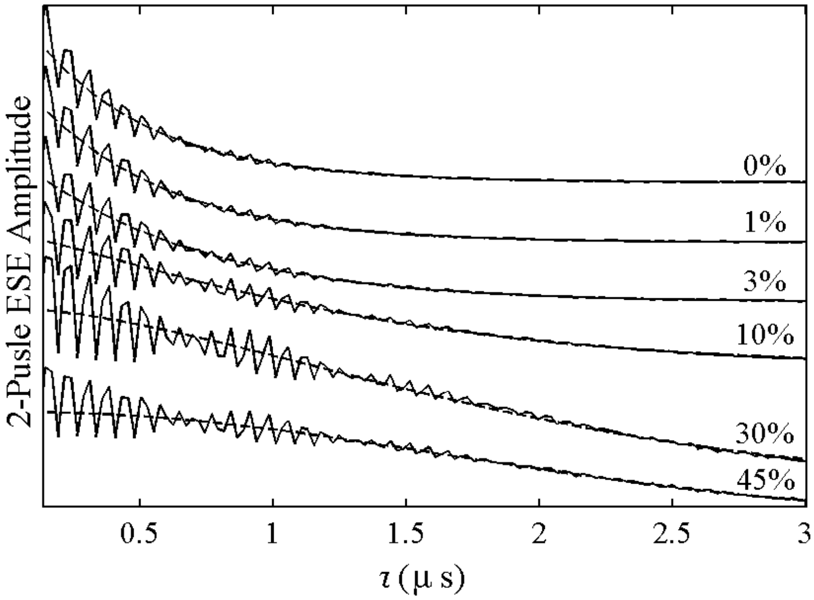

Figure 3.9. Two-pulse ESEEM waveforms for TEMPOL spin probe, mixed with EAL for pure water and different aqueous sucrose solutions [% (w/v)] and overlaid with fittings (dashed line) from stretched exponential decay function.

Table 3.1. Electron spin echo envelope modulation, spin-lattice relaxation and phase memory relaxation parameters and 95% confidence intervals for the TEMPOL spin probe in pure water and in aqueous sucrose solutions at different concentrations of added sucrose with addition of EAL and substates.

Sucrose Concentration [% (w/v)] + EAL	EMD	T_1 (s)	2-Pulse ESEEM	
			T_M (μs)	Exponent
0	N/A	$(2.2\pm0.2)\times10^{-2}$	0.44±0.09	1.00±0.17
1	0.008±0.003	$(3.5\pm0.3)\times10^{-2}$	0.50±0.09	1.03±0.17
3	0.016±0.003	$(2.4\pm0.1)\times10^{-1}$	0.68±0.10	1.05±0.16
5	0.026±0.002	$(3.2\pm0.1)\times10^{-1}$	1.08±0.11	1.13±0.17
10	0.028±0.004	$(2.3\pm0.1)\times10^{-1}$	1.35±0.09	1.30±0.18
20	0.028±0.006	$(4.7\pm0.2)\times10^{-1}$	1.89±0.06	1.73±0.16
30	0.028±0.004	$(6.1\pm0.4)\times10^{-1}$	2.15±0.06	2.09±0.20
45	0.030±0.010	$(8.0\pm0.4)\times10^{-1}$	2.20±0.10	1.85±0.23
60	N/A	$(8.1\pm0.6)\times10^{-1}$	2.24±0.11	1.78±0.22

Sucrose Concentration. [% (w/v)] + EAL + Substrate	EMD	T_1 (s)	2-Pulse ESEEM	
			T_M (μs)	Exponent
0	N/A	$(2.5\pm0.1)\times10^{-1}$	0.77±0.11	1.05±0.17
5	0.017±0.003	$(2.0\pm0.1)\times10^{-1}$	1.07±0.09	1.21±0.17
30	0.030±0.004	$(6.5\pm0.3)\times10^{-1}$	2.11±0.07	2.01±0.21
60	0.028±0.006	$(7.0\pm0.6)\times10^{-1}$	2.25±0.10	1.92±0.23

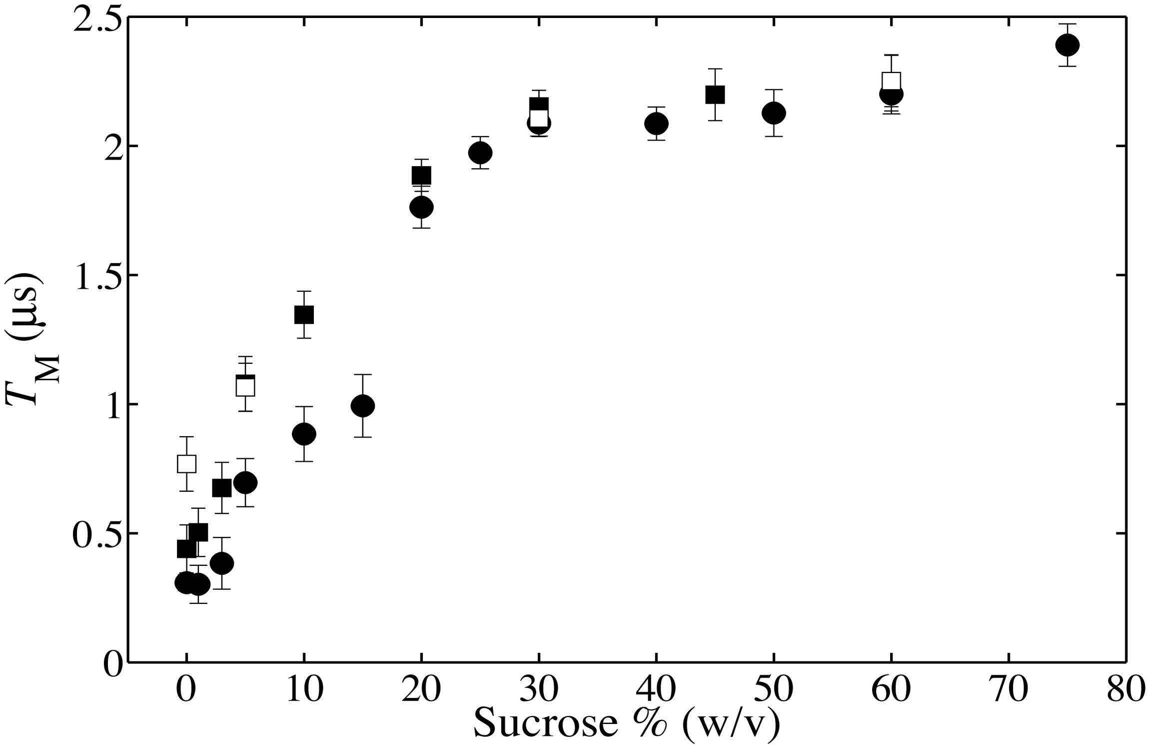

Figure 3.10. The dependence of the phase memory time, T_M, of TEMPOL in pure water and aqueous sucrose solutions (□), in EAL and sucrose solutions (n) and in EAL, substrate and sucrose solutions (□), as a function of sucrose concentrations.

3.7 Discussion

3.7.1 Identification of the mesodomain and properties in sucrose solutions with EAL or EAL/ethanolamine

In the CW-EPR measurements, T_t values for all samples are comparable to the two reported T_g values (124 and 136 K) for homogenous water glass, [81, 114] and the melting temperature, T_m=273 K. This provides evidence for the formation of mesodomains in the samples. TEMPOL, EAL and substrate ethanolamine are excluded from the crystalline ice. In Figure 3.2, the T_t values divide the EAL samples in sucrose solutions into two types: one with low T_t (EAL in pure water, 235 K), another is with high and constant T_t (EAL in ≥5% (w/v) sucrose solutions, 255 K). It was reported that T_t for pure water is 205 K, which is significantly lower than 235 K, the T_t for EAL in pure water. Addition of EAL causes a large, 30 K increase in T_t. This effect is comparable to 1% (w/v) sucrose added to pure water (35 K shift), indicating EAL behaves like sucrose by increasing the viscosity of the environment. Stoke's law, shown in Eq.2.3, correlates viscosity and τ_c. As viscosity decreases, τ_c shortens. It was also pointed out that viscosity of sucrose-water samples is proportional to the sucrose concentration.[96, 97] Therefore, the local concentration of sucrose can be estimated. In Figure 3.2, the viscosity for samples with EAL in ≥5% (w/v) sucrose solutions is similar. This observation is consistent with results shown in the ^{2}H modulation measurements. In Figure 3.4, the EMD, a reporter of local sucrose concentration, for EAL in ≥5% (w/v) sucrose solutions is approximately the same.

In Figure 3.2, addition of substrate ethanolamine in EAL solutions causes no shift in T_t, compared to 235 K, the T_t for EAL in pure water, and the t_c values for both samples are comparable, indicating that ethanolamine causes negligible change in EAL physical properties, such as viscosity and conformations.

3.7.2 Relative volume of the mesodomain in sucrose solutions with EAL or EAL/ethanolamine

Relaxation times measurements show that the addition of EAL leads to a large increment in the T_1 and T_M values for low added sucrose samples, compared to TEMPOL in aqueous sucrose solutions. For samples with high sucrose contents, homogeneous glasses are formed; therefore, T_1 and T_M values show no difference with and without EAL. The increase of relaxation times corresponds to a decrease in the paramagnetic probe concentration, which is shown in Figure 3.7. The calibrated concentration is 5-100 fold higher than the starting concentration, 0.2 mM. This deviation provides a convenient and efficient way to estimate the volume of the mesodomain. In contrast to the mesodomain volumes created in aqueous sucrose solutions, the volume is much larger in the presence of EAL or EAL/ethanolamine. This variation indicates that EAL generates mesodomain by itself, and protein surfaces create the boundaries. This interstitial space between EAL molecules provides evidence that on slow cooling, proteins are not tightly aggregated. This domain might assist the rearrangements proteins to approach to a thermostatic state at cryogenic temperatures.[115]

3.7.3 Heterogeneous structures of the mesodomains formed in sucrose solutions with EAL or EAL/ethanolamine

In our previous work, the mesodomain consists of ordered sucrose hydrates and disordered amorphous sucrose-water, with a ratio up to 14. As shown in Figure 3.8, the maximum ratio decreases to 3, indicating the EAL or EAL/ethanolamine prohibits the formation of sucrose hydrates, therefore, the volume of mesodomain is not further reduced by the exclusion of sucrose hydrates.

The difference of T_t in pure water and in 60% (w/v) sucrose solutions (glass) is 50 K,[70] while in the presence of EAL, the variation narrows to approximately 20 K. This suggests that EAL increases the degree of amorphousness in the samples.

3.8 Conclusions

In this chapter, we revealed the features of mesodomain in TEMPOL-sucrose-EAL (with or without ethanolamine)-water systems. The sucrose concentration ranges from 0-60 % (w/v), which covers pure water, unsaturated and supersaturated sucrose solution conditions. Upon cooling the unsaturated sucrose solutions at a relatively slow rate, sucrose-water molecules and substrate ethanolamine, excluded by water-ice crystalline, reside in a heterogeneous domain (mesodomain). EAL behaves like sucrose. Its large size and solid glass-like nature create mesodomains in frozen pure aqueous and aqueous-sucrose solutions. The surfaces are the boundaries. This mesodomain displays structural (amorphous glass) and dynamical properties (mobility transition) that differ dramatically from the polycrystalline bulk aqueous solvent.

CW- and pulsed-EPR were applied to detect the tumbling and relaxation of TEMPOL, to calibrate the effective spin paramagnetic probe concentration from T_1 and EMD measurements and to characterize the microscopic structure of mesodomain (volume, compositions, and environment). We found that the measured mesodomain volume is comparable with the predicted maximally freeze-concentrated (80% (w/v)) volume with exceptions of samples with 10-30% (w/v) sucrose, where ordered sucrose hydrates start to grow. The presence of EAL potentially inhibits the formation of sucrose hydrates by 4 times. The non-linear dependence of T_1 and T_M on sucrose concentrations implies the heterogeneity of the mesodomain, with transitions at two starting concentrations, 5% and 30% (w/v) sucrose.

From the effective TEMPOL concentrations, the volume of the EAL mesodomain in the absence of sucrose and substrate is estimated to be 1.8 μl for the 0.4 ml total sample volume.

The EAL protein mesodomain is augmented by the substrate ethanolamine, at concentrations used in cryotrapping of samples, for kinetic studies. Therefore, the EAL+substrate sample properties are appropriate for interpretation of protein-solvent interaction effects on with low-temperature radical reaction kinetics.

These understandings of the microscopic structure in the mesodomain are significant for us to investigate the mechanism how enzyme works at low temperatures.

Chapter 4

Probing decay kinetics of Co(II) - [^{1}H]-substrate radical pair at temperatures below 190 K

4.1 Introduction

It was reported that like glass-forming substances, proteins undergo a “dynamical transition” in the temperature range of 180-200 K.[44, 116, 117] This transition is demonstrated by a reduction of chemical rates in enzyme-catalyzed reactions and a decrease of the displacements and frequencies of atomic fluctuations.[44, 46, 118] These properties of the “protein glass transition” are characterized in many experiments performed on myoglobin, ribonuclease A and membrane proteins using different spectroscopic techniques, such as Mössbauer spectroscopy, X-ray crystallography, neutron scattering and other methods.[116, 119-123] Recently, it has been proposed that the fluctuations responsible for the “protein glass transition” do not actually undergo a dynamical transition, but instead decrease in frequency and amplitude to a threshold level, below which they cannot be detected by the physical measurement.[84] Below a comparable threshold level of frequency and/or amplitude, the fluctuations also cannot facilitate the protein function.[84]

Protein biological functions are achieved through protein “dynamics,” meaning the fluctuations of the protein structure among different configurational, or conformational states, which are necessary to guide the particular function. At temperatures below the region of the observed protein dynamical transition, protein motions are greatly slowed down and the amplitudes of the motions are decreased, and therefore, it is expected that protein functions are inhibited, or that they may even cease.[124, 125] To ascertain the above statement and further gain information on how protein dynamics affect functions near the transition range, the EAL catalyzed substrate radical decay reaction are investigated in this work at ultra-low temperatures (173, 177, 183, 187 K). EAL was selected as our model for the following three reasons: (a) The Co(II)-substrate radical pair intermediates generated during EAL catalysis can be cryotrapped and stabilized.[38, 63] (b) The radical signals can be monitored by full-spectrum CW-EPR spectroscopy. (c) The decay of substrate radical signals is directly related to protein function. The continuous reduction of substrate radicals implies no denaturation in the involved EAL molecules. Previously, kinetic information was accumulated by using the substrate radical decay reaction in EAL, down to 190 K.[36] Zhu and Warncke monitored the decay of substrate radicals to products in frozen aqueous solution on timescales of $<10^5$ s by using X-band CW-EPR spectroscopy. They found that in the low temperature range, ($190 \leq T \leq 207$ K) the decay fits a biexponential curve with constant fast and slow phase amplitudes. The rate constants k_f and k_s for the fast and slow phases are calculated from the fittings. It was shown that the natural logarithms of k_f and k_s values for $190 \leq T \leq 207$ K as a function of inverse absolute temperature can be linearly fitted. Different slope and intercept parameters are yielded for k_f and k_s, indicating different pathways, or the same pathway but different rate limiting steps the for the fast and slow populations. In their studies, the observed linear dependence in the Arrhenius plot implies that the protein dynamic transition was not detected, at $T \geq 190$ K. To extend this study, four ultra-low temperatures are added, which are 187, 183, 177 and 173 K, respectively.

It is predicted that at the ultra-low temperatures below 190 K, the decay rate of the ethanolamine substrate radical pair will be decreased to a degree that is not predicted by the linear extrapolation of the Arrhenius plots (ln$k$ versus $1/T$) of the rate constants from $T \geq 190$ K. That is, the rate constant is predicted to begin to decrease with a super-Arrhenius behavior, at some temperature below 190 K. This prediction is based on the fundamental proposal that protein dynamics is the precondition for functions. In addition, the previous work showed that the difference between the k_f and k_s obtained from the biexponential fit increased with decreasing temperature.[36] Therefore, it is rational to predict that the differences between k_f and k_s at the four ultra-low temperatures will increase.

In this chapter, we report the results of the substrate radical decay measurements at the four temperatures of 173, 177, 183, and 187 K, and present three kinetic models to analyze the collected data, including single exponential, biexponential, and single power law decay functions, applied to both the fast and slow phases of decay. Unlike satisfactory fittings with a biexponential equation for the decays above 190 K, this method does not fully cover the ultra-low temperature data. Among the three models, single power law shows the best fitting. It implies that the EAL substrate radical decay reaction reaches the "dynamic transition region" in the range of 173-187 K, and that the protein conformations are distributed, thus creating a distribution of activation energy barriers.

4.2 Sample preparation and time-resolved EPR measurements

Sample preparation. EAL was purified from *E. coli* overexpressed with cloned genes encoding EAL from *S. typhimurium*,[4] following the procedure proposed by Faust and coworkers,[126] with the modification that enzyme-containing precipitate was dialyzed in 2 L of buffer T (100 mM HEPES (pH 7.5), 10 mM potassium chloride, 5 mM dithiothreitol, and 10% (v/v) glycerol).[127] The concentrated EAL was suspended in 10 mM potassium phosphate buffer (pH 7.5) and stored in -80 °C freezer. Enzyme activity assay was performed by using the coupled assay with alcohol dehydrogenase (ADH) and NADH by monitoring the spectrophotometric changes caused by NADH oxidation in the reaction.[128] The determined activity of the purified EAL with substrate ethanolamine was in the range of 18-25 μmol/min/mg. The coenzyme B_{12} (adenosylcobalamin, Sigma Chemical Co.) and ethanolamine (Aldrich Chemical Co.) were obtained from commercial sources and used without further purification. EAL (15 mg/ml), B_{12} (0.36 mM), and ethanolamine (200 mM) were mixed in 10 mM KP (pH 7.5) and loaded in 4 mm o.d. EPR tubes (Wilmad-Labglass). Samples were immediately plunged into liquid nitrogen chilled isopentane (T = 150 K), and stored in liquid nitrogen. The average preparation time of one sample was 15 s from mixing to liquid nitrogen freezing. By using this cooling procedure, the EPR detectable Co(II)-substrate radical pair, an intermediate state during the catalysis, was cryotrapped. [38, 63] All reactions were conducted on ice under dim red light to avoid photolysis of the AdoCbl. The active site concentration of EAL (180 μM) relative to the concentration of B_{12} (360 μM) was maintained at 1:2 in all the samples, and relative to these constituents, the concentration of ethanolamine is in excess at 200 mM. A sample containing 10 mM KPi (pH 7.5) was made for baseline corrections.

Time-resolved EPR measurements. Prepared samples were incubated in an ISIS temperature controller (Instrumart, South Burlington, VT). The setting temperatures range from -100 to 40 °C (173 to 313 K) with high accuracy (± 0.02 °C)). Four ultra low temperatures, 173, 177, 183 and 187 K were used in separate experiments. To obtain a standard deviation at each data point, for 183 K measurements, three samples and one control sample were prepared, and for 173, 177 and 187 K four samples and two control samples were measured. At every incubation temperature, samples were first left in the controller for an hour and subsequently taken out for spectra collections in a Bruker E500 ElexSys CW-EPR spectrometer. All samples were saved in liquid nitrogen when they were outside the IRIS controller and EPR cavity. The temperature of the equipped Bruker ER4123 SHQE cavity was fixed to 120 K for all measurements. This temperature was obtained by an Oxford Instruments cryostat with continuous N_2 flow through a stainless steel coiling tube in a liquid nitrogen reservoir and stabilized and tuned by a Bruker ER4131VT temperature control unit. At 120 K, the dynamics of EAL was sufficiently slowed down, and the decay of the trapped radical pair state was negligible, compared the short measurement time range. To maintain the samples at the same position for all measurements, a dimpled dewar (Wilmad-Labglass) was built in the cavity. Before collecting EPR spectra, one minute was waited to ensure that the temperature of samples achieved 120 K from 77 K. Other parameters were set as follows: 9.45 GHz, microwave frequency; 1024 points; 3200 Gauss, central field; 2000 Gauss, sweeping width; 10 dB, power (20.38 mW); 1 Gauss, modulation; 40.96 ms, conversion time; 10.24 ms, time constant; 4-9 scans were averaged. After the EPR spectra were acquired, samples were first plunged in liquid nitrogen, then loaded in the controller and incubated until the next EPR spectra collections. The incubation times spanned from hours to days, depending on the decay time of the radical. On each day of measurements, an EPR spectrum of the sample containing 10 mM KPi was recorded as the baseline for all spectra collected on the same day. This buffer sample baseline was subtracted from the amplitude of each EPR substrate radical spectrum. To improve the signal to noise ratio, nine scans were averaged for each spectrum. The amplitude of the EPR signal that was used in the analysis was the difference between the peak and trough amplitude, which corresponds to the max and min value in the spectrum around $g \approx 2.0$. The EPR amplitude as a function of the incubation time shows the time-resolved decay of Co(II) and substrate radical signals. The EPR amplitude at time zero was derived from the first collected EPR spectrum.

In addition to the samples described above, which were measured at short time intervals, one or two samples (control samples) were maintained for days (10-30 days) in the temperature controller, and then taken out for measurements. These samples were used to examine whether frequent pauses of the catalytic reactions affect the accuracy and reliability of this measuring method.

4.3 Results and discussion

Figure 4.1 shows the results of the ultra low temperature decay measurements. In Figure 4.1, the results are plotted in a linear-linear, amplitude versus decay time form. Qualitatively, the decays all show a relatively fast phase and a slower phase. This is also shown by the log(rate) versus log(time) plots in Figure 4.2, which are presented as part of an assessment of the exponential character of the decays (see below). In Figure 4.2, a characteristic inflection separates the different phases. The inflection is obvious for the 177, 183, and 187 K decays. For example, at 183 K, the point appears at approximately 5×10^5 s on the log(time) axis. Figures 4.1 and 4.2 show that the form of the substrate radical decay kinetics changes significantly over the relatively narrow temperature range of 173-187 K.

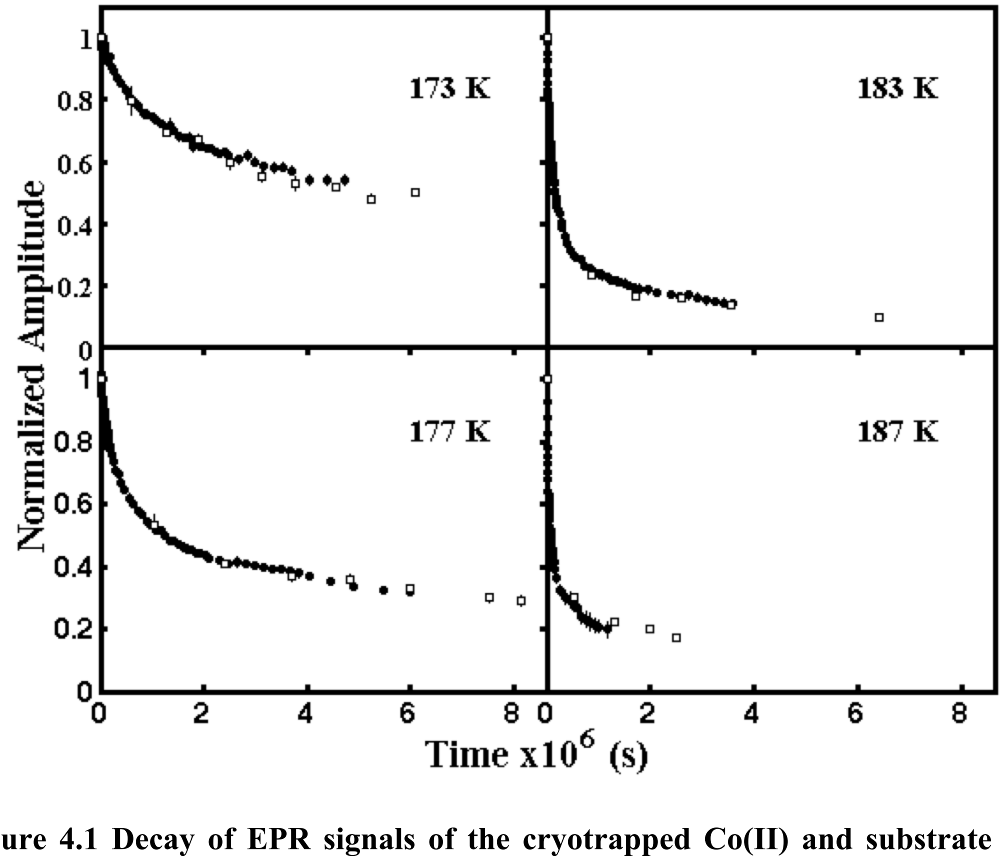

Figure 4.1 Decay of EPR signals of the cryotrapped Co(II) and substrate radical pair as a function of incubation times at different temperatures: 173, 177, 183 and 187 K. The amplitude (dot) was normalized to the value at $t = 0$. At each panel, the error bar presents the computed standard deviation of 3-4 samples at each time interval. In comparison with the samples measured at short intervals, the amplitudes of control samples (open square) with error bars were also shown at each temperature.

The decay data presented in Figure 4.1 and 4.2 was fitted by using fitting functions, in order to determine the kinetic models for the decay, toward comparison with the biexponential model, which was found to fit the data at $T \geq 190$ K,[36, 129] Figure 4.3 shows the experimental decay data, with overlaid best-fit monoexponential decay function, obtained by using the following expression:

$$A(t) = A_0 e^{-kt} \qquad \text{Eq. 4.1}$$

where A(t) is the normalized amplitude, and k is the first-order rate constant. This fitting function does not provide satisfactory results. This is consistent with previous results, which showed that the substrate radical is not singly populated (single-step kinetic model) at low temperatures down to 190 K.[36] Therefore, more parameters need to be introduced to analyze the components in the samples.

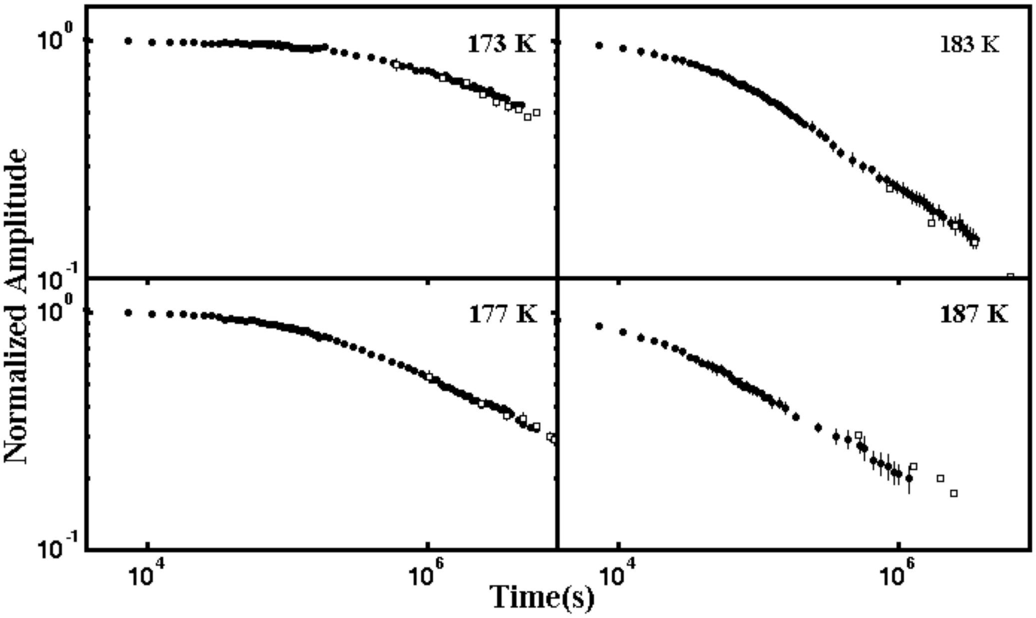

Figure 4.2 Decay of EPR signals of the cryotrapped Co(II) and substrate radical pair as a function of incubation times at different temperatures: 173, 177, 183 and 187 K on log-log scale. The symbols are as described in the legend to Figure 4.1.

Figure 4.4 shows the decays of the substrate radical fitted by a biexponential function, with the following expression:

$$A(t) = A_1 e^{-k_1 t} + A_2 e^{-k_2 t} \qquad \text{Eq. 4.2}$$

where A(t) is the normalized amplitude, A_1 and A_2 are the relative fractions of the rapidly and slowly decaying components satisfying the relationship of $A_1 + A_2 = 1$, and k_1 and k_2 are the corresponding first-order rate constants. The amplitude was normalized to

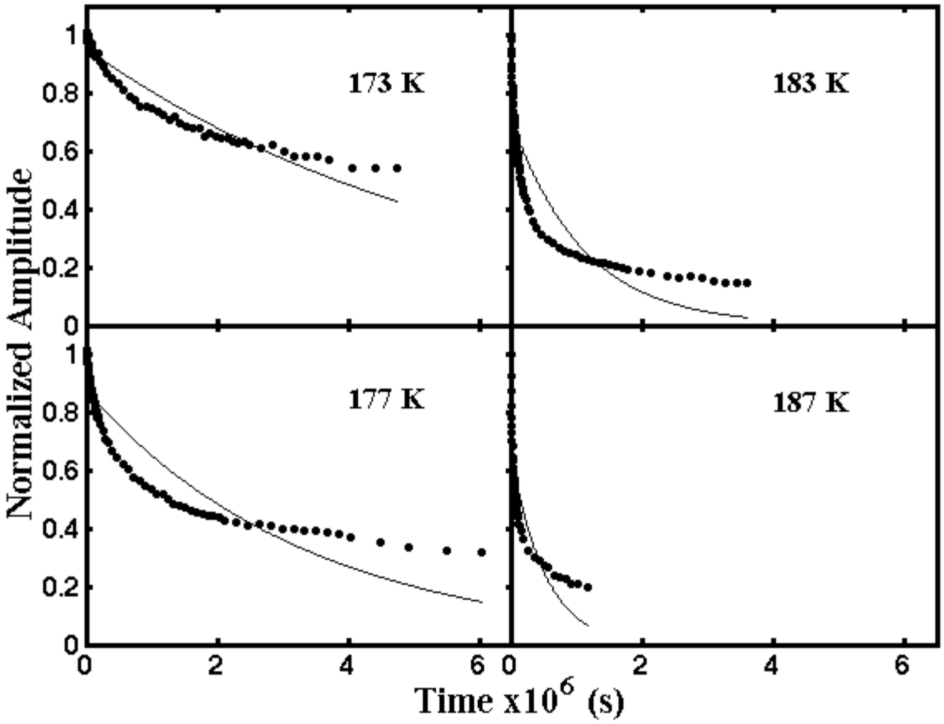

Figure 4.3 Dependence of EPR amplitudes of the cryotrapped Co(II) and substrate radical pair on incubation times at different temperatures: 173, 177, 183 and 187 K, and overlaid with best-fit monoexponential functions. The amplitude (solid) was normalized to the value at $t = 0$. *Simulation parameters*: 173 K: $A_0 = 0.96$, $k = 1.70 \times 10^{-7}$ s^{-1}, $R^2 = 0.9379$; 177 K: $A_0 = 0.88$, $k = 2.96 \times 10^{-7}$ s^{-1}, $R^2 = 0.8725$; 183 K: $A_0 = 0.71$, $k = 9.11 \times 10^{-7}$ s^{-1}, $R^2 = 0.8074$; 187 K: $A_0 = 0.67$, $k = 1.95 \times 10^{-6}$ s^{-1}, $R^2 = 0.7151$.

the value at $t = 0$. Using the biexponential model, the simulation parameters calculated for the two components are presented in Table 4.1. The data shows that as the temperature increases, both of the fast phase and slow phase decay faster. In contrast to the single step model described above, the fittings are significantly improved, with higher R-squared values, indicating that there are at least two phases in the samples. This is consistent with the previous studies at $T \geq 190$ K.[36] In Figure 4.4, the decays at the temperatures of 177, 183 and 187 K, for which the decay proceeds to normalized amplitude of ≤ 0.3, provide an apparent near-complete decay through the "fast" channel, and a significant decay through the "slow" channel. This allows a critical assessment of the quality of the biexponential fit for these temperatures. In contrast, the decay at 173 K proceeds to a normalized amplitude of approximately 0.5, and the "slow" phase is not well represented. As shown in Figure 4.4, the simulated curves deviate significantly from the experimental decay data for 177, 183, and 187 K, and in particular, for incubation times longer than 5×10^5 s. The deviations suggest the introduction a new model, which provides a more accurate fit for the slow phase.

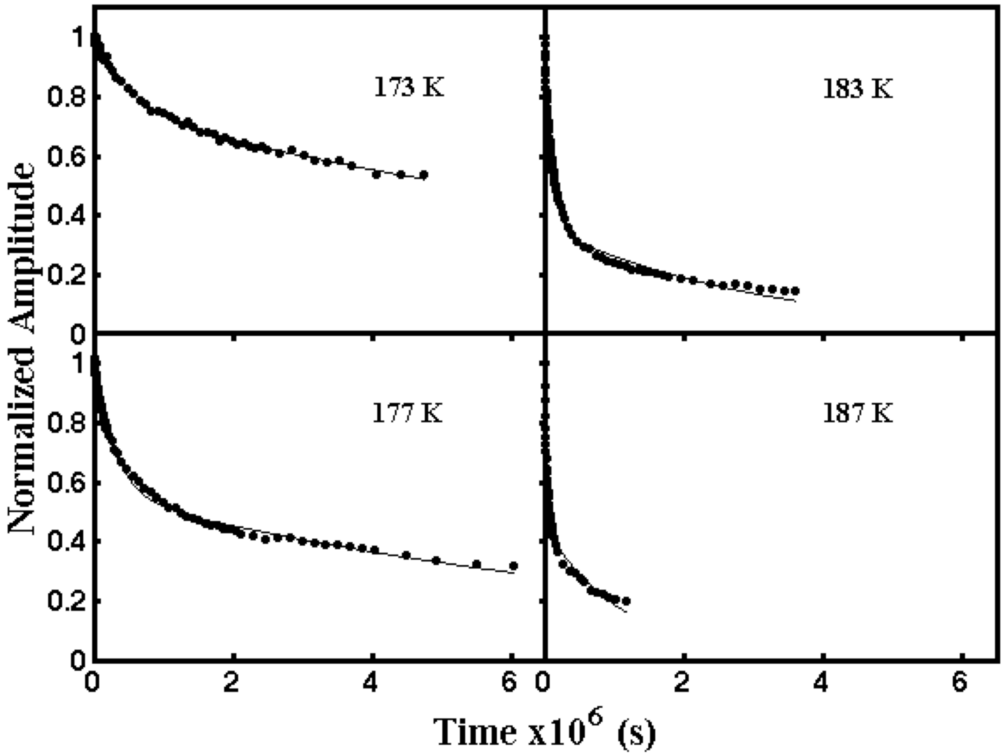

Figure 4.4 Dependence of EPR amplitudes of the cryotrapped Co(II) and substrate radical pair on incubation times at different temperatures: 173, 177, 183 and 187 K, and overlaid with best-fit biexponential functions. The amplitude (solid) was normalized to the value at $t = 0$. *Simulation parameters*: 173 K: $A_1 = 0.24$, $k_1 = 1.94 \times 10^{-6}$ s^{-1}, $A_2 = 0.76$, $k_2 = 7.91 \times 10^{-8}$ s^{-1}, $R^2 = 0.9975$; 177 K: $A_1 = 0.44$, $k_1 = 3.35 \times 10^{-6}$ s^{-1}, $A_2 = 0.56$, $k_2 = 1.07 \times 10^{-7}$ s^{-1}, $R^2 = 0.9973$; 183 K: $A_1 = 0.64$, $k_1 = 9.68 \times 10^{-6}$ s^{-1}, $A_2 = 0.36$, $k_2 = 3.25 \times 10^{-7}$ s^{-1}, $R^2 = 0.9949$; 187 K: $A_1 = 0.55$, $k_1 = 2.81 \times 10^{-5}$ s^{-1}, $A_2 = 0.45$, $k_2 = 8.70 \times 10^{-7}$ s^{-1}, $R^2 = 0.9935$. The values of the time constant are included in Table 4.1.

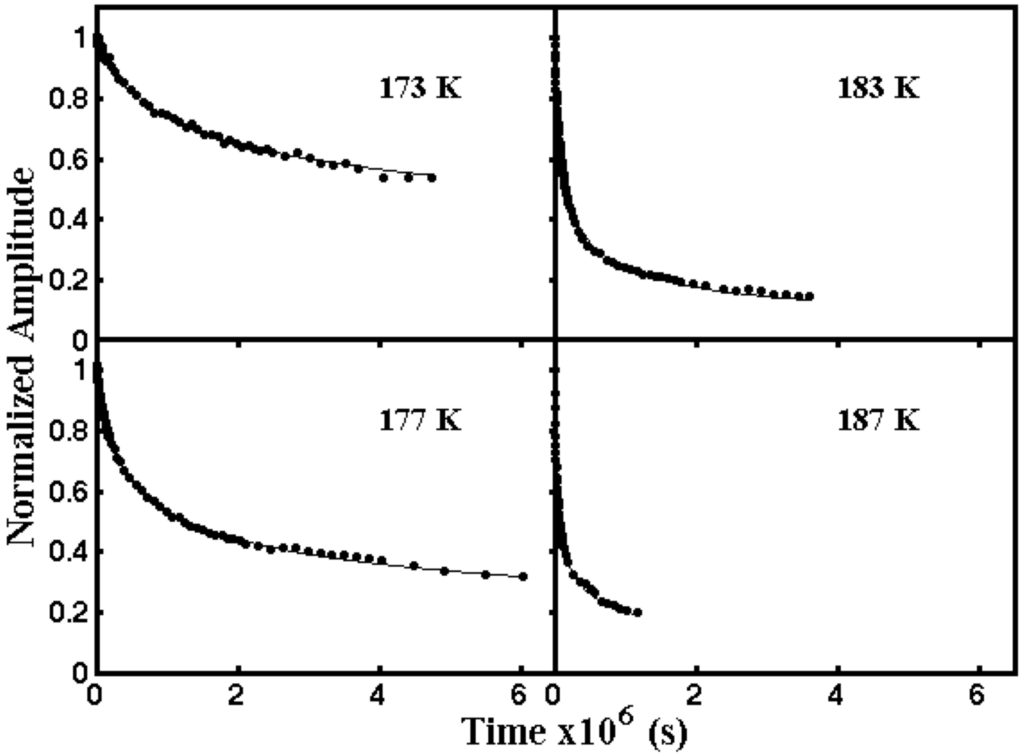

Figure 4.5 Dependence of EPR amplitudes of the cryotrapped Co(II) and substrate radical pair on incubation times at different temperatures: 173, 177, 183 and 187 K, and overlaid with best-fit power-law functions. The amplitude (solid) was normalized to the value at $t = 0$. *Simulation parameters*: 173 K: $t_0 = 3.6 \times 10^5$ s, $n = 0.228$, $R^2 = 0.9972$; 177 K: $t_0 = 1.6 \times 10^5$ s, $n = 0.314$, $R^2 = 0.9987$; 183 K: $t_0 = 5.0 \times 10^4$ s, $n = 0.469$, $R^2 = 0.9986$; 187 K: $t_0 = 1.52 \times 10^4$ s, $n = 0.379$, $R^2 = 0.9980$. The values of the time constant are included in Table 4.1.

Figure 4.5 shows the experimental data fitted by a power law function with the following expression:

$$A(t) = (1 + t / t_0)^{-n} \qquad \text{Eq. 4.3}$$

where A(t) is the normalized amplitude, t_0 and n are adjustable parameters and change with temperature.[130] One difference of this model from the biexponential model is that it contains two adjustable parameters, whereas the biexponential model needs three. Another difference is that instead of assuming one or two components in the samples, it represents a continuous distribution of first-order decay components, each with a separate *k* value. The inverse Laplace transform of the function in Eq. 4.3 provides the distribution function, *g*(*k*), for the rate constants, k.[130] The power law fittings were found to give the best agreement with the decays over the whole range in measurement time when compared with the other fitting functions. This implies that the ensemble of substrate radicals decay through multiple exponential decays in the system at ultra low temperatures of $T \leq 187$ K.

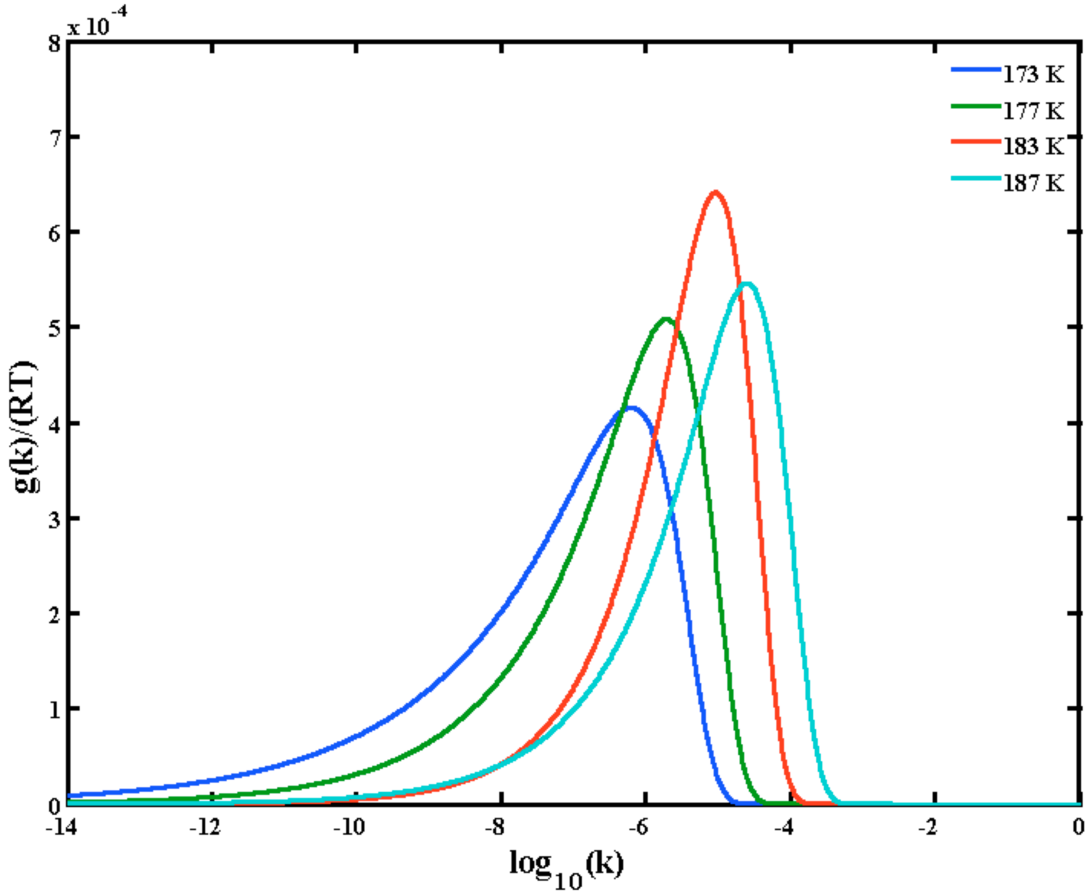

Figure 4.6 Analytical plot of g(k)/RT versus $\log_{10}$(k) at different temperatures: 173, 177, 183, and 187 K. Here, g(k) is the distribution function derived in equation (14) from the reference,[130] R is the gas constant, T is the temperature. The values of the rate constant, k, were assigned to range from 10^{-14} to 1 s^{-1}.

Figure 4.6 shows the dependence of the analytical calculation of the normalized distribution function, $g(k)/RT$, on $\log_{10}(k)$, where k is the decay rate constant of a particular substate of the system. The distributions were calculated from the following expression:[130]

$$\frac{g(k)}{RT} = \frac{(t_0 k)^n e^{-t_0 k}}{\Gamma(n)} \qquad \text{Eq. 4.4}$$

where $g(k)$ represents the probability of finding a substrate radical with rate constant between k and k+dk, $\Gamma(n)$ is the gamma function, T is the temperature, t_0 and n are obtained by fitting Eq. 4.3 for each temperature, R is the gas constant. Here, the values of k were set to span a wide range from 10^{-14} to 1 s^{-1} and apply to all the four temperatures. As temperature decreases, the rate constant at which $g(k)/RT$ peaks decreases. The full width at half maximum expands during the temperature cooling from 183 to 173 K, indicating an increase of different conformational states or higher heterogeneity in the protein system.

Table 4.1: Fitting parameters for the biexponential and power law function to the Co(II)-substrate radical pair decay kinetics at different temperatures for the natural abundance (^{1}H) states.

Biexponential fitting parameters	T (K)	k_f (s^{-1})	A_f[a]	k_s (s^{-1})	A_s[b]	R^2[c]
	173	1.94×10^{-6}	0.24	7.91×10^{-8}	0.76	0.9975
	177	3.35×10^{-6}	0.44	1.07×10^{-7}	0.56	0.9973
	183	9.68×10^{-6}	0.64	3.25×10^{-7}	0.36	0.9949
	187	2.81×10^{-5}	0.55	8.70×10^{-7}	0.45	0.9935
Power law Fitting parameters	T (K)	t_0 (s)		n		R^2[c]
	173	3.6×10^5		0.228		0.9972
	177	1.6×10^5		0.314		0.9987
	183	5.0×10^4		0.469		0.9986
	187	1.52×10^4		0.379		0.9980

[a] The relative fitted amplitude for the fast phase, normalized to the sum, A_f+A_s.

[b] The relative fitted amplitude for the slow phase, normalized to the sum, A_f+A_s.

[c] R is Pearson's correlation coefficient.

4.4 Conclusion

The decay kinetics of Co(II)-substrate radical pair was investigated in the temperature range of 173-187 K. Three models have been used and compared to probe the dynamical behavior of EAL around the "transition" temperature. The power law function provides the best fitting for the time resolved decay for all four temperatures, implying that there are multiple distributed population of substrate radicals with different energy barriers at low temperatures down to 173 K. Previously, we investigated the dynamics of solutions with and without proteins in this temperature range, and no obvious transition was observed below 190 K. The abrupt reduction in the kinetics of the decay of substrate radicals at temperatures below 183 K might result from protein itself or interactions with water molecules in the hydration shell.

Chapter 5

Connections: EPR spectroscopic and relaxation studies of the solution and protein mesodomain environments in frozen aqueous solutions, and kinetics of the radical rearrangement reaction in EAL

The diverse set of studies presented in this dissertation is united by the application of multiple EPR techniques. In Chapter 2, four EPR techniques, continuous-wave EPR spectroscopy, and the repetition rate dependence and τ-dependent decay of the 2-pulse ESE, and three-pulse ESEEM methods of pulsed-EPR spectroscopy, were used to characterize the interstitial mesoscopic domain (mesodomain) in frozen pure aqueous and frozen aqueous-sucrose samples. The results revealed the structure (composition, concentrations of components, volume), and a dynamical feature (the glass transition temperature, T_g'), of the mesodomain.[70] In Chapter 3, application of the same set of EPR techniques led to characterization of the mesodomain structure and dynamics in water-only and aqueous-sucrose solutions that included EAL protein, with and without substrate aminoethanol. In Chapter 4, continuous-wave EPR was used in the dual role of spectroscopy and monitor of reaction kinetics: Time-resolved, full-spectrum continuous-wave EPR spectroscopy was applied to measure the decay of the substrate radical in a previously unexplored temperature regime, at T<190 K. The results provided the kinetics of the radical rearrangement in EAL in this low temperature regime, and the EPR line shape indicated that the substrate radical decays without detectable intermediate states. In combination, the multiple EPR techniques have provided unprecedented insights into the structure and the dynamics of the mesodomain, the kinetics and mechanism of the core rearrangement reaction in EAL, and correlations between mesodomain dynamics and rearrangement reaction kinetics.

The long-term goal of the general approach presented in this dissertation, is to define the structure and dynamics of the mesodomain environment of the protein, so that correlations of the mesodomain solvent properties with the low-temperature kinetics of the substrate radical decay reaction can be made. The hypothesis is that the correlations will reveal contributions of solvent to the chemical reaction steps in EAL. As one thrust in this two-front general approach, studies of the mesodomains in frozen aqueous solutions in the presence and absence of EAL protein are presented in Chapters 2 and 3. In Chapter 2, the temperature dependence of the CW-EPR lineshape showed the glass transition temperature, T_g', of the mesodomain, based on observation of the mobility transition of the TEMPOL. The repetition rate dependence of the 2-pulse ESE provided an observed spin lattice relaxation time, T_1, and the measured T_1 dependence on TEMPOL concentration under global glass conditions led to a calibration, which allowed determination of the absolute concentration of TEMPOL in the mesodomain. The relative TEMPOL mesodomain concentration, measured by the 2-pulse ESE phase memory time, T_M, at different added sucrose concentrations, was consistent with the T_1-determined TEMPOL mesodomain concentrations. Three-pulse ESEEM of the TEMPOL interaction with ^{2}H nuclei on ^{2}H-labeled sucrose provided an assessment of the relative sucrose concentration in the mesodomain. In combination, the results from the pulsed-EPR techniques revealed a critical dynamical feature (the T_g') of the mesodomain, and new insights into the detailed structure of the aqueous sucrose mesodomain: At $\geq$3% (w/v) of added sucrose, the mesodomain maintains a constant concentration of sucrose in a disordered (amorphous, glass) phase at the "maximally freeze concentrated" value of 120% (w/v), while a quantified fraction of the sucrose forms an ordered phase, which is composed of sucrose-hydrates.

In Chapter 3, the frozen aqueous solution mesodomain studies are expanded to include the EAL protein, under conditions comparable with those in the substrate radical decay reaction kinetics measurements. The same set of EPR techniques, as in Chapter 2, was applied to frozen water-only and aqueous-sucrose solutions that included EAL protein, with and without the substrate, aminoethanol. The combined pulsed-EPR results indicated that the EAL protein, itself, creates a homogeneous, mesodomain-like environment in which the TEMPOL resides. The addition of aminoethanol, at concentrations used in samples for the kinetic studies, promoted additional mesodomain formation. Both conditions led to a comparable shift in the TEMPOL mobility transition, or T_g', relative to the pure aqueous solution condition. Addition of sucrose contributed to the volume and glass transition properties of the protein mesodomain in the presence of EAL and EAL-aminoethanol, in a manner that was consistent with the solution-only studies.

In Chapter 4, the kinetics of substrate radical decay (the radical rearrangement reaction) are addressed by using time-resolved, full-spectrum continuous-wave EPR spectroscopy. The kinetics of the rearrangement reaction (the substrate radical decay reaction) in EAL in the low-temperature, frozen aqueous system have been previously determined for the temperature range of 223 to 190 K.[36, 129] Recent results indicate that the bifurcation of the decay kinetics into fast and slow exponential components, as the temperature is decreased, occurs at approximately 230-240 K (M. M. Kohne, C. Zhu, K. Warncke, unpublished). This temperature range is coincident with the T_g' of 235 K for the EAL protein mesodomain, thus indicating a correlation between the mesodomain solvent dynamics and the rearrangement reaction mechanism. This validates the general, two-thrust approach, of characterizing and comparing the mesodomain and protein reaction kinetics. The studies in Chapter 4 seek to identify additional influences of protein and coupled solvent on the rearrangement reaction kinetics, by addressing the substrate radical decay in the previously unexplored temperature range below 190 K. The extremely long decay durations (on the order of megaseconds, Ms; 1 year=6×10^6 s), that are necessary to reach decay levels of ≤20% of the initial population in the T<190 K range, required the development of new protocols for the kinetic measurements. Toward this, the samples were held at the decay temperature in a specialized, high-accuracy temperature bath-calibrator device. The bath-calibrator and associated EPR sampling protocols, allowed decays at 173-187 K to proceed to the low levels necessary for reliable fitting of the time-dependences, to determine the appropriate kinetic model. The agreement provided by a power law fitting in preliminary analysis, suggests that the protein and coupled solvent fluctuations become reaction rate limiting at T<180 K. In future work, we will use EPR spectroscopy of nitroxide spin labels, directly (covalently) attached to the EAL protein surface, to reveal correlations of the temporal and spatial properties of the protein (and coupled hydration shell) motions with the kinetics of the rearrangement reaction.

Bibliography

1. Buckel, W. and Golding, B. T., *Chem. Soc. Rev.*, 1996, **25**, 329-&.
2. Banerjee, R., *Chemistry and Biochemistry of B12*, John Wiley and Sons, New York, 1999.
3. Brown, K. L., *Chem. Rev.*, 2005, **105**, 2075-2149.
4. Faust, L. P. and Babior, B. M., *Arch. Biochem. Biophys.*, 1992, **294**, 50-54.
5. Shibata, N., Tamagaki, H., Hieda, N., Akita, K., Komori, H., Shomura, Y., Terawaki, S., Mori, K., Yasuoka, N., Higuchi, Y. and Toraya, T., *J. Biol. Chem.*, 2010, **285**, 26484-26493.
6. Roof, D. M. and Roth, J. R., *J. Bacteriol.*, 1988, **170**, 3855-3863.
7. Roof, D. M. and Roth, J. R., *J. Bacteriol.*, 1989, **171**, 3316-3323.
8. Brinsmade, S. R., Paldon, T. and Escalante-Semerena, J. C., *J. Bacteriol.*, 2005, **187**, 8039-8046.
9. Srikumar, S. and Fuchs, T. M., *Appl. Environ. Microb.*, 2011, **77**, 281-290.
10. Kendall, M. M., Gruber, C. C., Parker, C. T. and Sperandio, V., *Mbio*, 2012, **3**.
11. Li, H., Kristensen, D. M., Coleman, M. K. and Mushegian, A., *Plos One*, 2009, **4**.
12. Hubbard, T. J. P., Ailey, B., Brenner, S. E., Murzin, A. G. and Chothia, C., *Nucleic. Acids. Res.*, 1999, **27**, 254-256.
13. Toraya, T., *Chem. Rev.*, 2003, **103**, 2095-2127.
14. Barker, H. A., Iodice, A. A., Rooze, V. and Suzuki, F., *J. Biol. Chem.*, 1964, **239**, 3260-&.
15. Marsh, E. N. G. and Ballou, D. P., *Biochemistry*, 1998, **37**, 11864-11872.
16. Moore, B. S., Eisenberg, R., Weber, C., Bridges, A., Nanz, D. and Robinson, J. A., *J. Am. Chem. Soc.*, 1995, **117**, 11285-11291.
17. Pierik, A. J., Ciceri, D., Broker, G., Edwards, C. H., McFarlane, W., Winter, J., Buckel, W. and Golding, B. T., *J. Am. Chem. Soc.*, 2002, **124**, 14039-14048.
18. Pierik, A. J., Ciceri, D., Lopez, R. F., Kroll, F., Broker, G., Beatrix, B., Buckel, W. and Golding, B. T., *Biochemistry*, 2005, **44**, 10541-10551.
19. Marsh, E. N. G., *Bioessays*, 1995, **17**, 431-441.
20. Babior, B. M., *B12*, Wiley, New York, 1982.
21. Babior, B. M. and Li, T. K., *Biochemistry*, 1969, **8**, 154-&.
22. Klopotow.T and Wiater, A., *Arch. Biochem. Biophys.*, 1965, **112**, 562-&.
23. Manitto, P., Speranza, G., Fontana, G. and Galli, A., *Helvetica Chimica Acta*, 1998, **81**, 2005-2016.
24. Ghambeer, R. K., *Indian J. Biochem.*, 1967, **4**, 36-&.
25. Chirpich, T. P., Zappia, V., Costilow, R. N. and Barker, H. A., *J. Biol. Chem.*, 1970, **245**, 1778-&.
26. Wolthers, K. R., Rigby, S. E. J. and Scrutton, N. S., *J. Biol. Chem.*, 2008, **283**, 34615-34625.

27. Marsh, E. N. G., *Essays. Biochem.*, 1999, **34**, 139-154.
28. Bovell, A. M. and Warncke, K., *Biochemistry*, 2013, **52**, 1419-1428.
29. Banerjee, R. and Ragsdale, S. W., *Annu. Rev. Biochem.*, 2003, **72**, 209-247.
30. Pratt, J. M., *Inorganic Chemistry of Vitamin B12*, Academic Press INC, New York, 1972.
31. Bandarian, V., Poyner, R. R. and Reed, G. H., *Biochemistry*, 1999, **38**, 12403-12407.
32. Weisblat, D. A. and Babior, B. M., *J. Biol. Chem.*, 1971, **246**, 6064-6071.
33. Carty, T. J., Babior, B. M. and Abeles, R. H., *J. Biol. Chem.*, 1974, **249**, 1683-1688.
34. Licht, S. S., Lawrence, C. C. and Stubbe, J., *J. Am. Chem. Soc.*, 1999, **121**, 7463-7468.
35. Bradbeer, C., *J. Biol. Chem.*, 1965, **240**, 4669-&.
36. Zhu, C. and Warncke, K., *Biophys. J.*, 2008, **95**, 5890-5900.
37. Babior, B. M., Carty, T. J. and Abeles, R. H., *J. Biol. Chem.*, 1974, **249**, 1689-1695.
38. Ke, S. C., Torrent, M., Museav, D. G., Morokuma, K. and Warncke, K., *Biochemistry*, 1999, **38**, 12681-12689.
39. He, Y. F., Ku, P. I., Knab, J. R., Chen, J. Y. and Markelz, A. G., *Phys. Rev. Lett.*, 2008, **101**.
40. Bhat, S. N., Sharma, A. and Bhat, S. V., *Phys. Rev. Lett.*, 2005, **95**, 2357021-2357024.
41. Ringe, D. and Petsko, G. A., *Biophys. Chem.*, 2003, **105**, 667-680.
42. Parak, F., Knapp, E. W., Chang, I. and Nienhaus, G. U., *Hyperfine. Interact.*, 1992, **70**, 1125-1128.
43. Parak, F., Frolov, E. N., Mossbauer, R. L. and Goldanskii, V. I., *J. Mol. Biol.*, 1981, **145**, 825-833.
44. Doster, W., Cusack, S. and Petry, W., *Nature*, 1989, **337**, 754-756.
45. Hartmann, H., Parak, F., Steigemann, W., Petsko, G. A., Ponzi, D. R. and Frauenfelder, H., *Proc. Natl. Acad. Sci. U. S.*, 1982, **79**, 4967-4971.
46. Loncharich, R. J. and Brooks, B. R., *J. Mol. Biol.*, 1990, **215**, 439-455.
47. Doster, W., Bachleitner, A., Dunau, R., Hiebl, M. and Luscher, E., *Biophys. J.*, 1986, **50**, 213-219.
48. Demmel, F., Doster, W., Petry, W. and Schulte, A., *Eur. Biophys. J. Biophy.*, 1997, **26**, 327-335.
49. Mattos, C., *Trends Biochem. Sci.*, 2002, **27**, 203-208.
50. Teeter, M. M., Yamano, A., Stec, B. and Mohanty, U., *Proc. Natl. Acad. Sci. U. S.*, 2001, **98**, 11242-11247.
51. Vitkup, D., Ringe, D., Petsko, G. A. and Karplus, M., *Nat. Struct. Biol.*, 2000, **7**, 34-38.
52. Ngai, K. L., Capaccioli, S. and Shinyashiki, N., *J. Phys. Chem. B*, 2008, **112**, 3826-3832.

53. Capaccioli, S., Ngai, K. L. and Shinyashiki, N., *J. Phys. Chem. B*, 2007, **111**, 8197-8209.
54. Fenimore, P. W., Frauenfelder, H., McMahon, B. H. and Parak, F. G., *Proc. Natl. Acad. Sci. U. S.*, 2002, **99**, 16047-16051.
55. Fenimore, P. W., Frauenfelder, H., McMahon, B. H. and Young, R. D., *Proc. Natl. Acad. Sci. U. S.*, 2004, **101**, 14408-14413.
56. Lee, A. L. and Wand, A. J., *Nature*, 2001, **411**, 501-504.
57. Zavoisky, E., *J. Phys. USSR*, 1945, **9**, 211-216.
58. Zavoisky, E., *J. Phys. USSR*, 1946, **10**, 197-198.
59. Wertz, J. E. and Bolton, J. R., *Electron Spin Resonance*, Chapman and Hall: New York,, 1986.
60. Altshuler, S. A. K., B. M. , *Electron Paramagnetic Resonance*, Academic Press: New York, 1964.
61. Eaton, G. R., Eaton, S. S., Barr, D. P., and Weber, R. T. , *Quantitative EPR*, Springer, 2010.
62. Pilbrow, J. R., in *In B12*, ed. D. Dolphin, Wiley: New York, 1982, vol. 1, p. 431.
63. Babior, B. M., Moss, T. H., Ormejohn.Wh and Beinert, H., *J. Biol. Chem.*, 1974, **249**, 4537-4544.
64. Gerfen, G. J., in *Chemistry and Biochemistry of B12*, ed. R. Banerjee, John Wiley and Sons, New York, 1999, pp. 165-195.
65. Canfield, J. M. and Warncke, K., *J. Phys. Chem. B*, 2002, **106**, 8831-8841.
66. Bandarian, V. and Reed, G. H., *Biochemistry*, 2002, **41**, 8580-8588.
67. Ke, S. C., *Bba-gen. Subjects.*, 2003, **1620**, 267-272.
68. Schweiger, A. and Jeschke, G., *Principles of pulse electron paramagnetic resonance*, Oxford University Press, Oxford, UK, 2001.
69. Mims, W. B., *Phys. Rev. B*, 1972, **5**, 2409-2414.
70. Chen, H., Sun, L. and Warncke, K., *Langmuir*, 2013, **29**, 4357-4365.
71. Sun, L., Hernandez-Guzman, J. and Warncke, K., *J. Magn. Reson.*, 2009, **200**, 21-28.
72. Mazur, P., *Science*, 1970, **168**, 939-949.
73. Douzou, P., *Cryobiochemistry: An Introduction*, Academic Press, New York, 1977.
74. Gook, D. A. and Edgar, D. H., *Hum. Reprod. Update*, 2007, **13**, 591-605.
75. Young, F. E. and Jones, F. T., *J. Phys. Coll. Chem.*, 1949, **53**, 1334-1350.
76. Franks, F., *Biophys. Chem.*, 2003, **106**, 251-261.
77. Goff, H. D., Verespej, E. and Jermann, D., *Thermochim. Acta*, 2003, **399**, 43-55.
78. Franks, F., *Eur. J. Pharm. Biopharm.*, 1998, **45**, 221-229.
79. Mackenzie, A. P., Derbyshire, W. and Reid, D. S., *Philos. T. Trans. Roy. Soc. B*, 1977, **278**, 167-&.
80. Karel, M., Roos, Y. and Briera, M. P., in *Glassy state in food*, eds. J. M. V. Blanshard and P. J. Lilliford, Nottingham University Press, Loughborough, UK, 1994.
81. Johari, G. P., Hallbrucker, A. and Mayer, E., *Nature*, 1987, **330**, 552-553.

82. Banerjee, D., Bhat, S. N., Bhat, S. V. and Leporini, D., *Proc. Natl. Acad. Sci.*, 2009, **106**, 11448-11453.
83. Dantsker, D., Samuni, U., Friedman, J. M. and Agmon, N., *Biochim. Biophys. Acta*, 2005, **1749**, 234-251.
84. Frauenfelder, H., Chen, G., Berendzen, J., Fenimore, P. W., Jansson, H., McMahon, B. H., Stroe, I. R., Swenzon, J. and Young, R. D., *Proc. Natl. Acad. Sci.*, 2009, **106**, 5129-5134.
85. Jansson, H., Bergman, R. and Swenzon, J., *J. Phys. Chem. B*, 2011, **115**, 4099-4109.
86. Stoll, S. and Schweiger, A., *J. Magn. Reson.*, 2006, **178**, 42-55.
87. Mims, W. B. and Peisach, J., in *Biological Magnetic Resonance*, eds. L. J. Berliner and J. Reuben, Plenum, New York, 1981, vol. 3, ch. 5, pp. 213-263.
88. Bowman, M. K., in *Modern pulsed and continuous wave electron spin resonance*, eds. L. Kevan and M. K. Bowman, John Wiley and Sons, New York, 1990, ch. 1, pp. 1-42.
89. Hellwege, K.-H. and Hellwege, A. M., *Landolt-Bornstein Numerical Data and Functional Relationships in Science and Technology*, Springer-Verlag, New York, 1988.
90. Pake, G. E. and Estle, T. L., *The physical principles of electron paramagnetic resonance*, W. A. Benjamin, Inc., Reading, Massachusetts, 1973.
91. Bartos, J., Andreozzi, L., Faetti, M., Sausa, O., Racko, D. and Kristiak, J., *J. Non-Cryst. Solids*, 2006, **352**, 4785-4789.
92. Redfield, A. G., *IBM J. Res. Dev.*, 1957, **1**, 19-31.
93. Kulikov, A. V. and Likhtenshtein, G. I., *Adv. Mol. Relax. Int. Pr.*, 1977, **10**, 47-69.
94. Poole, C. P. J. and Farach, H., *Relaxation in Magnetic Resonance*, Academic Press, New York, 1971.
95. Kumler, P. L. and Boyer, R. F., *Macromolecules*, 1976, **9**, 903-910.
96. Longinotti, M. P. and Corti, H. R., *J. Phys. Chem. Ref. Data*, 2008, **37**.
97. Riseman, J. and Ullman, R., *J. Chem. Phys.*, 1951, **19**, 578-584.
98. Shalev, E. Y. and Franks, F., *Thermochim. Acta*, 1995, **255**, 49-61.
99. Mathlouthi, M., Luu, C., Meffroy-Biget, A. M. and Luu, D. V., *Carbohyd. Res.*, 1980, **81**, 213-223.
100. Mathlouthi, M., Cholli, A. L. and Koenig, J. L., *Carbohyd. Res.*, 1986, **147**, 1-9.
101. Mathlouthi, M., *Carbohyd. Res.*, 1981, **91**, 113-123.
102. Schneider, F., Schliephake, D. and Klimmek, A., *Zucker*, 1963, **17**, 465-473.
103. Mathlouthi, M. and Genotelle, J., *Carbohyd. Polym.*, 1998, **37**, 335-342.
104. Richardson, S. J., Baianu, I. C. and Steinberg, M. P., *J. Food Sci.*, 1987, **52**, 806-&.
105. Rampp, M., Buttersack, C. and Ludemann, H. D., *Carbohyd. Res.*, 2000, **328**, 561-572.
106. Chaplin, M., *Nat. Rev. Mol. Cell Bio*, 2006, **7**, 861-866.
107. Lipton, A. S., Heck, R. W., de Jong, W. A., Gao, A. R., Wu, X., Roehrich, A., Harbison, G. S. and Ellis, P. D., *J. Am. Chem. Soc.*, 2009, **131**, 13992-13999.

108. Siemer, A. B., Huang, K. Y. and McDermott, A. E., *Proc. Natl. Acad. Sci. U. S.*, 2010, **107**, 17580-17585.
109. Stanley, H. E., Buldyrev, S. V., Franzese, G., Kumar, P., Mallamace, F., Mazza, M. G., Stokely, K. and Xu, L., *J. Phys-condens. Mat.*, 2010, **22**, 284101.
110. Swenson, J., Jansson, H. and Bergman, R., *Phys. Rev. Lett.*, 2006, **96**, 247802.
111. Huang, Y. W., Lai, Y. C., Tsai, C. J. and Chiang, Y. W., *Proc. Natl. Acad. Sci. U. S.*, 2011, **108**, 14145-14150.
112. Hollaway, M. R., Johnson, A. W., Lappert, M. F. and Wallis, O. C., *Eur. J. Biochem.*, 1980, **111**, 177-188.
113. Bandarian, V. and Reed, G. H., *Biochemistry*, 1999, **38**, 12394-12402.
114. Handa, Y. P. and Klug, D. D., *J. Phys. Chem.*, 1988, **92**, 3323-3325.
115. Borovykh, I. V., Kulik, L. V., Gast, P. and Dzuba, S. A., *Chem. Phys.*, 2003, **294**, 433-438.
116. Parak, F., Knapp, E. W. and Kucheida, D., *J. Mol. Biol.*, 1982, **161**, 177-194.
117. Tsai, A. M., Neumann, D. A. and Bell, L. N., *Biophys. J.*, 2000, **79**, 2728-2732.
118. Smith, J., Kuczera, K. and Karplus, M., *Proc. Natl. Acad. Sci. U. S.*, 1990, **87**, 1601-1605.
119. Keller, H. and Debrunner, P. G., *Phys. Rev. Lett.*, 1980, **45**, 68-71.
120. Knapp, E. W., Fischer, S. F. and Parak, F., *J. Phys. Chem.*, 1982, **86**, 5042-5047.
121. Frauenfelder, H., Petsko, G. A. and Tsernoglou, D., *Nature*, 1979, **280**, 558-563.
122. Tilton, R. F., Jr., Dewan, J. C. and Petsko, G. A., *Biochemistry*, 1992, **31**, 2469-2481.
123. Ferrand, M., Dianoux, A. J., Petry, W. and Zaccai, G., *Proc. Natl. Acad. Sci. U. S.*, 1993, **90**, 9668-9672.
124. Brooks, C. L., Karplus, M. and Pettitt, B. M., *Proteins: A Theoretical Perspective of Dynamics, Structure, and Thermodynamics*, Wiley-Interscience, 1988.
125. Bragger, J. M., Dunn, R. V. and Daniel, R. M., *Bba-protein. Struct. M*, 2000, **1480**, 278-282.
126. Faust, L. R. P., Connor, J. A., Roof, D. M., Hoch, J. A. and Babior, B. M., *J. Biol. Chem.*, 1990, **265**, 12462-12466.
127. Harkins, T. T. and Grissom, C. B., *J. Am. Chem. Soc.*, 1995, **117**, 566-567.
128. Kaplan, B. H. and Stadtman, E. R., *J. Biol. Chem.*, 1968, **243**, 1787-&.
129. Zhu, C. and Warncke, K., *J. Am. Chem. Soc.*, 2010, **132**, 9610-9615.
130. Austin, R. H., Beeson, K. W., Eisenstein, L., Frauenfelder, H. and Gunsalus, I. C., *Biochemistry*, 1975, **14**, 5355-5373.